UNIVERSITÀ DEGLI STUDI
DI GENOVA

Molecular-level characterization of the interaction between monolayer-protected Au nanoparticles and model lipid membranes and proteins

Candidate:

Federica Simonelli

Supervisor:

Giulia Rossi

Genoa, 17 December 2018

ABSTRACT

In this thesis we study the interactions of monolayer-protected gold nanoparticles with proteins and model lipid membranes. Gold nanoparticles are a paradigm in biological applications of nanomaterials, thanks to their peculiar physico-chemical properties; among these, the possibility to bind different kinds of molecules (ligands) to gold atoms in clusters *via* thiol bonds is particularly important for biomedical use of nanoparticles. In fact, the ligand shell is what nanoparticles expose to the biological environment in which they are used. In *in vivo* applications, nanoparticles come in contact with many biological molecules before being delivered to cells, which are the target of most of biological applications of nanoparticles. Among them, proteins are particularly relevant since they can irreversibly bind to nanoparticles, thus changing the surface they expose to the biological environment.
In this thesis we use molecular dynamics simulations to study how different ligands can influence the interaction of nanoparticles with the most abundant protein in blood, human serum albumin. We test two zwitterionic ligands with different hydrophobic content and we find that ligand conformation, which is affected by hydrophobicity, promotes different adhesion strengths between nanoparticles and albumin. We then study the interaction of nanoparticles with a model cell membrane, the first barrier they encounter in cell-targeted applications. We use molecular dynamics simulations to study the mechanism of interaction between a negatively charged nanoparticle and a neutral lipid membrane. We find that the process develops in three stages which involves the adsorption on the membrane surface and the progressive penetration in the membrane core of the nanoparticle. Finally, we study the influence of the sign of the charge on nanoparticles on their interaction with a model membrane. We use experiments of fluorescent dye-leakage from neutral liposomes to probe the effect of positively and negatively charged nanoparticles on the model membrane of the lipid vesicles. In particular, we find that both anionic and cationic nanoparticles behave similarly in the interaction with a zwitterionic lipid membrane. We use molecular dynamics simulations to support the experimental findings and observe that anionic and cationic nanoparticles share similar interaction processes and energetics.

To my brother and my family

LIST OF PUBLICATIONS

Federica Simonelli, Davide Bochicchio, Riccardo Ferrando and Giulia Rossi. "Monolayer-Protected Anionic Au Nanoparticles Walk into Lipid Membranes Step by Step". In: J. Phys. Chem. Lett. 2015, 6, 16, pp. 3175-3179

Sebastian Salassi, Federica Simonelli, Davide Bochicchio, Riccardo Ferrando and Giulia Rossi. “Au Nanoparticles in Lipid Bilayers: A Comparison between Atomistic and Coarse-Grained Models”. In: J. Phys. Chem. C 2017, 121, 20, pp. 10927-10935

Andrea Torchi, Federica Simonelli, Riccardo Ferrando and Giulia Rossi. "Local Enhancement of Lipid Membrane Permeability Induced by Irradiated Gold Nanoparticles". In: ACS Nano 2017, 11, 12, pp. 12553-12561

Sebastian Salassi, Federica Simonelli, Alessio Bartocci and Giulia Rossi. "A Martini coarse-grained model of the calcein fluorescent dye". In: J. Phys. D: Appl. Phys. 2018, 51, 38, 384002-384012

Ester Canepa, Sebastian Salassi, Federica Simonelli, Riccardo Ferrando, Ranieri Rolandi, Chiara Lambruschini, Fabio Canepa, Annalisa Relini and Giulia Rossi. In preparation

Federica Simonelli, Giulia Rossi and Luca Monticelli. "Hydrophobicity, charge and ligand conformation drive nanoparticle-protein interactions". To be submitted

CONTENTS

LIST OF ACRONYMS

AA all atom

AUNP gold nanoparticle

BB backbone

CG coarse-grained

COM centre of mass

CV collective variable

FES free energy surface

HSA human serum albumin

MD molecular dynamics

NP nanoparticle

OT octanethiol

PEG polyethylene glycole

PME particle mesh Ewald

PW polarisable water

RDF radial distribution function

RMSD root mean square deviation

RMSF root mean square fluctuation

RMSIP root mean square inner product

SASA solvent accessible surface area

UA united atom

1 NANOPARTICLES AND THEIR BIOMEDICAL APPLICATIONS

Contents

1.1 Nanoparticles in biomedicine

The ability to produce and manipulate objects at the nanoscale has opened the way to the use of nanomaterials in the most diverse fields, ranging from electronics to medicine. In particular, nanoparticles (NPs) have attracted more and more attention over the years because of their particular physical and chemical properties such has high surface-to-volume ratio, possibility of surface functionalisation, high surface reactivity, superparamagnetism, surface plasmon resonance. The possibility to combine two or more of these properties make NPs attractive especially for use in biomedicine where they can be employed as imaging [1], diagnostic [2] or therapeutic agents [3].

1.1.1 Different materials for different applications

Depending on the desired application, specific materials such as metals, metal oxides and polymers can be selected to design NPs with applications in biomedicine, as recently reviewed by McNamara *et al.* [4].
Metallic NPs with gold and silver core can be used in imaging and photothermal therapy exploiting their response to electromagnetic radiation. In fact, metal NPs exhibit the so-called *localised surface plasmon resonance* which is a collective and coherent oscillation of the free electrons in the metal NP under an electromagnetic field. The surface plasmon resonance of NPs can be exploited in at least two different ways in biomedicine. One possibility is that the incident radiation, such as that produced by a laser, is adsorbed by the NP and decays non-radiatively. In this case the NP can effectively convert light into heat. Heat conversion can be used, for example, in photothermal therapy of cancer where localised heating of the tumour cells is necessary to

kill the diseased cells and preserve the surrounding healthy tissues [1]. Alternatively, the incident radiation can be scattered: in this situation, enhanced scattering at the surface plasmon resonance frequency and the high photostability of the NP can be exploited for imaging applications. NPs become then an alternative to fluorescent dyes. For both therapeutic and imaging purposes, it is important that the NP response fall in the NIR region, where radiation is not adsorbed by biological tissues. The absorbance window for metal NPs can be tuned by changing the NP shape, aspect ratio, or by synthesising hollow NPs [5]. An example of gold NPs with different size and shape is shown figure 1

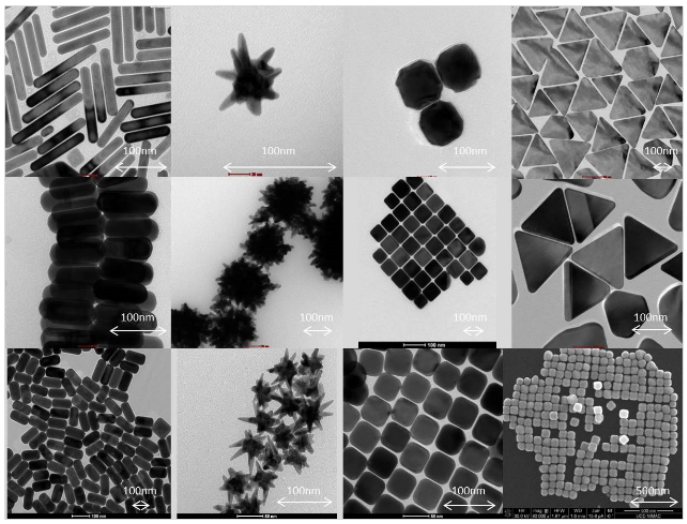

Figure 1: TEM and SEM micrographs of gold NPs with different size, shape and aspect ratio. Taken from
https://www.ucd.ie/cbni/newsevents/cbni-in-the-news/name,196987,en.html

Metal oxide NPs can find different applications in biomedicine ranging from controlled drug delivery to hyperthermia therapy to imaging. Among metal oxides, iron oxide NPs are used in biomedicine as contrast agents in magnetic resonance imaging [6] or for magnetic induced hyperthermia [7], exploiting the superparamagnetic character of iron oxide at the nanoscale. If the size of the NPs is below a certain critical value, a single magnetic domain is present and when an external magnetic field is applied and then removed there is not residual magnetisation, conversely to ferromagnetic NPs. For the latter kind of NPs heat is generated under an external alternating magnetic field because of the hysteresis of the magnetisation. For superparamagnetic NPs, instead, heat production is due to the rotation of the single-domain NPs in the fluid in which they are immersed. Thanks to the lower intensity of the magnetic field required to obtain a significant heating, superparamagnetic NPs are preferred to ferromagnetic ones [8]. Superparamagnetic NPs can also be used as negative contrast agents in magnetic resonance imaging exploiting their ability to influence the relaxation time of the spin of water protons under a magnetic field [9]. Combining high contrast imaging with local hyperthermia makes superparamagnetic NPs ideal candidates for theranostic applications [10], that is diagnostic and therapy can be performed using a single agent.
Metal oxide NPs can also be employed as antimicrobial agents, as in the case of ZnO and CuO NPs [11] or as drug delivery systems like porous TiO_2 NPs; these NPs can be functionalised to achieve specific targeting and the drug

load can be released upon irradiation with UV light to which TiO_2 NPs are sensitive [12].
Quite novel NPs that can be used in magnetic resonance imaging are core/shell NPs. Fe-Pt [13], Fe-Ni [14] and Fe-Co [15] are the most commonly used due to their higher magnetic moment which results in longer relaxation times and therefore higher contrast with respect to metal oxide NPs.
Organic NPs like dendrimers and liposomes can be successfully employed in biomedicine as drug delivery agents. Thanks to the combination of their small size and high branching [16, 17], dendrimers, polymers of branched repeated units that depart from a central core and extend outwards, are particularly useful for drug/gene delivery applications or as imaging tools [18]. Among the most used types of dendrimers are polyamidoamines (PAMAM) and polypeptides. In the aqueous compartment of liposomes, as well as in the lipid membrane that encloses the internal hydrophilic environment, drugs and other molecules of interest can be encapsulated and liposomes used as drug delivery systems.

1.1.2 Functionalisation of NPs

The surface of NPs can be covered with molecules of different kinds which give specific properties to the NPs: such NPs are said to be *functionalised*. One of the most important reasons for surface functionalisation is to prevent aggregation of NPs in the phase of synthesis. In fact, the surface of bare NPs is highly reactive so that NPs are prone to aggregation and precipitation. To avoid this effect different kinds of molecules can be used to cover NP surface: charged molecules are employed to achieve ionic stabilisation, while neutral hydrophilic molecules, such as polyethylene glycole (PEG), act as steric stabilising agents.
The possibility to functionalise the surface of NPs with a variety of molecules can be exploited to confer the desired properties to NPs. For biomedical applications, for example, biological ligands, such as small peptides and DNA strands, can be bound to NPs in targeted delivery or sensing. Fluorescent molecules can also be anchored to NPs for imaging applications. The methods to prepare functionalised NPs for biomedical applications have been recently reviewed by Thanh *et al.* [19]. Whatever the biomedical application is, functionalised NPs have to face the biological environment and functionalisation should be thought to guarantee NP stability in different conditions. More details on this topic are given in subsection 1.1.3.

1.1.3 Major concerns with the use of NPs for *in vivo* applications

With the increasing use of nanosystems in the most diverse fields, from technology to medicine, one of the major issues that needs to be faced is the toxicity of nanomaterials for environment and people's health. For what concerns their biomedical applications, NPs should be biocompatible, that is they should perform their action without causing adverse effects on the patient. It is known that NP toxicity depends not only on NP size, shape, core material and surface chemistry, but also on the application and on the biological host of the NPs. As pointed out by Williams [20], defining biocompatibility is non-trivial and requires case-by-case analysis. Producing general guidelines on material toxicity is thus a hard task.

Each time a specific region of the body should be reached, for example in targeted drug delivery applications or in imaging, NPs are required to circulate in the blood stream without being removed from the macrophages, the garbage collectors of the human body. External-body removal from macrophages starts with adsorption of specific proteins on the NP surface (opsonisation). The proteins are then recognised by macrophages that engulf the NPs and remove them from blood stream [21]. Different strategies have been found to prolong *in vivo* circulation time of NPs, including modifying the surface chemistry of the NPs [22] or varying their shape and size [23]. Cellular toxicity refers to undesired negative effects that are generated on cells and that can affect their viability. One of the possible causes of NPs toxicity is the administered dose of NPs [24, 25]. It is thus crucial to employ the smallest possible NP dose which guarantees the desired efficiency [26]. For delivery applications, this implies an optimisation of different NP parameters such that the largest possible number of molecules should be loaded to the minimum number of NPs. Moreover it is necessary to efficiently deliver NPs to the desired target without NPs being early removed from blood circulation or avoiding cargo loss in undesired regions. This requires coating NPs with suitable molecules so as to stabilise the complex NP–drug and to control the region of release. This can be accomplished using both external stimuli, for example magnetic field for magnetic NPs, or exploiting different local chemical properties such as different pH at tumour sites [27, 28]. Even if a small dose is administered, other toxic effects can come into play once NPs reach cells. The most common toxic effects that are registered in NP administration are induction of oxidative stress [29], cell membrane disruption [30] and DNA damage [31], effects that are common to a large variety of NPs [32].

1.2 The nanoparticle journey through the organism

The wide variety of systems studied in literature and the non-trivial nature of the problem itself makes it difficult to fully understand what happens when NPs are administered to the body. Different routes of administration cause NPs to interact with different biological environments. NPs delivered by intravenous injection, for example, come in contact with blood components such as ions, sugars and proteins which can modify NPs characteristics and thus their fate in the body. The presence of ions can influence NP colloidal stability [33] causing aggregation of NPs and precipitation. This phenomenon is well understood and described by the DLVO (Derjaguin, Landau, Verwey, Overbeek) theory. NP–plasma protein interaction is more complicated and little is known on this issue despite the increasing amount of literature on this topic.

1.2.1 Interaction with proteins – protein corona

Intravenously injected NPs interact with plasma proteins which can associate to the NPs forming the so-called *protein corona* [34]. Plasma proteins refer to a large ensemble of proteins with different functions such as transport and regulation, other than immunogenic, which are present in blood serum. Due to the wide variety of proteins, the composition of the corona can change dynamically. Proteins with the most abundant concentration, such as human

serum albumin (HSA), have the highest probability to be the first proteins to adsorb on the NP surface: the protein layer formed by these proteins is called *soft protein corona*. Typically, these proteins have high association rates; however they can also dissolve quickly leaving the protein corona. Proteins with lower concentration but higher affinity can then bind to the NP surface. This protein layer is called the *hard protein corona*. The competitive and dynamic process which governs protein adsorption is known as the Vroman effect [35]. A schematic picture of a NP surrounded by the protein corona is shown in figure 2

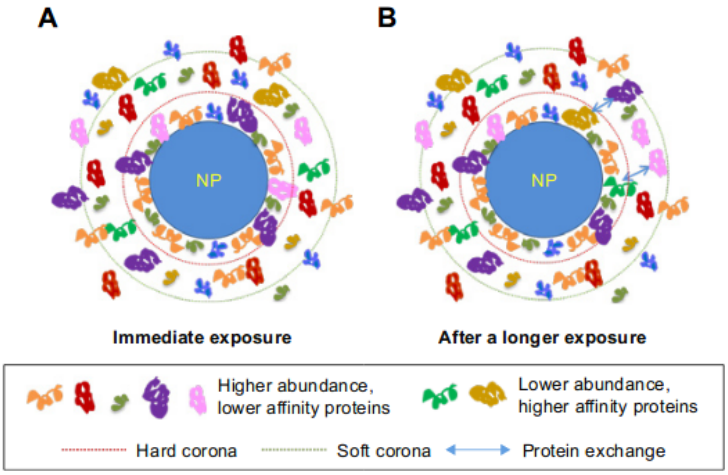

Figure 2: Schematic representation of a nanoparticle surrounded by its protein corona. Proteins with highest concentration but weak affinity are the first to bind to the nanoparticle. Due to the weak binding, proteins in the soft corona can dissociate and proteins with lower concentration but higher affinity bind to the nanoparticle forming the hard corona. Adapted from [36].

Interaction of NPs and proteins in serum is determined by both serum and NP characteristics: for example, temperature [37] and pH on the serum side, size, shape and surface composition on the NP side [38].
The protein corona constitutes the "biological identity" of the NPs, that is what cells really see when NPs approach them. Thus, it is of paramount importance to understand the effects that proteins on NP surface can have on the body response. Depending on the specific application the protein corona could be either useful or dangerous. For example, if NPs are functionalised for targeted delivery applications, the adsorption of proteins on their surface alters their interactions with the specific target loosing delivery efficiency. Moreover NPs could be recognised by macrophages and removed from blood circulation, affecting again the delivery efficiency and requiring a higher administered dose. Conversely, adsorption of protein on certain kind of NPs could improve their biocompatibility [39].
If the formation of a protein corona is uncontrolled, designed functionality is lost so that it becomes of paramount importance to control the adsorption of proteins on NPs. Different strategies have been used to prevent corona formation on NPs. PEGylation of NPs, which consists in the functionalisation of the NP surface with PEG molecules, is considered an efficient approach to reduce protein adsorption [40]. The literature on this topic is very vast and

focuses on different aspects of the problem starting from the design of the functionalisation [41] and arriving to toxicity [42] of PEGylated NPs. What emerges from experiments and theory is that the anti-fouling properties of PEG, as well as of other stealth polymers, are due to both steric and hydrophilic effects. As for the former contribution, different conformations of PEG chains can be obtained varying PEG chain length and density on the grafted surface [43]. For what concerns the influence of hydrophilicity, variations in physico-chemical properties of anti-fouling polymers, particularly for PEG which has the tendency to oxidise, produce changes in surface hydration, thus influencing the polymer–protein interaction [44].
Zwitterionic materials proved even more efficient as anti-fouling coatings due to the presence of both positive and negative ions in the same molecule. The strong solvation shell around ions guarantees a more stable surface hydration compared to the simple hydrogen bonding network formed around hydrophilic polymers [45]. The most studied zwitterionic polymers are those containing betaine groups. Sulfobetaines, carboxybetaines and phophobetaines identify three classes of zwitterionic polymers which have been and still are intensively studied both experimentally and with molecular simulations. Moyano *et al.* [46], for example, recently designed and tested zwitterionic molecules with sulfobetaine terminals and tunable hydrophobicity. Small gold NPs functionalised with these molecules showed good resistance to hard protein corona formation.
Controlled adsorption of proteins onto the NP surface can be used to guide NPs in their journey to and inside the cells. Thus, it is of paramount importance to understand which characteristics of NPs drive the interaction with proteins. In this perspective computational studies can coordinate with experiment to first track the composition of the corona and then study if a pattern exists to drive the NP-protein interaction. Thus, being able to functionalise NPs with specific molecules which bind only selected proteins will allow to control the fate of NPs in the body and finally in the cell.

1.2.2 Interaction with cell membranes

The final target for NPs are cells or organelles inside cells. The interaction between NPs and cells is non-trivial and strongly depends on the type of cell, its environment and, on the NP side, on size, shape and surface composition [47]. Cells are delimited by the cell membrane which works as a barrier dividing the interior and exterior of the cell. Trafficking in and outside the cell is controlled by the cell membrane. Small and slightly polar compounds can passively cross the cell membrane. Polar or charged small molecules can be exchanged using trans-membrane proteins which serve as membrane channels. Larger molecules are internalised in cells by endocytosis: the cell membrane engulfs the object to be transferred forming a vesicle which eventually detaches from the membrane and travels in the interior of the cell. When large molecules need to be transferred to the exterior of the cell exocytosis comes into play: a vesicle is formed around the molecules and, when it reaches the cell membrane, fuses with it expelling its content. It has been found that NPs are able to penetrate cells both *via* direct permeation, that is NPs can pass through the cell membrane without being trapped into liposomes, and endocytosis [48, 49] which is the major translocation pathway. Direct permeation would be preferable to endocytosis since NPs cannot often

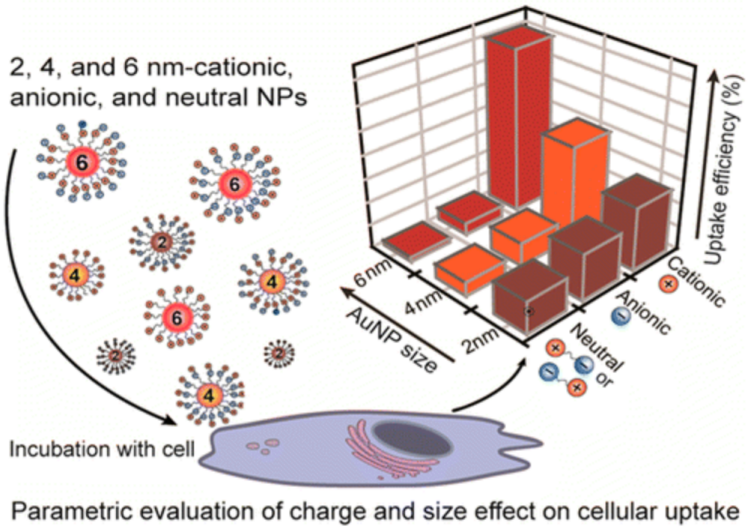

Figure 3: Schematic picture which summarises the interplay between size and surface charge in cellular uptake. Bigger cationic nanoparticles are most efficiently taken up by cells. Neutral zwitterionic nanoparticles show the smallest cellular uptake. Taken from [55].

escape from lipid vesicles, thus reducing delivery efficiency. A large amount of experimental literature exists on NP-cell interaction, most of which is focused on the uptake efficiency of NPs different in size, shape and ligand coating [50]. Recently, Nakamura *et al.* [51] reviewed both experimental and computational literature on passive permeation of NPs across cell membranes, focusing on the characteristics of NPs which are thought to be relevant for spontaneous internalisation. Size seems to play a crucial role in selecting the cell penetration mechanism: large NPs with size in the range of tens to hundreds of nanometers are usually internalised *via* endocytosis while for small NPs (less than 20 nm) passive penetration seems to be favoured. Shape could be another key factor: spherical NPs are usually taken up more efficiently than rod-like NPs due to larger membrane deformations which occur in NP internalisation *via* endocytosis. Surface characteristics of NPs also play a crucial role in NP uptake, in particular effects of charge have been largely investigated. Cationic and anionic NPs, that is NPs owning a net positive or negative charge, respectively, have been shown to enter cell *via* different endocytosis mechanisms [52, 53, 54]. Zwitterionic NPs, instead, seems to be taken up directly [55]. Not only individual physico-chemical properties, but also their combination can influence cellular uptake of NPs, especially in the sub-10 nm size scale [55] (see figure 3).
The large variability in experimental systems, like cell line, NP core composition, different ligand shells and so on, makes the comparison between experimental results non-trivial. Then, model systems need to be considered to try to overcome the problem. As cell membranes are mainly composed of lipids, liposomes have been naturally chosen as model systems. They can be synthesised with different lipid compositions and size thus allowing to mimic different kinds of cell membranes. Removing a large part of the complexity of the system, fundamental NP–membrane interactions can be studied and a molecular level interpretation of the process can be achieved with computational tools like molecular dynamics simulations. Typical

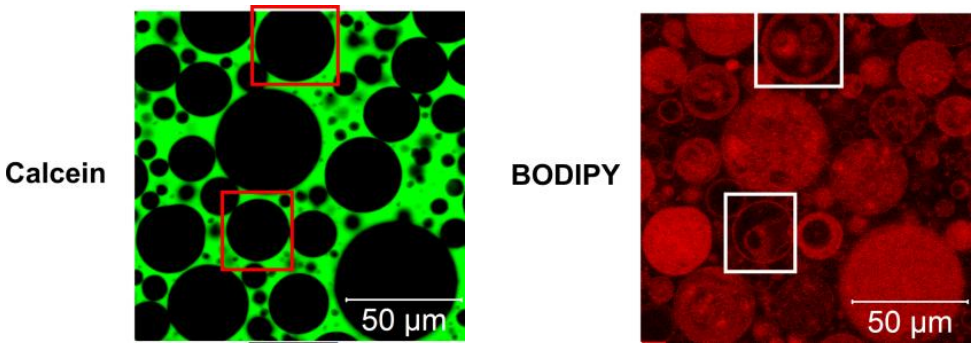

Figure 4: Confocal microscopy images of BODIPY-labelled NPs interacting with multilamellar DOPC vesicles. Left: calcein outside the liposomes cannot penetrate the vesicles once NPs are added to the solution. Right: BODIPY-labelled NPs interact preferentially with the lipid membrane and can non-disruptively penetrate in the liposome interior co-localising with the inner lipid membranes. Adapted from [57].

experiments to probe the NP–membrane interaction are based on the leakage of fluorescent dyes from liposomes. Using simple model systems it is possible to selectively vary the parameters whose influence on the interaction with liposomes is to be studied. For example, the effect of charge has been investigated in many studies. Cationic NPs are usually reported to be more disruptive than anionic NPs [56], [57]. In fact, for example, anionic NPs can non-disruptively penetrate lipid membranes of liposomes as shown in figure 4. Not only NP properties but also membrane characteristics can influence the NP-cell interaction. One of the possible factors affecting NP-cell interaction is membrane uneven composition: cell membranes, in fact, present structures with different rigidity, name lipid rafts which contain a large amount of cholesterol along with negatively charged lipids. Lipid rafts can move in the fluid lipid matrix of cell membranes and eventually come in contact with NPs. To study the influence of different lipid phases on the NP–membrane interaction, liposomes or supported lipid bilayers with phase separated domains have been used. Experiments with zinc oxide NPs and multicomponent liposomes showed that NPs seem to penetrate across lipid disordered phases and in proximity of phase boundaries [58]. Conversely, lipid-functionalised and cationic superparamagnetic iron oxide NPs were found to only adhere to the lipid membrane of a supported lipid bilayer containing a mixture of cholesterol, neutral and negatively charged lipids [59]. Both kinds of NPs were found to prefer cholesterol rich membranes, with lipid-functionalised NPs irreversibly binding to the bilayer surface.
Even if a bit more delicate compared to lipid vesicles, supported lipid bilayers offer a great platform to compare experiments and simulations. Using molecular dynamics simulations, a mechanism for the spontaneous penetration of small NPs through lipid bilayers [60, 61] was proposed, which involves adsorption on and subsequent progressive insertion in the lipid membrane. With analogous computational techniques, pristine fullerene NPs have been shown to spontaneously penetrate the lipid bilayer by hydrophobic effect [62]: fullerenes aggregate in the water phase and penetrate the lipid membrane as an aggregate which then dissolves in the lipid membrane core [63].
The increasing interest in the field has produced a vast literature which contributed to elucidated some important mechanisms regarding the

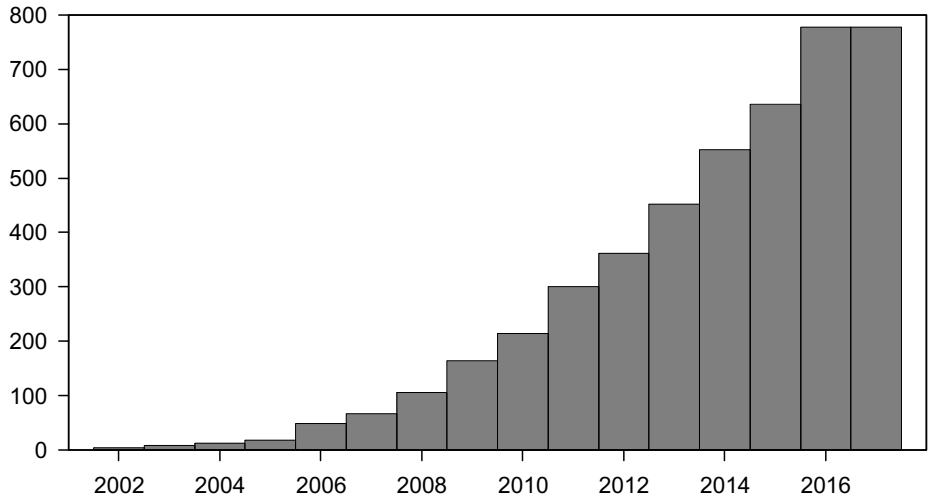

Figure 5: Number of publications on the topic gold nanoparticles in biomedicine. Results correspond to the search of "gold nanoparticle* biomedi*" on Web of Science from 2002 to 2017.

NP-membrane. However the same interest has led to the enlargement of the studied systems, together with the development and application of new techniques, increasing their variability and thus making it more difficult to interpret the results.

1.3 Gold nanoparticles – a paradigm in biomedical applications

Among the large variety of materials which proved useful for applications in biomedicine, gold has attracted greater and greater attention over the years as demonstrated by the exponentially growing number of publications in the field (see figure 5) The increasing interest towards gold for biomedical applications has its basis on the necessity of inert and non-toxic materials in the biological environment together with a wide range of tunable properties for different applications. Many reviews have been written on gold and its applications in biomedicine [64, 65, 66]. Here we summarise the key properties which attracted researcher's interest in gold nanoparticles (AuNPs).
AuNPs can be synthesised in a multitude of shapes and sizes. For biomedical applications nanorods, nanospheres, nanocages and core–shell NPs are typically used. Different synthesis methods have been developed and refined to obtain low polydispersity in the size distribution. In order for NPs not to precipitate in aqueous solution, AuNPs are usually capped with citrate molecules which form an adsorbed layer on the NP surface. The surface of AuNPs can also be functionalised with different kinds of molecules; NPs with net positive or negative charge as well as functionalised with neutral hydrophilic ligands can be produced. Biological molecules such as single stranded DNA and small peptides can also be bound to AuNPs. To stably functionalise AuNPs, ligands are usually thiolathed, that is a they contain a carbon-bonded sulphydryl (R–SH) group. The sulphur atom can be deprotonated and form a strong bond with Au atoms.
The importance of a gold core for NPs to be used in biomedicine is related to the unique properties that gold manifests at the nanoscale: AuNPs subject to

electromagnetic radiation exhibit a localised surface plasmon resonance whose frequency depends on NPs size, shape and surface functionalisation. Acting on these parameters it is possible to shift the plasmon resonance in the NIR region of the electromagnetic spectrum; in this region tissues are transparent to radiation which thus penetrates deeper in the body.
Due to the sensitivity of the surface plasmon resonance to the chemical environment, AuNPs find application as sensors for biomolecules. The surface of the NPs can be conjugated with selective molecules so that complementary molecules will attach to the NP surface: the resulting shift in the plasmon resonance can be related to the concentration of the binding molecules.
Thanks to the high light–to–heat conversion, AuNPs can be used as heating source for thermal therapy of cancer. Once irradiated with a laser source at the plasmon resonance, AuNPs absorb radiation and convert it into heat; heat is then released to the tumour cells to kill them.
AuNPs have attracted attention also in the theoretical community, especially the computational branch. First principle calculations have been performed to study the atomic structure of gold nanocluster both bare and functionalised. New models have also been parameterised to exploit molecular dynamics simulation to study the biological behaviour of NPs.

1.4 Aim of this thesis

The growing interest towards applications of NPs in biomedicine has led to a rapid expansion of the field. New challenges in developing materials with higher and higher efficiency enlarged the number of systems and conditions that have been experimentally realised and tested. This expansion undoubtedly improved the knowledge on the use of NPs for biomedical applications, but on the other hand, the large variety of systems under study made it difficult to directly compare results and draw general guidelines for the synthesis of NPs useful in biomedicine.
AuNPs have become a standard in many experimental as well as computational studies and a large bulk of literature exists on this topic. In this work we use molecular dynamics simulations to investigate, at molecular level, the interaction between small gold NPs and both proteins and lipid bilayers.

1. When NPs are injected in the blood stream they come in contact with biomolecules such as lipids and proteins. Proteins are particularly relevant for the use of NPs in biomedicine since adsorption of certain proteins on external objects is the first step of opsonisation, a process which leads to NP clearance from blood stream. In this thesis we investigate the interaction between a monolayer–protected AuNP and **human serum albumin**, the most abundant protein in human blood.

2. If no protein adsorption takes place, functionalised NPs can reach their target cells. The interaction between NPs and cell membrane is dependent on numerous NP and membrane characteristics. Since the interplay of these elements is non-trivial, to study the NP–cell interaction at a fundamental level, the system must be kept as simple as possible. Here we report on the **mechanism** by which a monolayer–protected AuNP fuses with a mono-component lipid bilayer.

3. Among the properties of NPs which can influence the NP–membrane interaction, charge plays an important role. Experimental results on this topic generally report positively charged NPs to be more disruptive than negatively charged NPs, thought the mechanism is still unclear. In this thesis we investigate, both experimentally and with computational tools, the effect of **charge** on the disruptive character of monolayer–protected AuNPs interacting with mono-component lipid membranes.

1.5 Content of this thesis

In this chapter we introduced the concept of nanoparticles, their key properties and their applications in the biomedical field. We also discussed their fate when used *in vivo*, focusing in particular on the interaction of nanoparticles with proteins and cells, and cell membranes in particular. Eventually, we zoomed in gold nanoparticles which are a paradigm in biomedical applications.
In chapter 2 we introduce the molecular dynamics technique, starting from its statistical physics basis. We then focus on metadynamics, an enhanced sampling technique based on classical molecular dynamics which can be used to sample rare events and reconstruct the free energy surface of a system. Then we introduce the concept of force field and illustrate the main characteristics of the most popular force fields used in biological simulations.
In chapter 3 we enter in the details of the system studied in this thesis. We describe the model of the nanoparticles which we developed and used in this thesis. We consider monolayer-protected nanoparticles with a gold core functionalised by different kinds of ligands. First the model of the core of the nanoparticle and then of the ligands are shown. Both negatively and positively charged nanoparticles are modelled to study the nanoparticle-membrane interaction, while neutral zwitterionic ligands have been considered to study their interaction with proteins.
In chapter 4 we describe the interaction between the most abundant protein in blood serum, human serum albumin, and two kinds of zwitterionic nanoparticles differing in hydrophobic content. We show that increasing the hydrophobicity of the terminal group of zwitterionic ligands induces a conformational change in the ligands which influences the nanoparticle-protein interaction: the most hydrophobic ligand folds and causes more hydrophobic nanoparticles to interact more strongly with the protein.
In chapter 5 we study the interaction of nanoparticles with different ligand arrangements on the nanoparticle surface and a model lipid membrane. We show that anionic nanoparticles can penetrate in neutral lipid membranes and stably reside in the membrane core.
In chapter 6 we investigate the effect of charge on the nanoparticle-membrane interaction using both experiments and computer simulations. We perform experiments of dye leakage from calcein-loaded liposomes which were put in solution with either anionic or cationic nanoparticles. We found that the sign of the charge of gold nanoparticles does not influence their interaction with neutral lipid membranes. We sustain this finding with molecular dynamics simulations which show that two nanoparticles differing only in the charge sign interact with a neutral lipid membrane with the same mechanism and induce the same perturbations on the membrane.

2 MOLECULAR DYNAMICS SIMULATIONS

Contents

The time evolution of a classical system is described by Newton's equations of motion. At molecular level quantum mechanics should be considered, whenever electron degrees of freedom are important: this is the case, for example, of the simulation of chemical reactions. However, the time evolution of large biological systems at equilibrium is most often described by classical models.
Solving the equations of motion for a system with a large number of atoms, as the ones considered in this thesis, is non-trivial and numerical methods are required. This is where molecular dynamics (MD) comes into play: given a set of initial conditions and interactions, the time evolution of the system can be obtained from the numerical integration of the equations of motion. In the first part of this chapter the basic concepts of statistical mechanics underlying MD simulations will be summarised (taken from *Computational biochemistry and biophysics* [67]). Then the technique itself will be described together with the interaction models necessary to describe our systems. In the final part of this chapter advanced simulations methods will be introduced. For a more detailed description of MD simulations the reader is addressed to the books by Allen and Tildesley [68] and Frenkel and Smit [69]

2.1 Basic concepts in molecular dynamics

Molecular dynamics is a computational method used to study the evolution in time of a system of molecules with given interparticle interactions. The method resides on statistical basis which are outlined in the following subsection.

2.1.1 Statistical mechanics basis of molecular dynamics

In the Hamiltonian description, the equations of motion can be derived from the Hamiltonian function H of the system. In general H is a function of

coordinates $\mathbf{q}$, momenta $\mathbf{p}$ and time t. If the potential energy function is independent of time, the Hamiltonian represents the total energy of the system

$$H = H(\mathbf{q}, \mathbf{p}) = K(\mathbf{p}) + U(\mathbf{q}) = \sum_i \frac{p_i^2}{2m_i} + U(\mathbf{q}) \tag{2.1.1}$$

where $K(\mathbf{p})$ is the kinetic energy and $U(\mathbf{q})$ the potential energy of the system. A point described by the ensemble of coordinates and momenta of the N points in the system is a *phase space point*. According to statistical mechanics, macroscopic properties of a system with a large number of particles can be computed from their phase space coordinates as

$$\langle A(\mathbf{q}, \mathbf{p}) \rangle = \int_\Omega d\Omega' \rho(\mathbf{q}, \mathbf{p}) A(\mathbf{q}, \mathbf{p}) \tag{2.1.2}$$

where Ω is the volume of phase space occupied by the system. The values of the property A are weighted by the probability function ρ evaluated at each point in phase space

$$\rho(\mathbf{q}, \mathbf{p}) = \frac{e^{-H(\mathbf{q},\mathbf{p})/k_B T}}{\int_\Omega d\Omega' e^{-H(\mathbf{q},\mathbf{p})/k_B T}} \tag{2.1.3}$$

k_B being the Boltzmann constant and T the absolute temperature. The denominator of equation 2.1.3 is called partition function.
The sampling of $\rho(\mathbf{q}, \mathbf{p})$ (2.1.3) for each point in phase space is non-trivial. A workaround for the computation of macroscopic properties is to follow the time evolution of the system in the phase space. Thus, the average of the quantity A becomes

$$\langle A(\mathbf{q}, \mathbf{p}) \rangle = \frac{1}{\tau} \int_0^\tau dt\, A(\mathbf{q}(t), \mathbf{p}(t)) \tag{2.1.4}$$

where τ is the time for which the values of A are known. The time evolution of the system, described by the set of phase space points $\{\mathbf{q}(t), \mathbf{p}(t)\}$, is obtained integrating its equations of motion. If the system is *ergodic*, that is it can visit every point in phase space, the average of A computed from the probability ρ (equation 2.1.2) and the time average of A (equation 2.1.4) are equivalent, provided that the latter is performed on an infinitely long trajectory. The previous statement is known as the *ergodic hypothesis* and theoretically justifies the use of molecular dynamics simulations to compute averages in the sense of equation 2.1.2, as long as the simulation time is ergodically long enough.

2.1.2 Working principles of molecular dynamics

To solve Newton's equations of motion a numerical integrator is required. Time is discretised in time intervals Δt and positions and velocities are obtained from previous values with a finite-difference method. Different algorithms have been proposed to solve the equations of motion numerically. The Verlet [70], the leap frog [71] and the velocity Verlet [72] integrators are

the most common and are based on the Taylor expansion to the second order of the trajectory $\mathbf{r}_i(t)$ for each particle i in the system

$$\mathbf{r}_i(t+\Delta t) \approx \mathbf{r}_i(t) + \mathbf{v}_i(t)\Delta t + \frac{\mathbf{f}_i(t)}{2m_i}(\Delta t)^2 \tag{2.1.5}$$

The Verlet algorithm reads

$$\mathbf{r}_i(t+\Delta t) = 2\mathbf{r}_i(t) - \mathbf{r}_i(t-\Delta t) + \frac{(\Delta t)^2}{m_i}\mathbf{f}_i(t)$$
$$\mathbf{v}_i(t) = \frac{\mathbf{r}_i(t+\Delta t) - \mathbf{r}_i(t-\Delta t)}{2\delta t}$$

The updating equations for the leap frog integrator are

$$\mathbf{r}_i(t+\Delta t) = \mathbf{r}_i(t) + \mathbf{v}_i(t+\Delta t/2)\Delta t$$
$$\mathbf{v}_i(t+\Delta t/2) = \mathbf{v}_i(t-\Delta t/2) + \frac{\Delta t}{m_i}\mathbf{f}_i(t)$$

In the velocity Verlet algorithm positions and velocities are update according to

$$\mathbf{r}_i(t+\Delta t) = \mathbf{r}_i(t) + \mathbf{v}_i(t)\Delta t + \frac{(\Delta t)^2}{2m_i}\mathbf{f}_i(t)$$
$$\mathbf{v}_i(t+\Delta t) = \mathbf{v}_i(t) + \frac{\Delta t}{2m_i}(\mathbf{f}_i(t) + \mathbf{f}_i(t+\Delta t))$$

The velocity Verlet is the most accurate algorithm though it is the most computationally expensive.
Once the algorithm is chosen, initial conditions are necessary to start the computation of the trajectory. The initial set of positions $\mathbf{r}(0)$ and velocities $\mathbf{v}(0)$ is assigned to the atoms in the system. While positions are usually taken from experimental structures, as in the case of proteins, or assigned by design, as in the case of this thesis for AuNPs, velocities are typically determined extracting random values from the Maxwellian distribution of velocities at the temperature of the simulation. The time step for integration is chosen based on the characteristic motions of the atoms in the system. For example, if hydrogen atoms are explicitly considered, the time step should be chosen so as to correctly sample the vibration of the bond between the hydrogen atom and the heavy atom to which it is bound in the molecule. The period of this vibration is of the order of $\tau \sim 10$ fs. A good rule of thumb for the choice of Δt is $\tau/\Delta t \approx 20$. In the case of hydrogen, then, an appropriate time step would be $\Delta t \approx 0.5$ fs. The interactions between atoms in the system are computed and positions and velocities updated according to the chosen algorithm. The integration stops when the number of integration steps previously set has been reached. A schematic representation of an MD simulation is shown in figure 6.

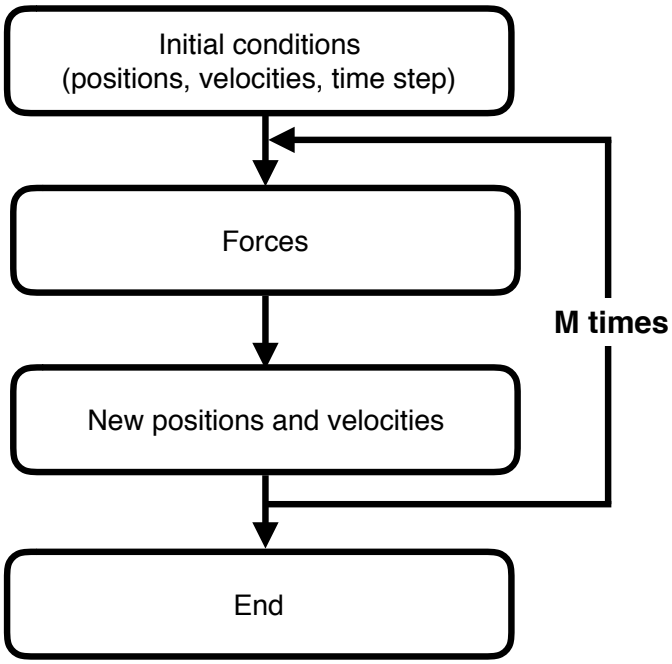

Figure 6: Schematic representation of a molecular dynamics simulation. The integration process is repeated M times before the simulation ends.

2.2 Details on molecular dynamics simulation

When large systems are simulated, the computation of interactions is the most expensive part of the algorithm. To save some computational time some workarounds can be used.

Cut-offed interactions In typical MD simulations of large biological systems the interactions between atoms which are not bound together, namely *non-bonded* interactions, are pairwise and depend only on the separation between the atoms, r.
If the interaction potential decreases in r faster than r^{-d}, with d the dimensionality of the system, the interaction is said to be *short ranged*. In this case only the closest atoms contribute to the interaction. It is thus possible to choose a cut-off distance beyond which the interaction can be set to zero. However, doing so, atoms close to the cut-off distance suffer from large forces due to the discontinuity in the potential function. To fix this problem different methods have been implemented, the most used of which are the shift and switch methods. In the former case the potential function is shifted to the cut-off value before the cut-off distance, while for the latter solution two cut-off distances are needed and the potential is smoothly change from its current value to the cut-off value between the first and the second cut-off (see figure 7).
With *long range* interactions, as in the case of the electrostatic potential, interactions are relevant also for large distances. In this case the use of cut-offed potential functions is to handle with care since it can lead to mistakes in the behaviour of the simulated system. The proper treatment of long range interactions is discussed in subsection 2.4.1.

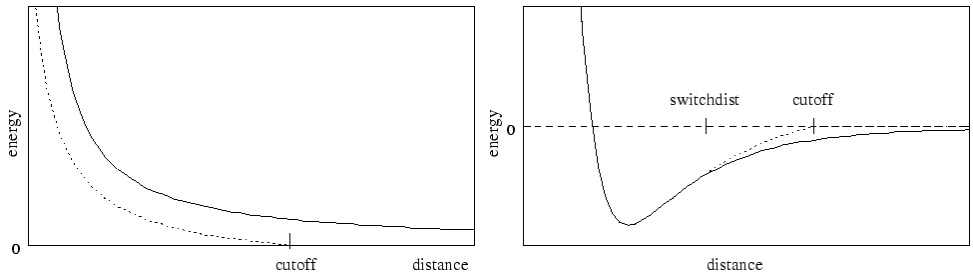

Figure 7: Example of shifting (left) and switching (right) modification to cut-offed interactions. In the former case the potential is shifted to its value at the cut-off. Since forces are computed as derivatives of the potential, no effects on force calculation are introduced. In the latter case the potential function is smoothly switched to its cut-off value in a range between *switchdist* and *cutoff*.

Neighbour list When forces are computed, it is necessary to search for all interacting pairs of atoms. This is extremely expensive in terms of computational cost. Introducing a cut-off for interactions improves the computational efficiency but the calculation of distances between the atoms within the cut-off still limits the computational efficiency. However it has to be considered that if two atoms were interacting at a certain step, the next step they will not be much further from each other. Thus a list of neighbour atoms can be compiled at the beginning of the simulation for each atom of the system and this list can be updated only after a certain number of simulation steps. Forces can then be computed only for the atoms in the list without repeating the distance calculation at each time step, thus saving computational time. However, some particles near the boundary could enter or exit the cut-off region so that the corresponding interactions could be added or neglected. To ameliorate the calculation of the interactions a buffered neighbour list can be considered computing interactions also for those atoms which lie within a spherical region of larger radius (see figure 8). The thickness of the buffer, which depends on the typical diffusion velocity of the centre of mass of the molecules in the system, should be chosen so as to balance precision and computational efficiency. Another key parameter is the update frequency of the neighbour list compilation; in principle it could be set at the beginning of the simulation and kept constant for the entire simulation. However, a better choice is to update the neighbour list whenever an atom travels over a distance that is longer than the thickness of the buffer.

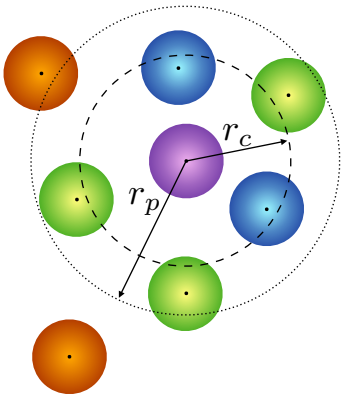

Figure 8: Schematic representation of a buffered cut-off list construction. Particles of the same colour have their centre in different shells. Blue particles belong to the cut-off shell of radius r_C and are therefore included in the calculation of the interactions. Green particles, whose centres lie within the cut-off shell and the pair cut-off shell (defined by r_p), are inserted into the neighbours pair list. Orange particles belong to neither of the two shells and so are not considered for force calculations.

Periodic boundary conditions Experimental systems are much larger than their simulated counterpart. This introduces artificial boundaries in the system due to its finite size. To avoid surface effects introduced by finite size, periodic boundary conditions are applied: under these conditions the behaviour of the system is closer to that of a system of the same size embedded in an infinite system.
Molecular dynamics simulations are carried out in a simulation box whose shape is determined by the symmetry of the system. Applying periodic boundary conditions to the system means replicating the main simulation box an infinite number of times along each side of the box. Then, the central simulation box is surrounded by identical copies of itself. When a particle in the central simulation box crosses one of the boundaries, its copies in all other boxes move accordingly, so that the number density of particles is conserved in the central box, as shown in figure 9. Application of periodic

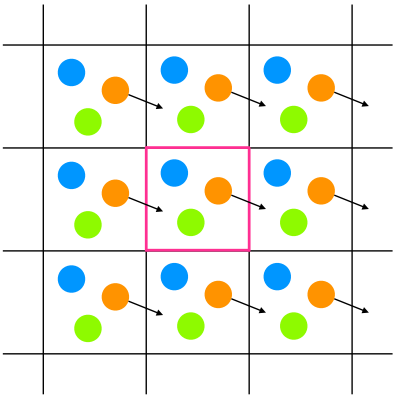

Figure 9: Schematic representation of periodic boundary conditions for a 2D system. The central box (pink contour) is replicated along each side of each box. The virtual movement of particles is represented by black arrows.

boundary conditions introduces some limitations: the size of the cell should be at least twice larger than the cut-off radius of the potential so that each atom interacts with only one image of all other atoms and does not interact with its own image; the characteristic length scale of the system should be smaller than the size of the box so as to be correctly sampled.

Molecular dynamics at constant temperature and pressure The original MD technique was implemented to study the classical Hamiltonian time evolution of systems with fixed number of particles N in a volume V. Under these conditions the system is isolated and its total energy E is conserved. However, experiments are usually performed at constant temperature T and pressure p. The simplest way to implement these experimental conditions in MD simulations is to rescale velocities and positions in the standard simulations, to obtain constant temperature and pressure conditions, respectively.
As for canonical simulations (NVT statistical ensemble), the velocities of all the particles in the system can be rescaled by the same factor α which depends on a target kinetic energy K_t, chosen with a stochastic procedure from the canonical equilibrium distribution of kinetic energies. The details of the calculation of α can be found in the original paper by Bussi *et al.* [73].
Simulations at constant pressure can be performed applying a scaling to the coordinates of the system, concurrent with a volume scaling, as proposed by Berendsen *et al.* in 1984 [74]. The scaling factor depends on the isothermal compressibility of the system, on the variation of the instantaneous pressure with respect to the target pressure and on the barostat relaxation time. Even if

the Berendsen barostat succeeds in driving the system to the target pressure, it fails in reproducing the fluctuations of the instantaneous pressure. To retrieve the correct behaviour of pressure fluctuations the Parrinello-Rahman approach [75] can be adopted: both the shape and size of the box are allowed to change during the simulation and the corresponding term is introduced into the Lagrangian of the system through a coupling constant related to the relaxation time of the system.

2.3 Metadynamics

Despite the various techniques that have been implemented to speed up MD simulations, the major limitation in the use of MD simulations is the sampled time. Considering typical time steps in the range 1-30 fs, simulated times reach at most tens of μs. It is not unusual, especially for biological systems, that the free energy surface (FES) associated to the system shows many local minima separated by high free energy barriers. Thus, to explore the entire surface a large amount of time is required. Standard MD simulations are not able to successfully sample such a FES. Enhanced sampling techniques have been developed to overcome this problem. Metadynamics, a method proposed by Laio and Parrinello in 2002 [76] is one of them. The main idea under enhanced sampling techniques like metadynamics is to describe the FES using a small set of parameters instead of all atomic coordinates. These parameters, called collective variables (CVs), are functions of the atomic coordinates and must be chosen so as to represent the physics of the system. Moreover they should be able to distinguish between different states of the system. An example may be useful to clarify the concept. Let us consider the alanine dipeptide (ACE-ALA-NME), shown in figure 10. The different

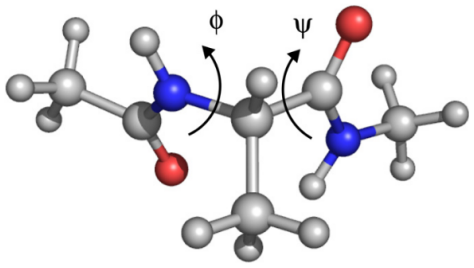

Figure 10: Alanine dipeptide. Backbone dihedral angles are denoted as ϕ and ψ.

conformations of the alanine dipeptide can be identified by the two dihedral angles ϕ and ψ instead of the coordinates of the single atoms in the molecule. It is thus possible to describe the FES of the system using the backbone dihedral angles as CVs. In vacuum the FES of the alanine dipeptide shows two minima, C_{7eq} and C_{7ax} (shown in figure 11), which are separated by free energy barriers around 33 kJ/mol, much larger than thermal energy $k_B T = 2.5$ kJ/mol at 300 K. If one assumes that an Arrhenius-like equation can describe the transition from one minimum to the other and that the frequency prefactor corresponds at most to the carbon-carbon bond vibration ($5x10^9$ 1/s), the rate of $7x10^3$ events per second is obtained for the transition between the two free energy minima. This means that simulations in the scale of milliseconds are necessary to sample at least one transition. These timescales are incompatible with standard MD simulations. The working principle of metadynamics is rather simple: to help the system escaping from free energy

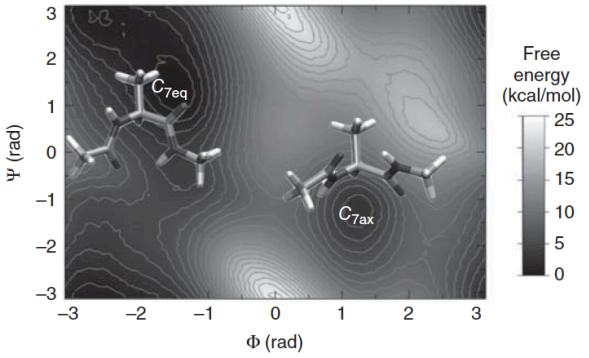

Figure 11: 2D free energy landscape for the alanine dipeptide as a function of the two backbone dihedral angles ϕ and ψ. Each line accounts for 1 kcal/mol difference in free energy. The two main minima, namely, C_{7eq} and C_{7ax}, are shown. Taken from [77].

minima, a repulsive Gaussian of width δs and height w is added to the energy of the system every t_G MD steps at the position $S(\mathbf{q}(t))$ in the CV space. The potential is history dependent since trace of the added Gaussian is kept in the time dependent potential

$$V_G(S(\mathbf{q}(t)), t) = \sum_{t'=t_G, 2t_G, \ldots < t} w \, exp\left(- \sum_{i=1}^{N_{CV}} \frac{(S_i(\mathbf{q}(t)) - S_i(\mathbf{q}(t')))^2}{2(\delta s_i)^2} \right) \quad (2.3.1)$$

When the added energy is sufficient to reach the shallowest saddle point, the system is likely to escape the trap through this saddle. An explanatory picture of the procedure is shown in figure 12. As more and more Gaussian are added, the FES is increasingly flattened.
Looking at figure 12, two possible ways to use metadynamics emerge [78]:

- if the simulation is stopped as soon as the system escapes a free energy minimum, then the height of the escaping barrier can be estimated knowing the bias potential at the time the simulation is stopped (blue curve in the lower panel of figure 12).

- the FES in the CVs space can be reconstructed from the potential in equation 2.3.1 assuming the limit of very long simulation time. In this limit the motion of the CVs on the FES becomes diffusive (orange curve in the upper panel of figure 12).

Due to its different applications and quite simple working principle, metadynamics is a powerful technique. However, the choice of CVs is not trivial. The same problem holds for the choice of metadynamics parameters, i.e. the height and width of the Gaussians and their deposition rate. The number of CVs should be kept as small as possible, taking into account the necessity to use suitable parameters to discriminate different states of the system. As for metadynamics parameters, they should be chosen so as to guarantee a good balance between accuracy in the reconstruction of the FES and efficiency in the simulation time: a large Gaussian width or high deposition rate will ensure rapid sampling times at the expense of small errors in the profile estimation; if Gaussians are added at low frequency or their width is too small, a more accurate reconstruction of the FES is possible but longer simulations times are needed.

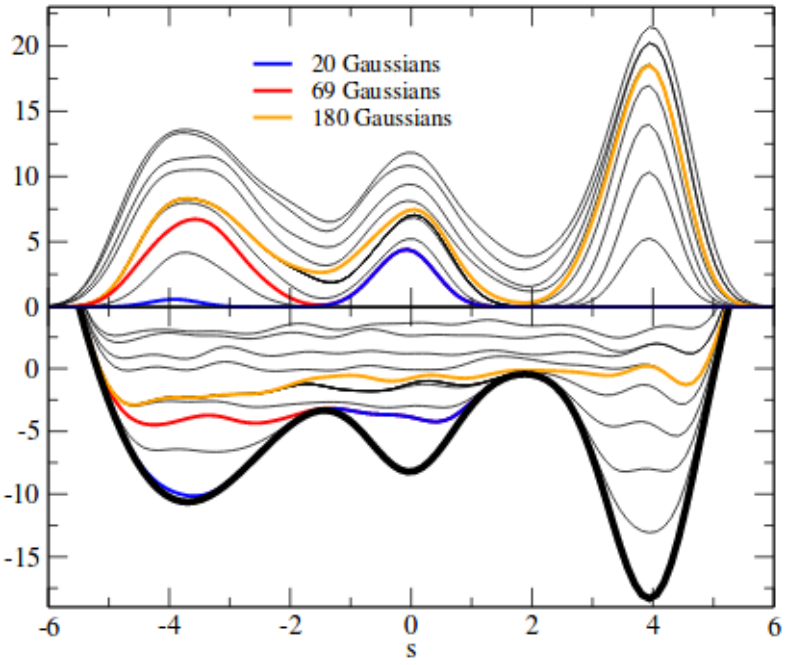

Figure 12: Example of a free energy profile reconstructed from a metadynamics simulation. The time evolution of the bias potential V_G is shown in the upper panel as a function of the collective variable s. The free energy profile is shown in the lower panel as a black thick line. The time evolution of the 'filling' potential is shown also shown in the lower panel. As more and more Gaussians are deposited, the system escapes the first minimum (blue line) and falls in a second minimum. When the second minimum is filled (red line) the system can explore the deepest well. Finally, the free energy profile is filled and the dynamics becomes diffusive (orange line). Taken from [78].

2.4 Force fields

In the previous sections a quite general description of the methods used to solve the equations of motion and sample the FES of a system of particles has been given. These methods are independent on the system itself and can be used to describe very different systems and phenomena. What is peculiar of the system under study is the set of parameters and potential energy functions that govern the interactions between the particles in the system: the *force field*. If the motion of electrons is averaged out, that is the Born-Oppenheimer approximation is applied, only interactions between atomic nuclei can be considered. *Classical* force fields deal with the description of interactions in such systems. Different levels of description are possible for bio-molecular systems as the ones studied in this thesis: the atomistic one, in which all atoms are described explicitly and maintain their chemical identity, and the coarse-grained (CG) level in which groups of atoms are treated as a unique particle which properties are chosen so as to reproduces the main physical and chemical properties of the group itself. In subsection 2.4.1 we will provide a summary of the main characteristics which are common to classical force fields, independently on their resolution, while in subsections 2.4.2 and 2.4.3 a detailed description of the atomistic and coarse-grained force fields we used will be given.

2.4.1 Common features of classical force fields

Molecular dynamics is a powerful technique which can be applied to study a wide variety of systems. What characterises each system is the set of potential energy functions which describes the interactions among the particles in the system itself. Functional forms for potential energy are the same for all the systems within a class but their parameters change to reproduce the physico-chemical properties of each system. Since the number of systems which can be studied is almost infinite, it is impossible to parameterise each system independently. Thus a small set of standard systems (training set) is used to parameterise the force field in specific conditions, for example within a range of temperature ad pressure, and the derived parameters can be used to describe other systems in other conditions. For example, the parameters derived for a carbon atom in an alkyl chain can be used to represent both a carbon atom in a polymer chain and a carbon atom in a lipid tail. This procedure is a fundamental characteristics of force fields and goes under the name of *transferability* of the force field parameters.

Functional forms Particles in molecules are subject to two kind of interaction potentials: *bonded* interactions, that connect particles within a molecule, and *non-bonded* interaction to which all particles in the system are subject.

Typical **bonded** interactions (U_{bonded}) involve up to four particles and include terms to describe bonds (U_b), angles (U_a) and dihedral angles (U_d) formed within a molecule

$$U_{bonded} = U_b + U_a + U_d = \tag{2.4.1}$$
$$= \frac{1}{2}\sum_{bonds} k_{bi}(l_i - l_{0i})^2 + \frac{1}{2}\sum_{angle} k_{ai}(\theta_i - \theta_{0i})^2 + \frac{1}{2}\sum_{dihedrals} V_n(1 + cos(n\omega - \gamma))$$

In equation 2.4.1 k_{ib} and k_{ia} are the elastic constants for bonds and angles, respectively. The equilibrium values for bonds and angles are l_{0i} and θ_{0i}, respectively. As for the dihedral potential, γ is a phase factor, usually chosen so that the potential energy is non-negative, n is the multiplicity, equivalent to the number of minima in the energy term, and V_n is the potential energy weight associated to the n-th component of the series. Different functional forms for the angle potential exist as well as for the dihedral potential (see for example the GROMACS manual http://manual.gromacs.org/documentation/).

Non-bonded interactions describe the Van der Waals and the electrostatic contributions and can act both between particles within the same molecules and between particles belonging to different ones. A restriction is applied to particles in the same molecule: non-bonded interactions are computed only for those particles being separated by a certain number of bonds which depends on the force field (see subsections 2.4.2 and 2.4.3 for further details). Van der Waals interactions can be written as a sum of an attractive part, due to London dispersion forces and described by a r^{-6} dependence on the separation r between the particles, and a repulsive part which is empirical and accounts for the fact that electron clouds cannot overlap. The repulsive part is represented by a $r^{-\alpha}$ dependence on the interparticle distance, with α usually equal to 9 or 12. For the force fields used in this thesis α is always equal to 12. The Van der Waals potential is called Lennard-Jones and reads

$$U_{LJ} = 4\epsilon\left[\left(\frac{\sigma}{r}\right)^{12} - \left(\frac{\sigma}{r}\right)^{6}\right] = \frac{C_{12}}{r^{12}} - \frac{C_6}{r^6} \tag{2.4.2}$$

where ϵ is the value of the potential at its minimum and σ is a parameter related to the position of the minimum of the potential. Van der Waals interactions are short ranged and thus usually computed imposing a cut-off. The electrostatic potential between two charged particles i and j separated by a distance r_{ij} and bearing charge q_i and q_j, respectively, is

$$U_{el} = \frac{1}{2}\sum_{i=1}^{N}\sum_{j\neq i}^{N}\frac{1}{4\pi\epsilon}\frac{q_i q_j}{r_{ij}} \tag{2.4.3}$$

In typical biological simulations periodic boundary conditions are applied to the simulation box. Since electrostatic interactions are long ranged (as described in section 2.2) also the contributions to the electrostatic potential energy deriving from periodic images of the system should be included in the computation of the energy. Thus, an infinite number of terms should be included in the computation, making the evaluation of the electrostatic potential impossible. A very rough method to solve this problem consists in treating electrostatics as a short range interaction, thus considering a cut-off

distance beyond which the interaction is set to zero. This method is drastic but sometimes sufficient to produce physically meaningful results. When electrostatics becomes important to describe the physics of the system, other methods which preserve the long range character of the interaction are used. Some of the force fields we used in this thesis are based on this methods and in particular on the particle mesh Ewald (PME) one [79, 80]. The PME treatment of electrostatics is based on the possibility to separate the periodic form of the electrostatic potential into a short and a long range part, as demonstrated by Ewald in 1921 [81]. The short range contribution can be directly computed while the long range part is computed in the Fourier space using the fast Fourier transform method. This is possible because charges are assigned to discrete grid points in space. Despite this trick, the computational cost to include long range electrostatics is very high. For example, adding the long range contribution to electrostatics in the simulation of a simple lipid membrane in water (~23000 particles) degrades performances from about 3500 ns/day to 1700 ns/day, without and with PME, respectively.
Improving the computation of the electrostatic potential with the PME method is not always sufficient to correctly reproduce the effects of electrostatics. For instance, charges are usually assigned as point charges centred at the position of the atomic nuclei; this does not allow for the description of atomic polarisation. Instead, effects of orientational polarisability can be included in simulations. At the expense of higher computational cost, also electronic polarisation can be included using different methods as reviewed by Yu and van Gusteren [82].
As explained at the beginning of this subsection, different resolutions in the description of a system are possible. The choice usually depends on the length and time scales of the process under study. In the following subsections we will outline the force field we used in this thesis.

2.4.2 Atomistic force fields

Atomistic force fields treat each atom as a single unit, except for the hydrogen atoms bound to carbon atoms, which, depending on the force field, can be incorporated in a unique particle. Force fields in which all hydrogen atoms are treated explicitly are said *all atom* (AA) force fields; if carbon atoms and their hydrogens are incorporated in a single particle the force field is called *united atom* (UA). Biological simulations usually involve a large number of atoms, most of which represent water molecules. Thus, length and time scales which can be simulated are limited to a few nanometres and nanoseconds if one wish to obtain results in reasonable times.
Different atomistic force fields have been developed to better reproduce different classes of systems. Since bonded interactions are usually fitted on experimental crystal structures and vibrational spectra or ab initio calculations, there is not a great difference in their parameters. Non-bonded interactions, instead, are fitted on different experimental data, such as densities and heat of vaporisation, depending on the class of system which has to be simulated. Only self interaction parameters are assigned and interatomic interactions are computed using the so-called *combination rules*. Different force fields use different combination rules. In this thesis we use the AMBER force field for proteins [83] and the united atom version of the OPLS force field [84, 85] integrated with Berger lipid parameters [86, 87]. Both force fields use

geometrical combination rules, that is Van der Waals parameters for the interaction between atoms *i* and *j* are computed as $\epsilon_{ij} = \epsilon_i \epsilon_j{}^{1/2}$ and $\sigma_{ij} = \sigma_i \sigma_j{}^{1/2}$. Proper of each force field is also the treatment of the so-called *1-4 interactions*: non-bonded interactions between atoms separated by 3 bonds and which participate in a dihedral interaction are scaled by a factor which depends on the force field. The AMBER force field for proteins, for examples, scales 1-4 electrostatic interactions by a factor 1/1.2 and van der Waals interactions by 1/2. As for the OPLS force field, the same scaling factor 1/2 is applied in the AA version while in the UA version the scaling factor for van der Waals interactions is 1/8. The major component of biological systems is water. Different models of water have been developed with different level of accuracy and hence complexity. The most used water model are SPC [88], SPC/E [89], TIP3P [90] and TIP4P [91]. Each force field comes with a water model, that is the interactions have been parameterised using a specific model of water. However, most times force field parameters are compatible with the most popular models of water.
Many biological phenomena occur on scales much longer than a few nanoseconds. Thus, even if computer power has significantly grown, microseconds simulations involving a large number of atoms cannot be performed using atomistic force fields.

2.4.3 Coarse grained force fields

To extend simulation time and length scales one possible solution is to *coarse grain* the system, that is average out some degrees of freedom of the system leaving only those relevant to the problem. There are many levels of coarse graining which are dependent on the phenomena under study. The general idea below coarse graining is no longer to consider atoms as the building blocks of the system, but groups of atoms represented by single particles or *beads* that should represent the physico-chemical properties of the underlying atoms. The size of the group of atoms that is coarsened into a single bead sets the level of coarse graining. Together with reducing the number of particles in the system, the higher efficiency of coarse grained force fields comes with the slowing down of vibrational modes in the system, which permits the use of larger time steps, and with the smoothing of the FES, that is a reduced number of free energy minima is present and the height of the free energy barriers which are still present is lowered, which leads to a faster diffusion of the system.
As remarked in the previous subsection, the largest number of molecules in biological simulations is represented by water molecules. One possible way to further extend simulation time and length scales maintaining a bead-like description is to implicitly include water molecules adjusting the interaction parameters of the remaining beads. For example, the self assembly of lipids into a lipid bilayer is strongly dependent on the presence of water. If water is explicitly removed from the simulation, one possible way to retrieve the behaviour of lipids is to add an attractive interaction between the lipids so as to make them self assemble as if there were water. In this thesis, however, we explicitly include water in our simulations.
Coarse grained force fields are typically parameterised so as to reproduce mechanical and thermodynamic target properties derived from atomistic simulations. For instance, the force field used in this thesis, the Martini force

field [92], aims at reproducing the partition free energy of a set of molecules between an organic solvent and water. In the following we enter in details in the force field since a large part of the simulations in this thesis are performed with this force field.

Martini force field The Martini force field was first developed for organic solvents and lipids [92] and then extended to proteins [93, 94, 95], sugars [96], polymers [97, 99, 98] and nucleic acids [100, 101]. The first step in building a coarse grained force field is to chose an appropriate *mapping*; the Martini force field is based on a 4:1 mapping in which four heavy atoms in the atomistic molecule are coarsened into one bead in the coarse grained model. Special beads are used whenever only two or three atoms are included in the mapping. An example of the coarse graining procedure is shown in figure 13.

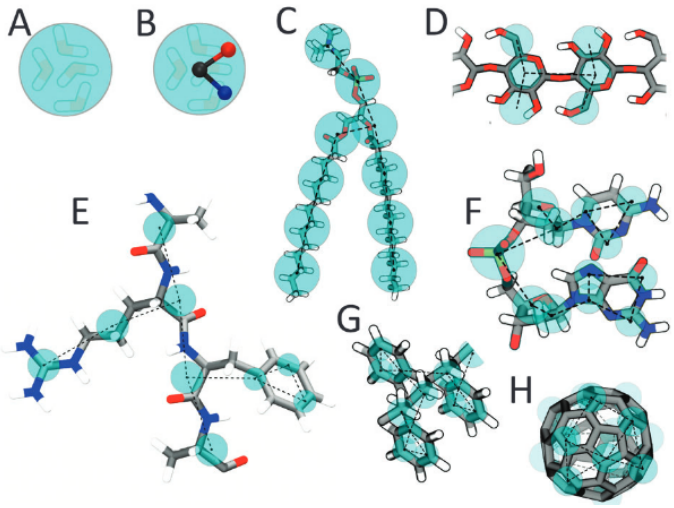

Figure 13: Example of the mapping procedure in the Martini force field (cyan circles). A: standard water. B: polarisable water. C: phospholipid. D: polysaccaride fragment. E: peptide. F: DNA fragment. G: polystyrene fragment. H: fullerene. Taken from [102].

A small number of different beads is parameterised to represent four kinds of particles: polar, charged, non-polar and apolar. Each of these four categories includes a set of subcategories labelled either by a number, indicating the bead polarity, or by a letter, related to the hydrogen-bonding capability of the bead. To parameterise the force field, the free energy of hydration and vaporisation and the partitioning free energy between water and different organic solvents for each bead type have been used as target properties. Each of the aforementioned values has been obtained from the equilibrium densities of the coarse-grained particles in the diverse phases. A table with the coarse-grained model results compared with the corresponding experimental values is shown in figure 14.

		Q				P					N				C				
	sub	da	d	a	0	5	4	3	2	1	da	d	a	0	5	4	3	2	1
Q	da	O	O	O	II	O	O	O	I	I	I	I	I	IV	V	VI	VII	IX	IX
	d	O	I	O	II	O	O	O	I	I	I	III	I	IV	V	VI	VII	IX	IX
	a	O	O	I	II	O	O	O	I	I	I	I	III	IV	V	VI	VII	IX	IX
	0	II	II	II	IV	I	O	I	II	III	III	III	III	IV	V	VI	VII	IX	IX
P	5	O	O	O	I	O	O	O	O	O	I	I	I	IV	V	VI	VI	VII	VIII
	4	O	O	O	O	O	I	I	II	II	III	III	III	IV	V	VI	VI	VII	VIII
	3	O	O	O	I	O	I	I	II	II	II	II	II	IV	IV	V	V	VI	VII
	2	I	I	I	II	O	II	II	II	II	II	II	II	III	IV	IV	V	VI	VII
	1	I	I	I	III	O	II	II	II	II	II	II	II	III	IV	IV	IV	V	VI
N	da	I	I	I	III	I	III	II	II	II	II	II	II	IV	IV	V	VI	VI	VI
	d	I	III	I	III	I	III	II	II	II	II	III	II	IV	IV	V	VI	VI	VI
	a	I	I	III	III	I	III	II	II	II	II	II	III	IV	IV	V	VI	VI	VI
	0	IV	IV	IV	IV	IV	IV	IV	III	III	IV	IV	IV	IV	IV	IV	IV	V	VI
C	5	V	V	V	V	V	V	IV	IV	IV	IV	IV	IV	IV	IV	IV	IV	V	V
	4	VI	VI	VI	VI	VI	VI	V	IV	IV	V	V	V	IV	IV	IV	IV	V	V
	3	VII	VII	VII	VII	VI	VI	V	V	IV	VI	VI	VI	IV	IV	IV	IV	IV	IV
	2	IX	IX	IX	IX	VII	VII	VI	VI	V	VI	VI	VI	V	V	V	IV	IV	IV
	1	IX	IX	IX	IX	VIII	VIII	VII	VII	VI	VI	VI	VI	VI	V	V	IV	IV	IV

Figure 15: Interaction table for the Martini beads. The intensity of the interaction decreases from level O to level IX. Taken from [92].

			ΔG^{vap}		ΔG^{hyd}		ΔG^{part}_{HW}		ΔG^{part}_{CW}		ΔG^{part}_{EW}		ΔG^{part}_{OW}	
type	building block	examples	exp	CG	exp	CG	exp	CG	exp	CG	exp	CG	exp	CG
Q_{da}	H_3N^+—C_2—OH	ethanolamine (protonated)				−25		< −30		−18		−13		−18
Q_d	H_3N^+—C_3	1-propylamine (protonated)				−25		< −30		−18		−13		−18
	NA^+OH	sodium (hydrated)				−25		< −30		−18		−13		−18
Q_a	PO_4^-	phosphate				−25		< −30		−18		−13		−18
	CL^-HO	chloride (hydrated)				−25		< −30		−18		−13		−18
Q_0	C_5N^+	choline				−25		< −30		−18		−13		−18
P_5	H_2N—C_2=O	acetamide	sol	sol	−40	−25	−27	−28	(−20)	−18	−15	−13	−8	−10
P_4	HOH (× 4)	water	−27	−18	−27	−18	−25	−23		−14	−10	−7	−8	−9
	HO—C_2—OH	ethanediol	−35	−18	−33	−18	−21	−23		−14		−7	−8	−9
P_3	HO—C_2=O	acetic acid	−31	−18	−29	−18	−19	−21	−9	−10	−2	−6	−1	−7
	C—NH—C=O	methylformamide	−35	−18		−18		−21		−10		−6	−5	−7
P_2	C_2—OH	ethanol	−22	−16	−21	−14	−13	−17	−5	−2	−3	1	−2	−2
P_1	C_3—OH	1-propanol	−23	−16	−21	−14	−9	−11	−2	−2	0	1	1	−1
		2-propanol	−22	−16	−20	−14	−10	−11	−2	−2	−1	1	0	−1
N_{da}	C_4—OH	1-butanol	−25	−16	−20	−9	−5	−7	2	0	4	2	4	3
N_d	H_2N—C_3	1-propylamine	−17	−13	−18	−9	(−6)	−7	(1)	0	(−3)	2	(3)	3
N_a	C_3=O	2-propanone	−17	−13	−16	−9	−6	−7	1	0	−1	2	−1	3
	C—NO_2	nitromethane	−23	−13	−17	−9	−6	−7		0		2	−2	3
	C_3=N	proprionitrile	−22	−13	−17	−9	−5	−7		0		2	1	3
	C—O—C=O	methylformate	−16	−13	−12	−9	(−6)	−7	(4)	0	(−1)	2	(0)	3
	C_2HC=O	propanal		−13	−15	−9	−4	−7		0	2	2	3	3
N_0	C—O—C_2	methoxyethane	−13	−10	(−8)	−2	(1)	−2		6	(3)	6	(3)	5
C_5	C_3—SH	1-propanethiol	−17	−10		1		5		10		10		6
	C—S—C_2	methyl ethyl sulfide	−17	−10	−6	1	(7)	5		10		10	(9)	6
C_4	C_2=C_2	2-butyne	−15	−10	−1	5		9		13		13	9	9
	C=C—C=C	1,3-butadiene		−10	2	5	11	9		13		13	11	9
	C—X_4	chloroform	−18	−10	−4	5	(7)	9	14	13		13	11	9
C_3	C_2=C_2	2-butene		−10		5		13		13		13	13	14
	C_3—X	1-chloropropane	−16	−10	−1	5	12	13		13		13	12	14
		2-bromopropane	−16	−10	−2	5		13		13		13	12	14
C_2	C_3	propane	gas	−10	8	10		16		15		14	14	16
C_1	C_4	butane	−11[b]	−10	9	14	18	18		18		14	16	17
		isopropane	gas	−10	10	14		18		18		14	16	17

Figure 14: Table of the experimental and simulated values of hydration, vaporisation and partitioning free energies. Examples of the chemical compounds represented by each Martini bead are also reported. Taken from [92].

Contrary to atomistic force fields, in the Martini force field van der Waals interactions are defined for each pair of beads. The standard value for σ is 0.47 nm; a smaller value (σ = 0.43 nm) is assigned to small beads, which experience also reduced interaction strength, while σ = 0.62 nm is set between charged beads and very apolar beads (lowest polarity levels, 1 and 2). There are ten interaction levels, from 5.6 kJ mol^{-1} (level O) to 2.0 kJ mol^{-1} (level IX). The interaction strength is scaled to 75% for small beads and level IX is assigned only when σ = 0.62 nm. The interaction matrix is shown in figure 15. As for electrostatic interactions, integer charges are assigned to charged bead types. Because only one charge, placed at the position of the bead, is used to model the charge of the underlying group of atoms for that bead, polarisability effects due to atomic dipoles are hindered. To account for the screening of polar media, an effective dielectric constant of 15 is used to

scale electrostatic interactions. Both van der Waals and electrostatic interactions are cut-offed and shifted.
Bonded interactions depend on the molecule to be parameterised. For example, aliphatic chains are described by bond length l_0 = 0.47 nm, bond constant k_l = 1250 kJ mol^{-1} nm^{-2}, equilibrium angle θ_0 = 180° and angle constant k_a = 25 kJ mol^{-1}. Due to the washing out of fast vibrations, time steps up to 40 fs can be used in simulations with the Martini force field.
In standard Martini, water is modelled as a unique neutral bead which represents four water molecules. With this parameterisation the intrinsic polar character of water is suppressed. To partially solve the problem of electrostatic screening, a **polarisable** model of water (PW) has been introduced [103] and refined [104]. This new water model maps four water molecules into three Martini beads: one central bead (W), which interacts only *via* van der Waals interactions, and two side beads, WM, carrying a negative charge, and WP, carrying a positive charge as shown in figure 16. No van der

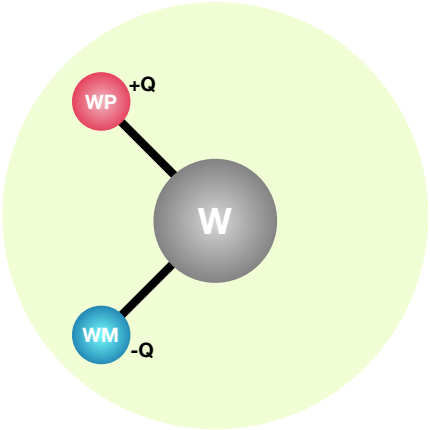

Figure 16: Schematic representation of a polarisable water bead. The van der Waals radius of the W bead is shown as a shaded green circle. Adapted from [103].

Waals interactions are assigned to the charged beads. The size of a PW bead is the same as that of a standard water bead. WP and WM are bound to W with a fixed-length bond while a harmonic potential is used for the angle. Orientational polarisability can somehow be retrieved with the PW model so that the global dielectric constant can be reduced to 2.5 in order to obtain a more realistic behaviour when two charged species interact in hydrophobic regions. Both cut-off and PME method to treat electrostatics can be used. Due to the new parameterisation of water, all interactions involving charged Martini types have been reassigned. The new interaction table is shown in figure 17.

	POL	Q_{da}	Q_d	Q_a	Q_0	P_5	P_4	P_3	P_2	P_1	N_{da}	N_d	N_a	N_0	C_5	C_4	C_3	C_2	C_1
Q_{da}	O	O	I	I	IV	O	O	O	O	O	O	O	O	III	IV	V	VI	VII	VII
	O	O	O	O	II	O	O	O	I	I	I	I	I	IV	V	VI	VII	IX	IX
Q_d	I	I	IV	III	VII	O	O	O	O	O	O	II	O	III	IV	V	VI	VII	VII
	O	O	I	O	II	O	O	O	I	I	I	III	I	IV	V	VI	VII	IX	IX
Q_a	I	I	III	IV	VII	O	O	O	O	O	O	O	II	III	IV	V	VI	VII	VII
	O	O	O	I	II	O	O	O	I	I	I	I	III	IV	V	VI	VII	IX	IX
Q_0	II	IV	VII	VII	IV	O	O	O	I	II	II	II	II	III	IV	V	VI	VII	VII
	O	II	II	II	IV	I	O	I	II	III	III	III	III	IV	V	VI	VII	IX	IX

Figure 17: Interaction table for the Martini beads in the polarisable model. Taken from [103].

As the number of particles is tripled, the better accuracy that can be obtained with a polarisable model has to face a degradation of simulation performance.

2.4.4 Molecular dynamics software

Usually force field parameters are included in MD softwares. For this thesis we use the GROMACS package [105] which provides different integrators, barostats and thermostats, to run simulations at constant temperature and pressure, different methods to compute electrostatic interactions and a set of analysis tools. Moreover it is compatible with both atomistic and coarse grained force fields, the most used of the former kind being included in the package.
To speed up simulations, the MD code included in the GROMACS package is parallelised, that is the algorithms necessary to run an MD simulation can be run on more than one core per CPU or more than one CPU. For MD simulations, the simulation box is divided into cells, each of which contains a certain number of particles and is assigned to a core. Communication within different cores is needed to compute interactions; this task is performed by special libraries and is the most expensive part of parallelisation. A balance between the speed-up due to parallel execution of the code and the slowing down of communication within different cores should be found to optimise performances. In the case of the GROMACS package this limit is set to about 200 particles/core. When the PME method to compute electrostatics is used, the positions of all particles, and not only those of particles in neighbouring cells, is needed. To avoid extensive communication within cores, the GROMACS package allows to separate the computation of electrostatics with PME from all other calculations. It is possible to increase the performance of MD simulations also using GPUs to which the computation of non-bonded interaction is assigned. Recent versions of the GROMACS package support this technology.
To run metadynamics simulations we use a plugin compatible with the GROMACS package named PLUMED [106]. An input file containing metadynamics parameters, that is Gaussian width, height and deposition pace together with the set of collective variables, has to be provided to the software. Analysis tools for metadynamics simulations, such as that to reconstruct the FES of the system, are included in the plugin.

3 COMPUTATIONAL MODELS OF NANOPARTICLES

Contents

In this chapter we describe the computational models of the AuNPs we use to study the NP–membrane and NP–protein interactions. The NPs are composed of a gold core which is functionalised by thiolated ligands. We consider both an atomistic and a coarse-grained model of the ligands while the gold core is always described by an atomistic representation. For the coarse-grained models developed for the scopes of this thesis, validation is based on the comparison with atomistic structural properties.

3.1 Nanoparticle core model

Thiolated AuNPs are widely used in different biomedical applications because of their electrochemical and thermal stability [107]. Since the publication of the first paper on thiolated AuNPs synthesis in 1994 [108], several progress have been made in the synthesis of AuNPs in the 1-3 nm range. These NPs have been characterised at a molecular level and present *magical* numbers of Au and S atoms among which are, for example, $Au_{20}(SR)_{16}$, $Au_{25}(SR)_{18}$, $Au_{38}(SR)_{24}$, and the $Au_{144}(SR)_{60}$ which is the one we use in this thesis. Among the large variety of clusters which can be synthesised in the sub-5 nm range, the NP with mass 29 kDa has attracted great interest and has been extensively characterised. It was shown with ab initio computational techniques that this NP corresponds to the $Au_{144}(SR)_{60}$ cluster [109]. This NP has a gold core with chiral icosahedral symmetry made of three concentric shells and a surface layer of 30 Au atoms to which 60 sulphur atoms are bound in a staple configuration. The atomic structure of the cluster is shown in figure 18. The diameter of the NP core is about 2 nm while the size of the functionalised NP depends on the length of the ligands.

3.1.1 Gold core model

This thesis is part of large project aiming at investigating the interaction of NPs with model lipid membranes and proteins (ERC Starting Grant BioMNP, g.a. 677513). A part of the project is related to the study of the interaction between heated NPs and model membrane. To reproduce the heating of the NP, which results from laser irradiation, the vibrational spectrum of the cluster should be

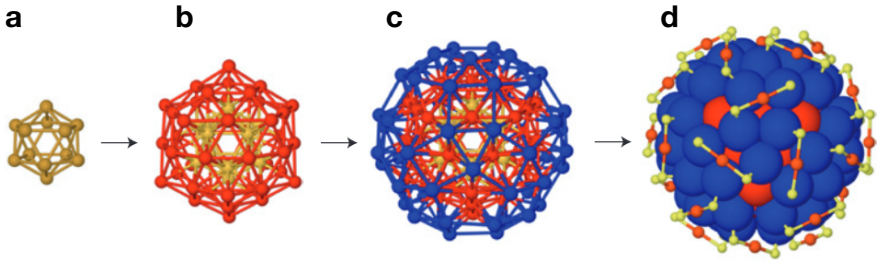

Figure 18: a-c: concentric shells of Au atoms which constitute the core of the $Au_{144}(SR)_{60}$ NP. d: staple configuration of the 30 Au surface atoms and 60 sulphur atoms to which ligands are bound in functionalised NPs. Adapted from [107].

reproduced as faithfully as possible. Given this target we decided to describe the gold core atomistically and to allow atomic vibrations in the cluster. One of the major concerns with the development of a model for the gold cluster is that gold is a metal and as such cannot be described by pair potentials, conversely to organic molecules. In metals, in fact, many-body effects become relevant to describe experimental properties such as the cohesive energy or the melting temperature. In particular, the so-called *bond length-bond order correlation*, which reflects the dependence of the bond length on the coordination of the atoms involved in the bond, cannot be captured by pair potentials. Different potential functions have been used to describe the many-body character of the metallic bond, among which there are the embedded atom [110], the Sutton-Chen [111] and the Gupta potential [112], which is the one we used to describe the vibrational spectrum of the Au_{144} cluster.

Gupta potential The potential function developed by Gupta to describe bonds in metals is based on the second-moment tight binding approximation of the electron density of states. The energy of a cluster of N metal atoms can be written as a sum of a binding contribution E_B, which is responsible for the many-body character of the potential, and a repulsive term E_R, which has a pairwise character and is necessary to guarantee cluster stability. The total cohesive energy of the cluster, E_C, reads

$$E_C = E_R + E_B = \sum_{i=1}^{N}(E_{Ri} + E_{Bi}) = \\ = \sum_{i=1}^{N}\left(\sum_{j=1}^{n} A e^{-p(r_{ij}/r_0-1)} - \sqrt{\sum_{j=1}^{n}\xi^2 e^{-2q(r_{ij}/r_0-1)}}\right) \tag{3.1.1}$$

Here r_{ij} is the distance between atoms i and j and r_0 is their first neighbour distance in bulk metal. The sum on the neighbours (j) is usually cut-offed at a number n of atoms which lie within a distance r_c from atom i. A, p, ξ and q are fitting parameters which are assigned so as to reproduce key experimental properties such as cohesive energies. A set of parameters for many transition metals have been derived by Cleri and Rosato [113].

Elastic network Given the potential function in equation 3.1.1, the vibrational modes of a cluster of atoms can be derived diagonalising the Hessian matrix associated to the potential. We used the vibrational spectrum

calculated from the Hessian as a target to parameterise our model of gold core.
The simplest choice that can be made to reproduce vibrations is to consider and elastic network among gold atoms which is described by the potential function

$$U_{el} = \sum_i \sum_{j \neq i} \frac{1}{2} k_{ij} (r_{ij} - r_{ij}^0)^2 \tag{3.1.2}$$

where r_{ij}^0 is the equilibrium distance between atoms i and j as computed in [109] and k_{ij} is the elastic constant associated to the bond between atoms i and j. The sum over j considers only atoms within a cut-off distance of 0.35 nm from atom i.
We tested different possibilities for k_{ij} comparing the results for the vibrational spectra computed from the potential in equation 3.1.2 and the Gupta potential. We found that a unique bond constant was not sufficient to faithfully reproduce the vibrations of the cluster. Thus we introduced two bond constants which distinguish between surface and core gold atoms. We applied a cut-off criterion on the number of neighbours to assign the elastic constants: if an atom had at least 9 neighbours it was considered as a bulk atom, otherwise as a surface atom. A larger bond constant was assigned to bonds between surface atoms while a smaller one to bonds between surface-bulk and bulk-bulk atoms. A surface bond constant $k_{ij}^S = 32500\,\mathrm{kJ\,mol^{-1}\,nm^{-2}}$ and a bulk bond constant $k_{ij}^C = 11000\,\mathrm{kJ\,mol^{-1}\,nm^{-2}}$ proved to be the best choice to reproduce the vibrational spectrum of the gold Au_{144} cluster with an elastic network potential. The superimposition of the target Gupta vibrational spectrum and the vibrational spectrum obtained with the elastic network potential is shown in figure 19.

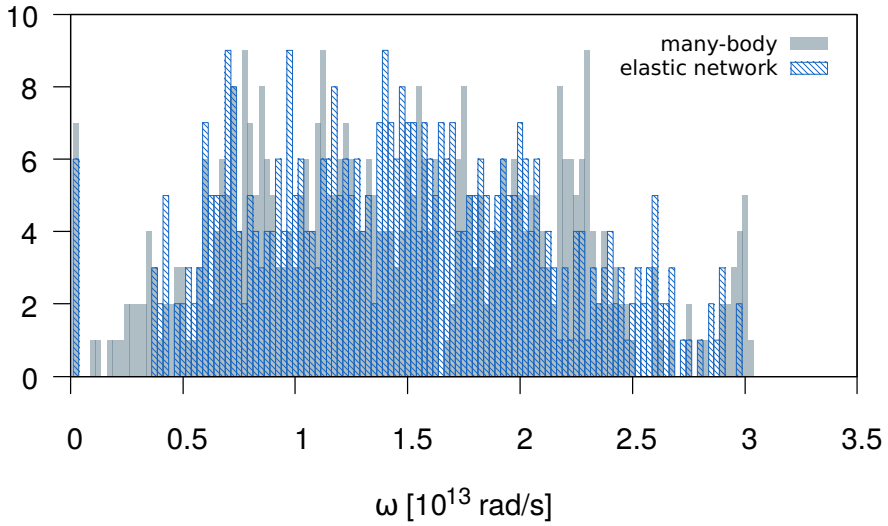

Figure 19: Vibrational spectrum of the Au_{144} cluster as computed with the Gupta potential (solid grey) and with the elastic network model (blue pattern). The target many-body vibrational spectrum is well reproduced, for high frequency modes, by a combination of two elastic constants: $k_S = 32500$ kJ mol^{-1} nm^{-2} and $k_C = 11000$ kJ mol^{-1} nm^{-2}.

3.1.2 Sulphur atom shell

Gold clusters are usually functionalised with thiolated molecules. Thiols are organosulphur compounds which bind to Au surfaces thanks to a strong Au–S bond. For the Au_{144} cluster, 60 thiolated molecules can be bound to the Au surface. We anchored the 60 sulphur atoms to the 30 Au surface atoms with the same bond constant as surface gold atoms, that is $k_S = 32500$ kJ mol^{-1} nm^{-2}. To keep the sulphur atoms in their equilibrium positions, as derived in [109], we built an elastic network among the sulphur atoms using a bond constant of 1250 kJ mol^{-1} nm^{-2} in coarse-grained simulations and of 25000 kJ mol^{-1} nm^{-2} in atomistic simulations. A cut-off distance of 0.55 nm was used to search for neighbour atoms. To prevent sulphur atoms penetrate the gold cluster, a purely repulsive potential has been set between sulphur and gold atoms. Using the Lennard-Jones potential form in equation 2.4.2, the repulsive potential is obtained setting $C_6 = 0$ and $C_{12} = 0.92953 \cdot 10^{-6}$ kJ mol^{-1} nm^{12}. Both the gold and sulphur elastic networks are shown in figure 20.

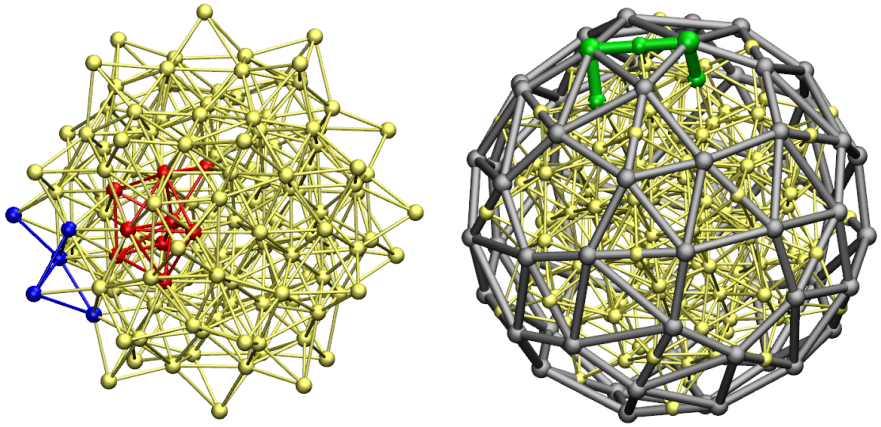

Figure 20: Elastic networks for gold (yellow) and sulphur (grey) atoms. Left: the gold elastic network. A core atom and its neighbours are represented in red, while a surface atom and its neighbours are shown in blue. Right: sulphur elastic network. A typical staple structure of the form Au-S-Au-S-Au is shown in green.

At atomistic level, gold and sulphur atoms possess partial charges, which we obtained from with courtesy of J. Akola in private communication. In particular gold atoms in the core have a positive charge +0.0286*e* while surface gold atoms, that is the central gold atom in the staple structure shown in green in figure 20, have a positive charge of +0.10273*e*, *e* being the absolute value of the electron charge. Sulphur atoms are instead negatively charged with a charge per atom of -0.12123*e*. The cluster thus has a negative total charge of -0.9315*e* which is compensated by an opposite charge equally distributed among the first atomic group of each ligand used to functionalise the gold cluster. In coarse grained simulations no charge is attributed to any gold or sulphur atom in the cluster.

3.2 Ligand model

We used three kinds of ligands to functionalise the $Au_{144}(SR)_{60}$ cluster: hydrophobic, charged and zwitterionic. Hydrophobic and charged ligands

have been modelled at both atomistic and coarse-grained level, while for zwitterionic ligands only a coarse-grained model have been developed. In the following subsections the details on the ligands and their models will be given.

3.2.1 Atomistic model of ligands

We chose to build a model for two of the most commonly used ligands in experiments with functionalised NPs: octanethiol (OT) ligands were chosen as hydrophobic ligands while mercapto-undecane carboxylate (AN) as a model for anionic ligands. The parameterisation of the ligands has been made within the united atom version of the OPLS force field. The schematic structure of the ligands is shown in figure 21 while the interaction parameters for the non-bonded and bonded interactions are summarised in table 1 and 2, respectively. Bonded interactions have been assigned according to the models of similar compounds in [84, 114, 115]. Type C2 and C3 in figure 21 refer to the CH_2 and CH_3 chemical groups, respectively. C and O types in figure 21 represent the COO^- terminal group of the anionic ligand. Non-bonded interactions are assigned based on OPLS types, except for Au whose parameters are derived from [116].

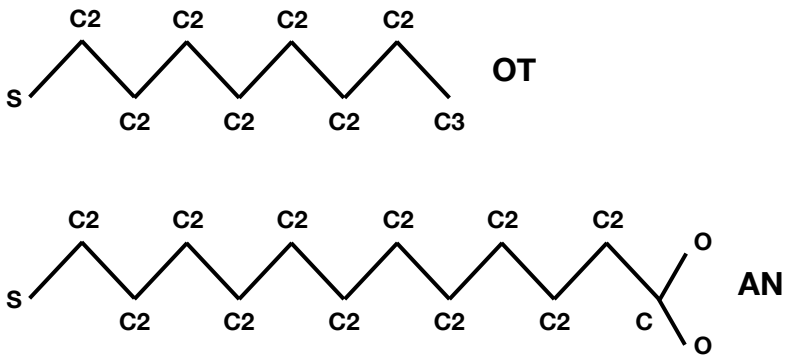

Figure 21: Schematic representation of the hydrophobic (top) and anionic (bottom) ligands.

Table 1: Parameters for non-bonded interactions of the particles in the hydrophobic and anionic ligands. σ is in nm and ϵ in kJ mol^{-1}. [a] the C2 particle bound to the C particle in the anionic ligand has a charge of -0.1e to obtain a net -1.0e charge for the COO^- terminal group. The C2 particle bound to the sulphur atom S has a charge of +0.0155225e to compensate for the core charge (see section 3.1). Charges are in units of e, the absolute value of the electron charge.

Atoms	σ	ϵ	charge
Au	0.2629	22.1449	see section 3.1
S	0.355	1.046	see section 3.1
C2	0.3905	0.493712	0[a]
C3	0.3905	0.7322	0
C	0.3750	0.43932	+0.7e
O	0.296	0.87864	-0.8e

Table 2: Parameters for bonded interactions in the hydrophobic and anionic ligands.

(a) Bonds. Bond length l_0 in nm, bond constant k_b in kJ mol^{-1} nm^{-2}.

Atoms	l_0	k_b (x10^5)
S – C2	0.182	1.85858
C2 – C2	0.153	2.17672
C2 – C3	0.153	2.17672
C2 – C	0.152	2.65390
C – O	0.125	5.48941

(b) Angles. Equilibrium angle θ_0 in deg, angle constant k_a in kJ mol^{-1} rad^{-2}.

Atoms	θ_0	k_a
S – C2 – C2	114.4	519.7
C2 – C2 – C2	112.0	527.4
C2 – C2 – C3	112.0	527.4
C2 – C2 – C	112.0	527.4
C2 – C – O	117.0	586.0
O – C – O	126.0	669.8

(c) Dihedral angles. The parameters for the Ryckaert-Bellemans form of dihedral angles are reported for the X – C2 – C2 – X dihedral angle, while the periodic form is used for both the X – C2 – C – X and X – O – C – O dihedral angles, X being any atom type. Ryckaert-Bellemans coefficients are in kJ mol^{-1}. In the periodic form the dihedral angle ϕ is in deg and the dihedral constant in kJ mol^{-1}.

Atoms	C_0	C_1	C_2	C_3	C_4	C_5
X – C2 – C2 – X	8.4015	16.7945	1.134	-26.33	0	0
Atoms	ϕ	k_ϕ	multiplicity			
X – C2 – C – X	180.0	0	3			
Improper dihedral angle						
Atoms	ϕ	k_ϕ	multiplicity			
X – O – C – O	180.0	0	3			

Model validation To validate our model for the ligands we built a NP covered by 60 anionic ligands (see figure 22) and performed a simulation in water to compute the radial distribution function (RDF) for the various components of the system. We compared the results with the RDFs obtained by Heikkilä *et al.* [117] for the same system and force field. We used a simulation box of about 12x12x12 nm^3 and solvated the anionic NP with about 54000 water molecules; 60 counterions (Na^+) were added to neutralise the simulation box. The system was equilibrated for 100 ns and the last 80 ns were used to compute RDFs with respect to the centre of mass (COM) of the NP for each component of the system. The NP core (Au + S atoms) was considered as a whole while ligands were divided into a hydrophobic part, made of the C2 particles, and a charged part which includes the atoms of the negatively charged COO^- terminal groups. The distributions of water and ions were computed separately. As it can be seen from figure 22 the radius of the NP core is about 1 nm as derived from ab initio calculations in [109]. The ligand shell has a thickness of about 2 nm so that the functionalised NP is about 5.4 nm. The small peak at the position of the surface of the cluster in the water distribution obtained from our simulations is due to a couple of water molecules which were trapped on the cluster surface.

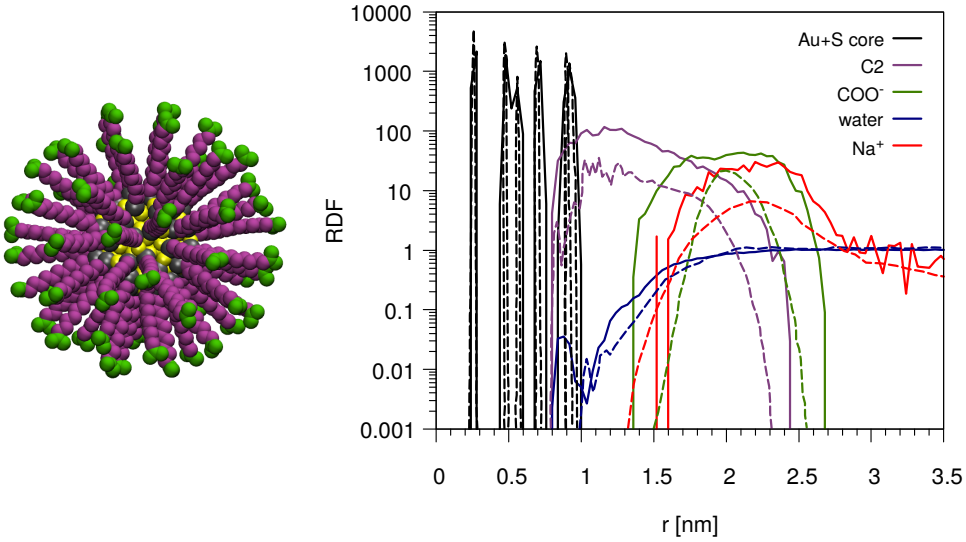

Figure 22: Left: anionic gold nanoparticle. Gold atoms in yellow, sulphur atoms in grey, C2 particles representing CH_2 groups in purple and negatively charged COO^- terminal group in green. Right: radial distribution functions for the different components of the system with respect to the centre of mass of the gold cluster. Solid lines refer to the model we developed while dashed lines are data extrapolated from [117].

3.2.2 Martini model of ligands

We developed a coarse-grained model for anionic, cationic, hydrophobic and zwitterionic ligands according to the Martini model.

Anionic, cationic and hydrophobic ligands As in the atomistic case we developed a coarse-grained model for the OT and AN ligands and we chose to model the trimetil-ammonium terminated mercapto-undecanoic acid (CAT) as cationic ligand. The mapping from the atomistic to the coarse-grained model is shown in figure 23. According to the Martini scheme, 4 CH_2 groups were coarsened into a Martini bead of type C1 (see figure 14). As for the charged ligands, a Martini bead of type Q_{da} with charge -1 was used to model the COO^- anionic terminal group while a bead type Q_0 with charge +1 was used for the cationic $N(CH_3)_3^+$ terminal group (see figure 14). Bonded interactions were assigned following the model of the lipid tails; the parameters are summarised in table 3. Contrary to the atomistic case, non-bonded interactions should be defined for each couple of beads in the system. For C1, Q_{da} and Q_0 beads the interaction matrix is defined by the kind of Martini force field (standard or polarisable) which is used. Gold and sulphur atoms are not Martini types so we defined their interaction matrix with all other Martini particles assigning a purely repulsive potential with the same strength of the Au-S potential defined in subsection 3.1.2. This choice was made to prevent any Martini particle from penetrating the NP core.

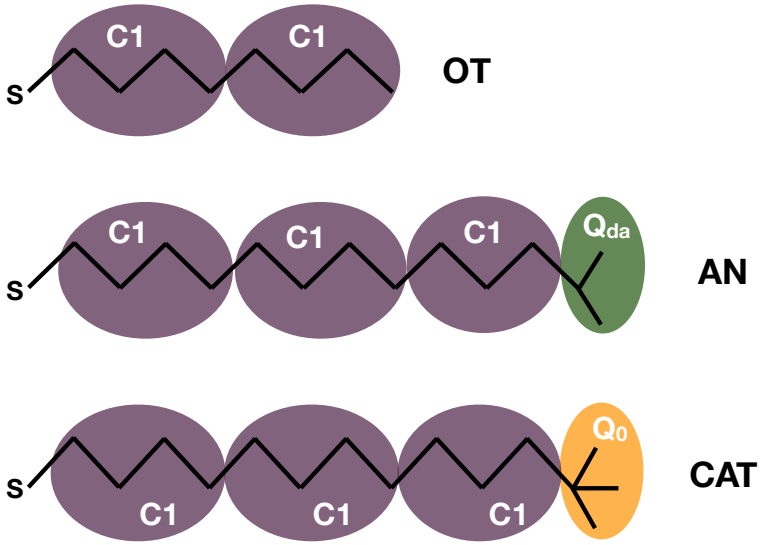

Figure 23: Mapping for the hydrophobic (OT, top), anionic (AN, centre) and cationic (CAT, bottom) ligands. Purple, green and yellow beads represent the hydrophobic moieties (C1), the anionic (Q_{da}) and cationic (Q_0) terminal groups, respectively.

Table 3: Parameters for bonded interactions of the beads of the hydrophobic, anionic and cationic ligands.

(a) Bonds. Bond length l_0 in nm, bond constant k_b in kJ mol^{-1} nm^{-2}.

Atoms	l_0	k_b
S – C1	0.47	1250
C1 – C1	0.47	1250
C1 – Q_{da}	0.47	1250
C1 – Q_0	0.47	1250

(b) Angles. Equilibrium angle θ_0 in deg, angle constant k_a in kJ mol^{-1} rad^{-2}.

Atoms	θ_0	k_a
S – C1 – C1	180	25
C1 – C1 – C1	180	25
C1 – C1 – Q_{da}	180	25
C1 – C1 – Q_0	180	25

As in the atomistic case, we built a completely anionic NP and performed a simulation in water to compute the RDFs of the different components of the system as a function of the distance from the COM of the gold core. The NP was inserted in a box of volume about 11x11x11 nm^3 and solvated with about 10000 water beads. To neutralise the simulation box, 60 Na^+ counterions were added in the water phase. The system was equilibrated for about 30 ns and the RDFs were computed from the trajectory of 1 μs run. The system was divided into the NP core, the hydrophobic parts of the ligands, C1 Martini type, the negatively charged Q_{da} beads, water and ions. The RDFs are shown in figure 24. The functionalised NP has a diameter of about 5.8 nm, the ligand shell being about 2 nm thick.

Zwitterionic ligands To study the NP-protein interaction we developed a model for two zwitterionic ligands whose synthesis and anti-fouling properties have been described in [46]. The two ligands have a common stretch formed by a hydrophobic part and a 4-monomer PEG part, and a zwitterionic sulphobetaine terminal group whose hydrophobicity can be tuned: the less

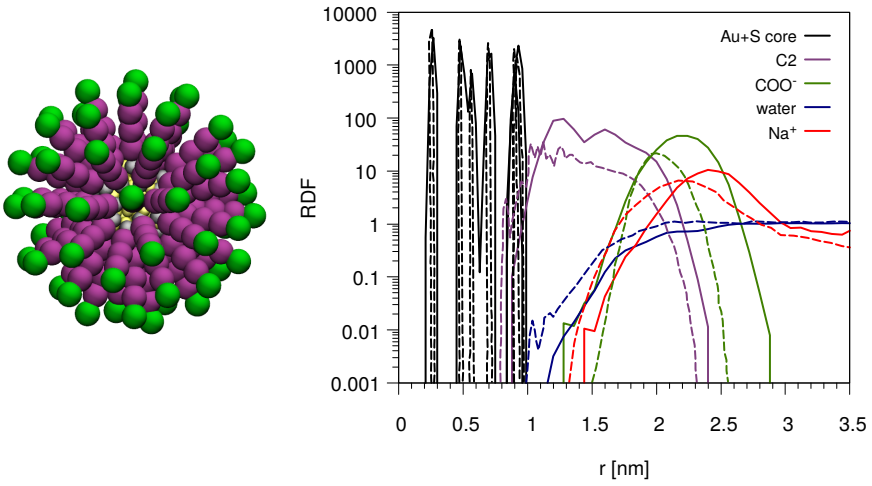

Figure 24: Left: anionic gold nanoparticle. Gold atoms in yellow, sulphur atoms in grey, C1 beads representing CH_2 groups in purple and negatively charged Q_{da} beads representing the COO^- terminal groups in green. Right: radial distribution functions for the different components of the system with respect to the centre of mass of the gold cluster. Solid lines refers to the model we developed while dashed lines are data extrapolated from [117].

hydrophobic ligand (Z) has a sulphobetaine terminal group while the more hydrophobic (ZH) has a di-butane modified sulphobetaine terminal group. A schematic representation of the ligands and their mapping is shown in figure 25. The parameters for the bonded interactions are summarised in table 4. The PEO bead is not a standard Martini type; its bonded and non-bonded parameters were taken from [118, 119] and [120]. In particular, the Lennard-Jones parameters for the self-interaction of PEO beads and those for the PEO–water interaction were taken from the PEG model by Lee and Pastor [118]; bonded interaction in the their model were corrected according to [120] so that a combination of cosine harmonic (CH) and restricted bending (ReB) potentials has been used to model the angle potential involving PEO beads. The bonds between C1 and PEO beads has been parameterised according to the polyoxyethylene alkyl ether model by Rossi *et al.* [119].

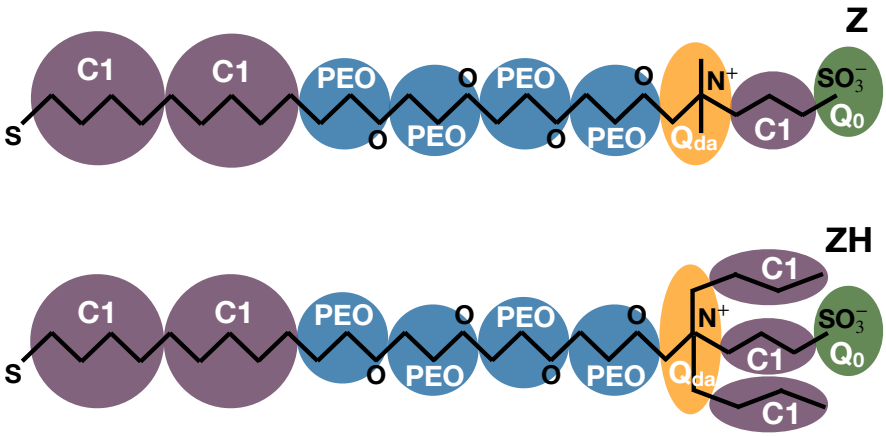

Figure 25: Mapping for the zwitterionic ligands. Purple beads represent the hydrophobic moieties (C1), cyan beads the PEG monomers (PEO), yellow and green beads the positively (Q_0) and negatively (Q_{da}) charged groups, respectively.

Table 4: Parameters for bonded interactions in the zwitterionic ligands.

(a) Bonds. Bond length l_0 in nm, bond constant k_b in kJ mol^{-1} nm^{-2}. [a] bond between the two C1 beads which constitute the side chains of the Q_0 bead and the Q_0 bead itself.

Atoms	l_0	k_b
S – C1	0.47	1250
C1 – C1	0.47	1250
C1 – PEO	0.41	5000
PEO – PEO	0.33	17000
PEO – Q_0	0.47	1250
Q_0 – C1	0.40	1250
Q_0 – C1[a]	0.47	1250
C1 – Q_{da}	0.40	1250

(b) Angles. Equilibrium angle θ_0 in deg, angle constant k_a in kJ mol^{-1} rad^{-2}. [a] cosine harmonic (CH) function for angles. [b] restricted bending (ReB) angle function. [c] angle involving the C1 bead in the side chain of the Q_0 bead.

Atoms	θ_0	k_a
S – C1 – C1	180	25
C1 – C1 – PEO	180	25
C1 – PEO – PEO	180	25
PEO – PEO – PEO[a]	130	50
PEO – PEO – PEO[b]	130	25
PEO – PEO – Q_0	180	25
PEO – Q_0 – C1	180	25
PEO – Q_0 – C1[c]	90	25
C1 – Q_0 – C1	180	25
Q_0 – C1 – Q_{da}	180	25

(c) Dihedral angles. Parameters for the periodic form of the dihedral angle: ϕ is in deg and k_ϕ in kJ mol^{-1}.

Atoms	ϕ	k_ϕ	multiplicity
PEO – PEO – PEO – PEO	180.0	1.960	1
PEO – PEO – PEO – PEO	0	0.180	2
PEO – PEO – PEO – PEO	0	0.330	3
PEO – PEO – PEO – PEO	0	0.120	4

To parameterise the sulphobetaine group in the zwitterionic ligand terminal we considered a polymer made of 8 sulphobetaine monomers for which simulations at atomistic level have been performed by Ghobadi *et al.* [121]. Each monomer is composed by three C1 beads which are the backbone of the polymer and by a side chain containing the sulphobetaine group, modelled by a positively charged Q_0 bead, a C1 bead and a negatively charged Q_{da} bead, preceded by the N fragment of a lysine, modelled with a P3 bead. Each monomer is then built with 7 beads which are shown in figure 26. Since the hydrophobic separator between the two charged beads is only three CH_2 groups long, a Martini small type should be used; however we decided to use a standard C1 type and shorten the bond length of the bead with the charged beads. Three different values of the angle constant, namely 2, 25 and 100 kJ mol^{-1}, for the Q_0 – C1 – Q_{da} angle were tested to reproduce the RDF of the Q_{da} beads with respect to the Q_0 beads. To compute the RDF the sulphobetaine polymer has been solvated by about 70000 water molecules and equilibrated for about 200 ns. The RDF has been computed choosing

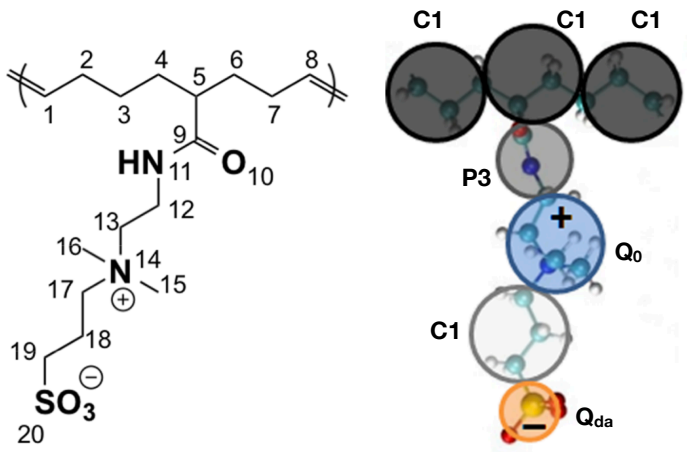

Figure 26: Left. Chemical representation of a sulphobetaine monomer. Right: Mapping for the sulphobetaine monomer. Black beads represent the hydrophobic backbone moieties (C1), the grey bead (P3) the N fragment of lysine, blue and orange beads the positively (Q_0) and negatively (Q_{da}) charged groups, respectively. The two charged beads are separated by a hydrophobic C1 beads (white).

one Q_0 bead and considering all Q_{da} beads which are not bound the Q_0 bead. The results are shown in figure 27 for the three angle constants. From the analysis of the RDF of the Q_{da} bead bound to the Q_0 bead, the angle constant of 2 kJ mol^{-1} rad^{-2} was excluded since this bond constant led to the superimposition of the two charged beads. No large difference was observed for the 25 and 100 kJ mol^{-1} rad^{-2} angle constants so we decided to keep the standard value of the Martini model, 25 kJ mol^{-1} rad^{-2}.

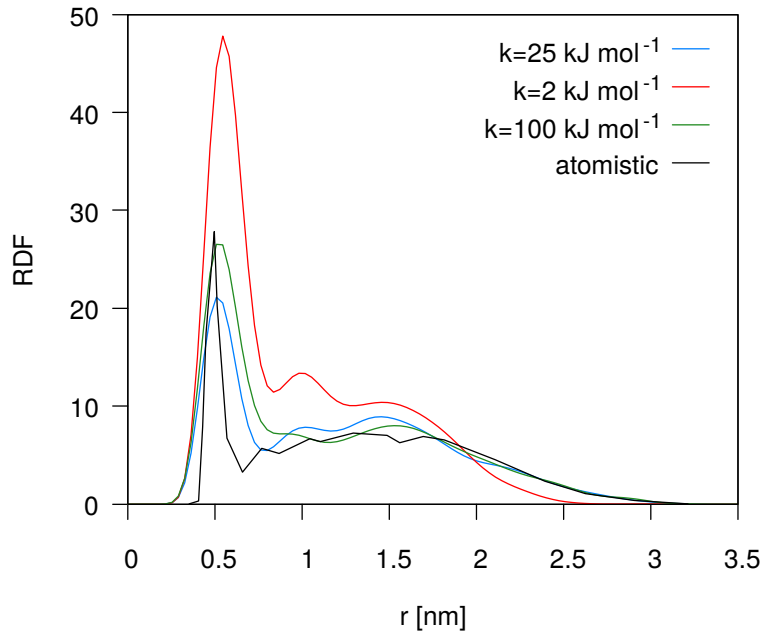

Figure 27: Radial distribution function RDF for the sulphobetaine 8-mer for the three values of angle constant we tested. The RDF has been computed for all Q_{da} which are not bound to the Q_0 bead chosen as a reference. Atomistic data extrapolated from [121].

4 HYDROPHOBICITY, CHARGE AND LIGAND CONFORMATION DRIVE NP–PROTEIN INTERACTION

Contents

When NPs are intravenously injected in the body, they have to travel in the blood stream encountering a variety of biological molecules among which there are proteins: NPs are soon covered by a corona of proteins which determine their interactions with the cells. If the adsorption of proteins is not controlled, the protein corona can lead to NP early clearance from the blood stream or alters the functionality of the NPs. To avoid undesired interactions, NPs are usually covered with anti-fouling ligands. PEG has proven to be very efficient in preventing protein adsorption. Even better results seems to be achievable with zwitterionic ligands. In this chapter we show how the interplay of chemical and conformational features of the ligand shell can influence the interaction of zwitterionic NPs and the most abundant serum protein, HSA.

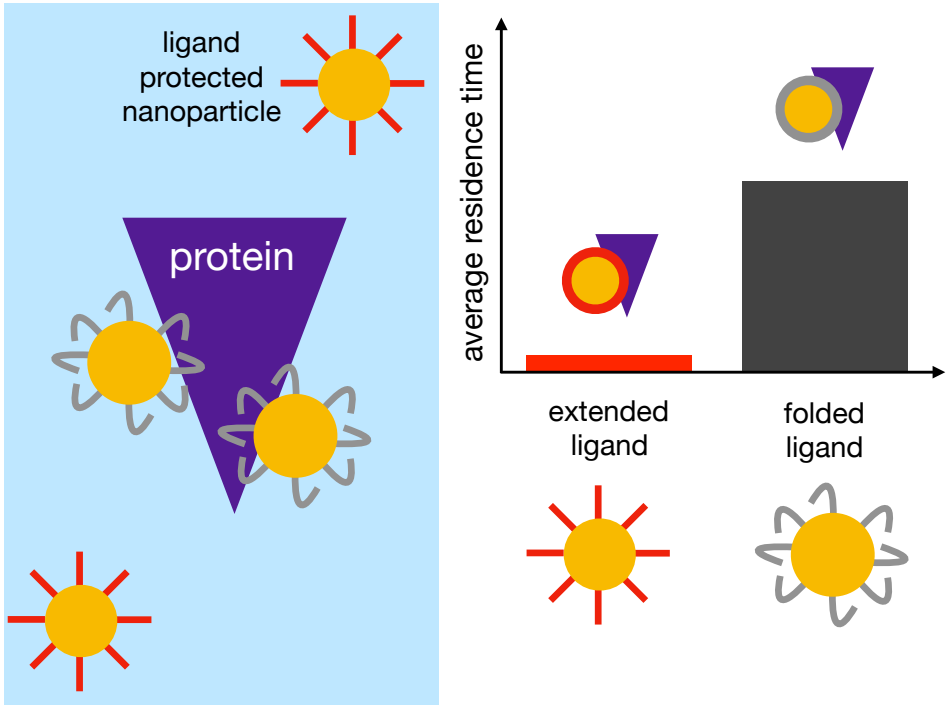

4.1 Proteins

Proteins are a class of macromolecules made of fundamental units, called amino acids, which are characterised by the same basic structure: a backbone, which is the same for the different amino acids, and a side chain, which is proper of each amino acid. The backbone is made of a central carbon atom, named C_α, to which an aminic $–NH_2$ (N terminus) and a carboxylic –COOH (C terminus) groups are bound. To build proteins a peptide bond is formed between the N and C termini of two consecutive amino acids, which are named residues. The peptide bond is planar, that is the two C_α atoms, the N and C atoms involved in the bond and the hydrogen and oxygen atoms which are bound to the N and C atoms, respectively, belong to the same plane: this is due to a partial double bond character of the peptide bond (see figure 28). Another characteristic of the peptide bond is its polarity: the N atom involved in the bond acquires a partial positive charge while the O atom bound to the peptide C atom is partially negatively charged.

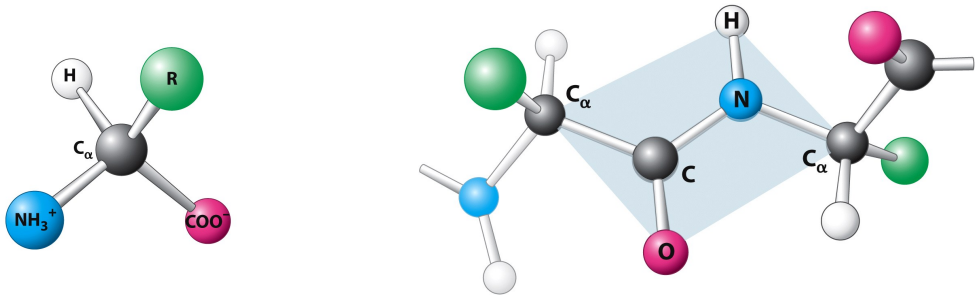

Figure 28: Left: schematic structure of an amino acid. Right: schematic structure of the peptide bond. The plane of the bond is shown in grey. Adapted from [122].

There are about 500 naturally occurring amino acids but only 20 of them are encoded in the genetic code: they are shown in figure 29. Different classifications of amino acids are possible depending on the properties at which one is looking. In this thesis we consider a classification based on amino acid side-chain hydrophilicity, as shown figure 29.
Each protein is identified by a sequence of amino acids which constitute the *primary* structure of the protein. Once the synthesis of a protein by the ribosomes ends, the protein starts to fold into its 3D structure which is called *tertiary* structure. The tertiary structure of a protein, also known as folded state, is made of regular sub-structures, namely α-helix and β-sheet, the *secondary* structure of a protein, which are defined by patterns of hydrogen bonds between the backbone peptide groups. Some proteins are made of two or more sub-units which constitute the monomers of the *quaternary* structure of these proteins. The different structures of proteins are shown for the proliferating cell nuclear antigen (PCNA) in figure 30.

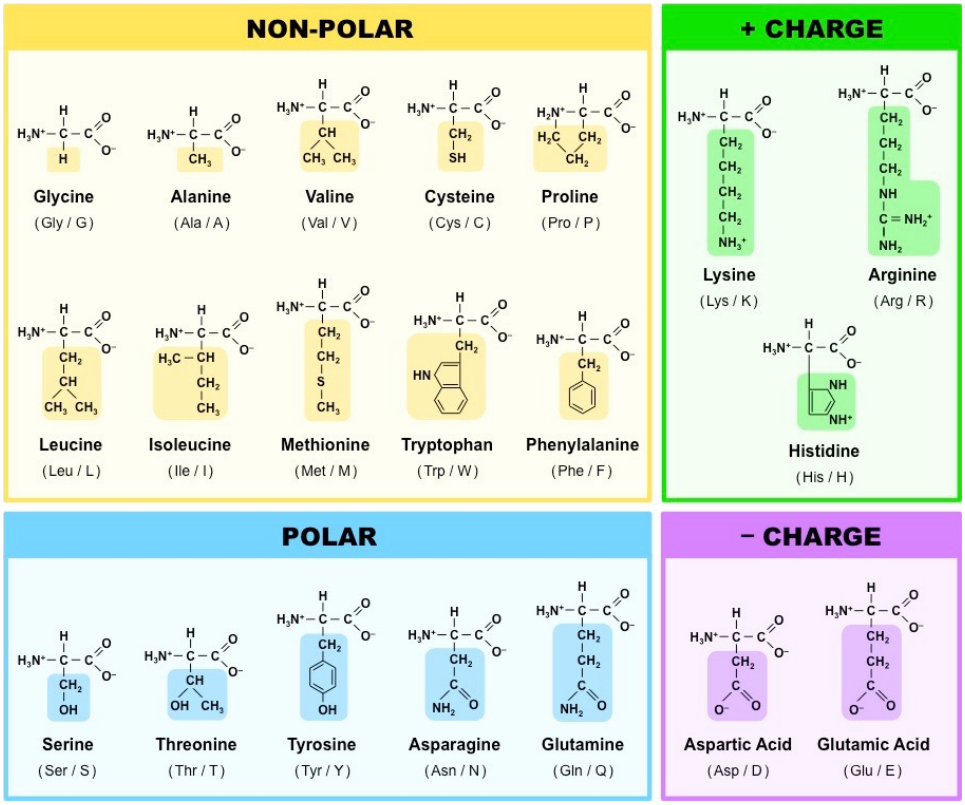

Figure 29: Classification of the 20 genetically-encoded amino acids in hydrophobic, charged and polar. Taken from http://ib.bioninja.com.au/standard-level/topic-2-molecular-biology/24-proteins/amino-acids.html.

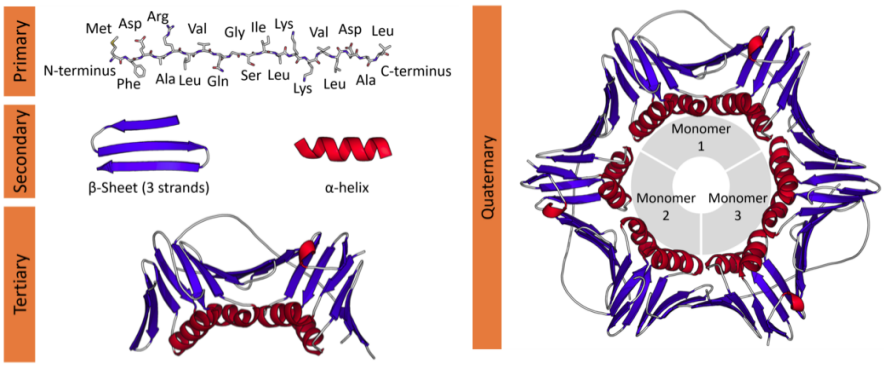

Figure 30: Left: primary, secondary and tertiary structure of proteins. The primary structure is made by the linear sequence of amino acids. Two secondary structures, namely α-helix and β-sheet, are formed by a regular network of hydrogen bonds. The combination of secondary structures in a 3D conformation form the tertiary structure of the protein. Right: the assembly of multiple folded sub-units or monomers constitute the quaternary structure. Taken from https://en.wikipedia.org/wiki/Protein_structure.

Proteins can be divided in four classes: globular, fibrous, disordered and membrane proteins. Globular proteins have a spherical shape and are the most populated class. Proteins in blood, also known as plasma protein, belong to the globular and fibrous protein classes. Plasma proteins have different functions: they transport molecules like lipids and hormones or participate in the immune system. Human serum albumin (HSA) accounts for

about the 55% of the plasma proteins; its main functions are to maintain the osmotic pressure in blood and to participate in transport of lipids and hormones. Globulins, plasma proteins dedicated to the transport of ions and hormones, make up about the 38% of blood proteins. The remaining 7% of plasma proteins is made of fibrinogen and other proteins which work as enzymes.

4.2 Human serum albumin

HSA is the most abundant protein in plasma. The structure of HSA has been experimentally determined with x-ray diffraction experiments: it displays only α-helix secondary structure arranged in a monomeric multidomain conformation.The structure of HSA is deposited in the protein data bank (PDB), which collects all the known structures of proteins, under the entry 1aO6 and is shown in figure 31. HSA has a weight of 66.5 kDa, it is made up of 585 residues and has a net negative charge of -15e, e being the absolute value of the electron charge.

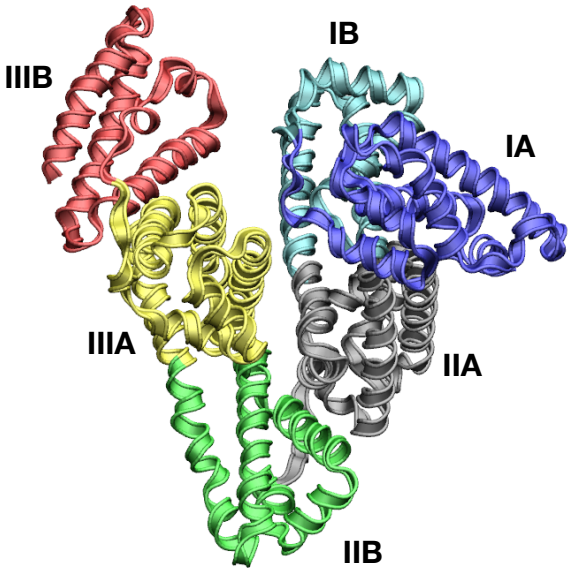

Figure 31: 3D structure of human serum albumin. α-helices forming the six sub-domains of the protein are shown in ribbon representation. Different sub-unites have different colours. Coordinates taken from PDB entry 1aO6.

4.2.1 Atomistic model of HSA

To developed a coarse-grained model of HSA we first built its atomistic version and used the properties derived from atomistic simulations as a target for the coarse-grained model. To parameterise the atomistic model we used the ff99SB-ILDN version of the Amber force field [83]. In the PDB structure file, the first four and the last three residues are missing. To neutralise the endings of the protein, two capping residues, an ACE group at the N-terminus and an NH_2 group at the C-terminus, have been introduced. The topology file, including particle definition, bonds angles and dihedral angles parameters,

has been generated from the modified coordinate file with the GROMACS tool *pdb2gmx*.

4.2.2 Coarse-grained model of HSA

We developed a coarse-grained model of HSA based on the ELNEDIN version of the Martini model [95]. The Martini force-field was first developed for lipids [92] and only at a later time extended to proteins [94, 95]. According to the philosophy of the original version, four heavy atoms are grouped into a single bead. For amino acids, one bead is used to model the backbone (BB) of each residue and zero to four beads are used to model their side chain, depending on the residue type. The mapping for the 20 genetically encoded amino acids is shown in figure 32. The backbone bead type depends on the secondary structure in which the residue participate: in coils the backbone shows a highly polar character which is strongly weakened by the hydrogen bonding network present in α-helices and β-sheets. In the Martini model proteins cannot change their secondary structure which is fixed by a combination of angle and dihedral angle potential energy functions. Thus, it is possible to distinguish between different secondary structures but no transitions between them are allowed. Movement of secondary structures with respect to each other are instead permitted.

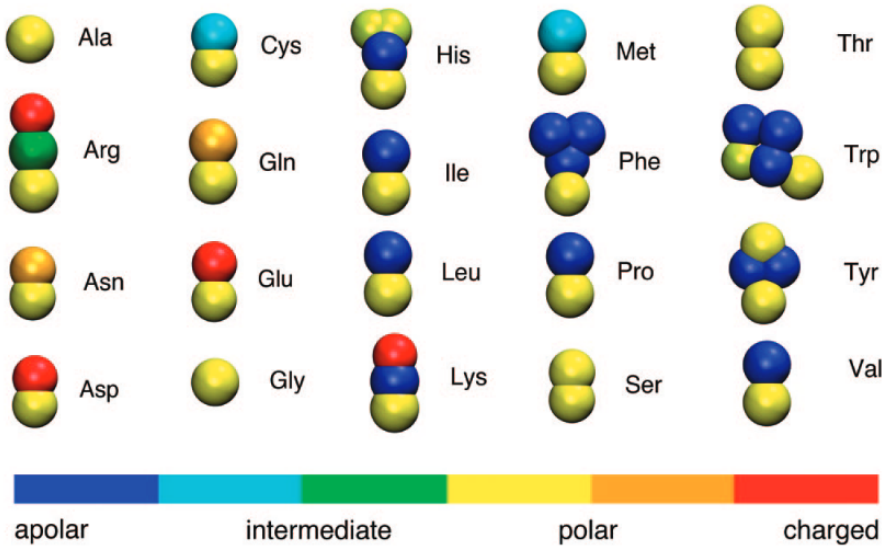

Figure 32: Mapping of all amino acids. Different colours represent different bead types. Taken from [94]

To improve the coarse-grained representation of structural and dynamical properties of proteins, including their collective motions, the Martini model has been combined with an elastic network model: the representation that emerges is based on both structural and thermodynamic properties and is termed ELNEDIN. In the ELNEDIN version of the Martini model bonded interactions are slightly modified since the position of the backbone beads now coincides with the C_α position and no more with the centre of mass of the backbone atoms. The elastic network is superimposed to the backbone beads and involves only beads within a cut off distance R_c which can be

tuned together with the elastic constant K to reproduce the atomistic model of the protein of interest.
To develop our model of HSA we varied the elastic constant of the elastic network while keeping the cut-off radius fixed at R_c = 0.9 nm. We also modified the BB–BB bond constant (common to all amino acids) and set the maximum value of the BB–side-chain bond constant (specific of each amino acid) to 25000 kJ mol^{-1} nm^{-2}.

Target properties for model refinement To fit the parameters of our Martini model of HSA we considered three target properties, namely the root mean square deviation (RMSD), the root mean square fluctuation (RMSF) and the superimposition of principal components, identified by the root mean square inner product (RMSIP) of the principal components. The RMSD represent the average deviation in time of the position of the C_α beads from the experimental structure of the protein as described in the PDB coordinate file. The RMSF refers to the fluctuation of the position of the C_α bead of each residue from its mean position. The RMSIP accounts for the superimposition of the first principal components of the atomistic and coarse-grained models. Principal components are derived from the diagonalisation of the covariance matrix $[C_{ij}]$ whose elements are given by

$$C_{ij} = \langle (q_i - \langle q_i \rangle) \cdot (q_j - \langle q_j \rangle) \rangle$$

where q_i is one of the Cartesian coordinates of a C_α bead and $\langle q_i \rangle$ is its average value. The eigenvectors with the highest eigenvalues are said principal components of the covariance matrix. The RMSIP is nothing but the root mean square of the inner product between the first N principal components η in the atomistic (AA) and coarse-grained (CG) simulations, that is

$$\text{RMSIP} = \sqrt{\frac{1}{N} \sum_{i=1}^{N} \sum_{j=1}^{N} (\eta_i^{AA} \cdot \eta_j^{CG})^2}$$

Simulation setup To compute the RMSD, RMSF and RMSIP we performed a simulation run of 1.5 and 2 μs for the atomistic and each coarse-grained model, respectively. Simulations were performed at constant temperature (T = 310 K) and pressure (p = 1 bar) in a simulation box of volume 12x12x12 nm^3. The protein was solvated with about 60000 TIP3P water molecules in the atomistic simulation and with about 13000 PW molecules in each coarse-grained simulation. Salt at physiological concentration (150 mM) was added to the simulation box in both atomistic and coarse-grained simulations together with 15 Na^+ ions to balance the negative charge of the protein. In both atomistic and coarse-grained simulation the long range contribution of electrostatics was included with the PME method. RMSD and RMSF were computed using the GROMACS tools *rms* and *rmsf*, respectively. To diagonalise the covariance matrix we used the GROMACS tool *covar* and the RMSIP was computed with a home-made script. The list of the tested parameters and the corresponding RMSIP is reported in table 5 while the RMSD and RMSF are shown in figures 33 and 34 only for stable simulations, that is only for those simulations that reached the end of the 2 μs run.

Table 5: Parameters for the BB–BB bond constant and for the elastic network constant. Both constants are in kJ mol^{-1} nm^{-2}. The total time reached in each simulation is in ps. The stability of a simulation is evaluated on the total time: if the simulation stopped before reaching the end (total time < 2 μs) then the simulation is considered unstable (stability = n). The best combination of parameters is between red lines.

Parameters		stability	total time	RMSIP
BB–BB (x10^3)	ELNEDIN			
15	350	y		0.44728
45	350	y		0.46006
90	290	y		0.44742
90	350	y		0.48091
100	350	y		0.48504
100	650	y		0.50361
120	300	n	637 500	0.43224
120	350	n	1 034 800	0.55028
150	290	y		0.45487
150	350	n	1 003 100	0.47407
150	500	n	1 034 900	0.48546

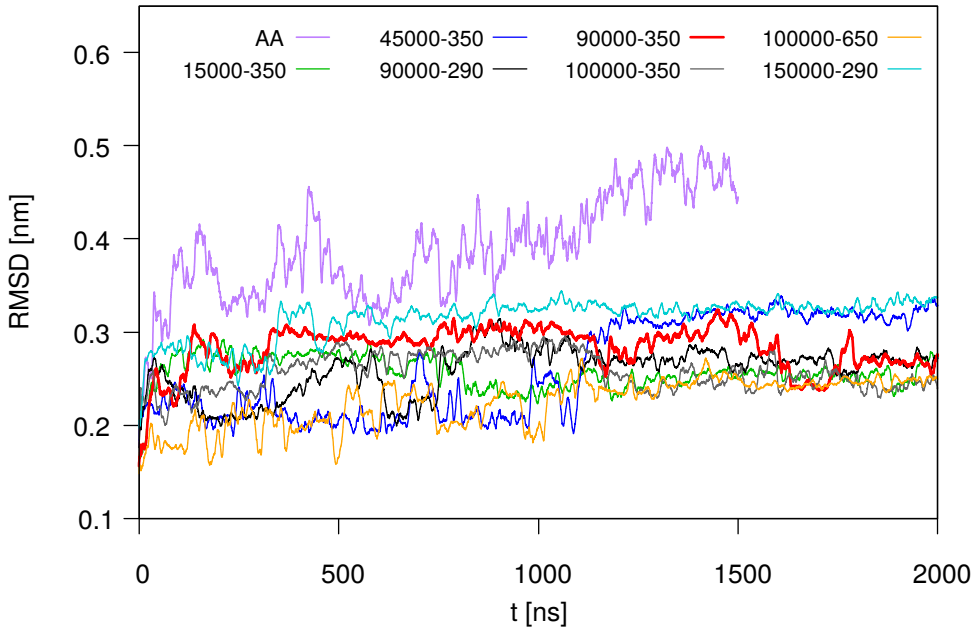

Figure 33: Comparison of the RMSD for the atomistic (AA) and the coarse-grained models. Coarse-grained models are labelled with a combination of two parameters: the first one refers to the BB–BB bond constant while the second is the elastic network constant. The RMSD for the best set of parameters (BB–BB bond constant = 90000 kJ mol^{-1} nm^{-2} and elastic network constant 350 kJ mol^{-1} nm^{-2}) is represented by thick red lines.

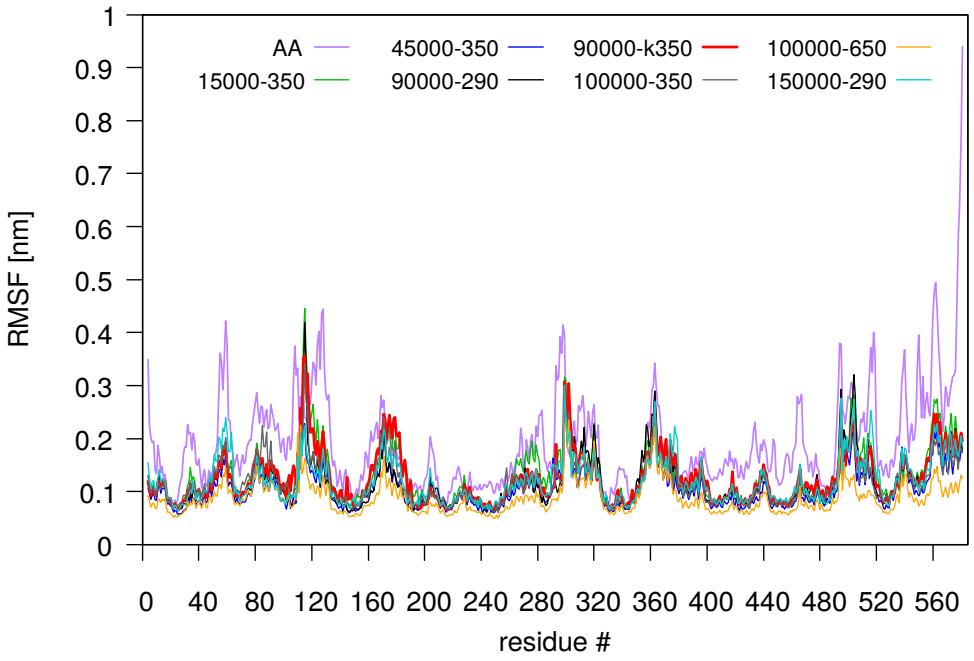

Figure 34: Comparison of the RMSF for the atomistic (AA) and the coarse-grained models. Coarse-grained models are labelled with a combination of two parameters: the first one refers to the BB–BB bond constant while the second is the elastic network constant. The RMSF for the best set of parameters (BB–BB bond constant = 90000 kJ mol^{-1} nm^{-2} and elastic network constant 350 kJ mol^{-1} nm^{-2}) is represented by thick red lines.

Looking at the three target properties, the RMSD, RMSF, RMSIP, the best set of parameters results in a BB–BB elastic constant of 90000 kJ mol^{-1} nm^{-2} and in an elastic network constant of 350 kJ mol^{-1} nm^{-2}. Even if the atomistic protein is more flexible than the coarse-grained one, as can be deduced from the larger value of the RMSD for the atomistic model, the superimposition of the peaks in the RMSF is pretty good and the RMSIP is the largest among all simulations with similar RMSD and RMSF profiles. The elastic network built on the protein backbone is shown in figure 35.

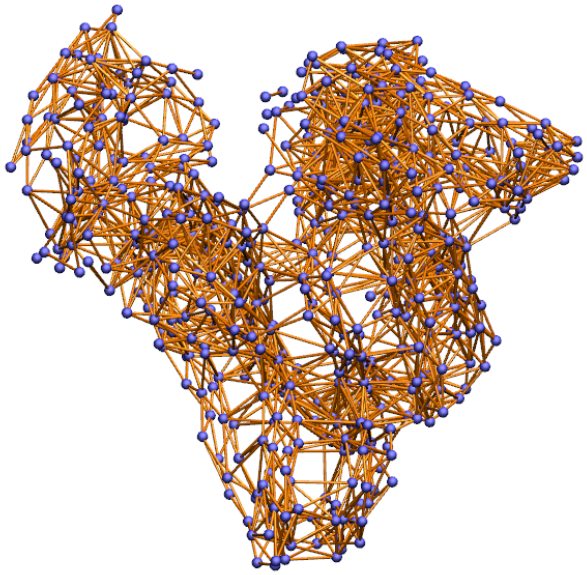

Figure 35: Elastic network (orange) superimposed to the backbone (blue beads) of the HSA.

4.3 NP–protein interaction

We studied the interaction of two zwitterionic NPs, differing for the hydrophobic content in the terminal group, and the most abundant protein in blood, HSA. The models of the ligands which functionalise the NPs are described in subsection 3.2.2. The least hydrophobic NP, from now on indicated with Z, is functionalised with 60 ligands terminated by a zwitterionic sulphobetaine group, while the most hydrophobic NP, from now on named ZH, is covered with 60 ligands whose terminal group is a di-butane sulphobetaine group. An example of ligand-protected gold NP, the coarse-grained representations of the ligands and of the protein are shown in figure 36.

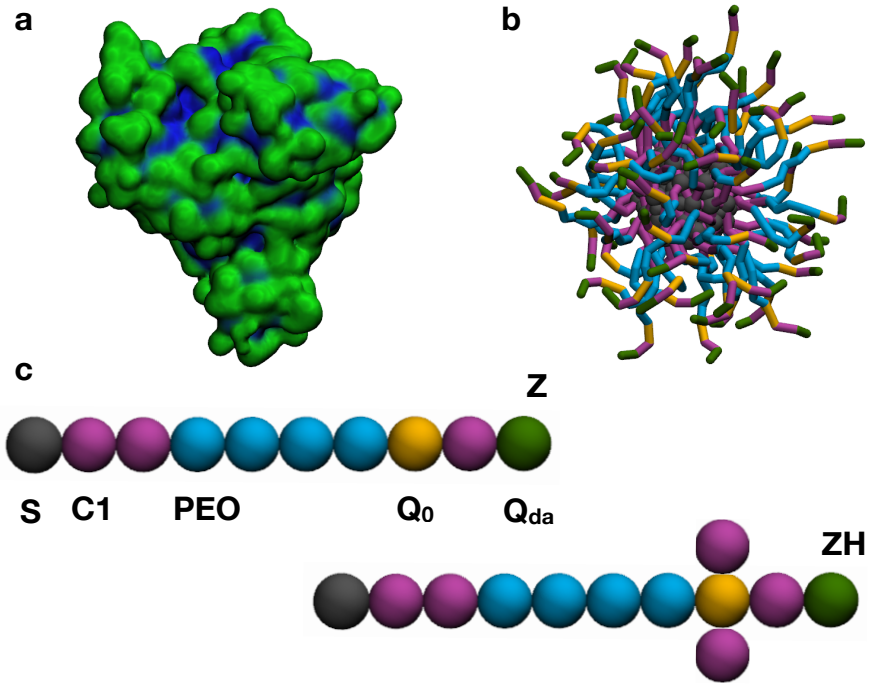

Figure 36: a. Surface representation of the coarse-grained protein. Surface residues are in green while bulk residues are in blue. b. Ligand-protected NP functionalised with Z ligands. c. Coarse-grained model of the least (Z) and most (ZH) hydrophobic ligands. C1 beads are in purple, PEO beads in blue, positively (Q_0) and negatively (Q_{da}) charged beads in orange and green, respectively.

Simulation setup To characterise the NP–HSA interaction we performed unbiased simulations in which a single NP, either Z or ZH, was allowed to interact with a single HSA (see figure 37). We set up 20 runs for NP type starting with different NP–HSA reciprocal orientation. The NP–HSA complex was solvated by around 52000 PW molecules in a box of volume 20x20x20 nm^3. Salt at physiological concentration (150 mM) together with 15 Na^+ counterions were added to the water phase. Each system was first minimised and equilibrated for 20 ns before the production run. For each of the 20 simulations we performed a 3 μs run at constant temperature (T = 310 K, velocity-rescale thermostat with time constant τ = 1 ps) and pressure (p = 1 bar, Parrinello-Rahman barostat with time constant τ = 12 ps, isotropic coupling and compressibility 3x10^{-4} 1/bar).
Since a new model of PEG was published by Grunewald *et al.* [123], which improves the previous model by Lee *et al.* [118] with corrected angle potential

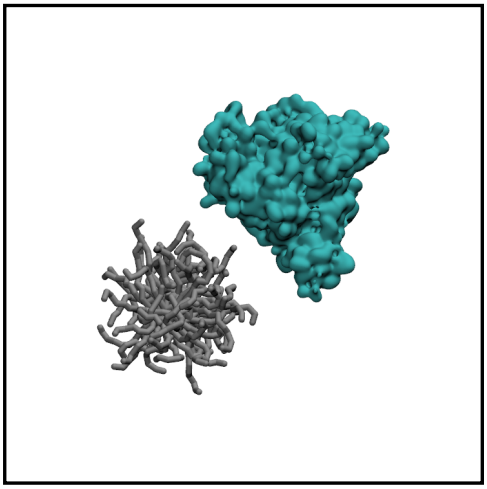

Figure 37: Front view of the initial configuration of one of the 20 simulations with the Z nanoparticle. The protein is shown in surface representation in cyan while the Z nanoparticle, in stick representation, is coloured in grey. Water beads and ions, which are not shown for clarity, fill the volume of the box.

[120], we replaced the PEG stretch in both the Z and ZH ligands with the newest model and performed additional 5 simulations of 3 μs for each of the two NPs. The same simulation setup of the old model of PEG was used for the new PEG model. No differences in the behaviour of the NPs were observed with the two PEG models.
We also built a NP covered with 60 PEG ligands having the same length in number of beads as the Z ligand. We used the PEG model by Lee *et al.* with the angle potential correction and performed two simulations of 3 μs.

Z and ZH NPs have different residence times on HSA Our unbiased simulations showed that both the Z and ZH NPs could establish a transient contact with the protein. We considered the NP in contact with the protein if at least two beads were closer that 0.8 nm. The number of contacts as a function of time was computed with the GROMACS tool *mindist*. We defined the average residence time $\langle t \rangle$ of each NP as the average time that a NP spent in contact with the protein. To compute the average residence time, we averaged over the 20 simulations the time stretches in which the number of contacts was different from zero. We found that the average residence time for the ZH NP is $\langle t^b_{ZH} \rangle$ = 34.2 ± 0.3 ns, while for the Z NP $\langle t^b_Z \rangle$ = 3.91 ± 0.01 ns. Thus, the most hydrophobic NP resides longer on the protein surface than the least hydrophobic NP (see figure 38). From the average residence times, it is possible to estimate the difference Δ^u between the unbinding free energy barriers for the two NPs:

$$\frac{\langle t^b_Z \rangle}{\langle t^b_{ZH} \rangle} = e^{-(\Delta G^\ddagger_{ZH} - \Delta G^\ddagger_Z)/k_B T}$$

$$\Delta^u = \Delta G^\ddagger_{ZH} - \Delta G^\ddagger_Z = -k_B T \ln\left(\langle t^b_Z \rangle - \langle t^b_{ZH} \rangle \right) \tag{4.3.1}$$

$\Delta G^\ddagger$ being the height of the unbinding barrier for each of the two NPs. Substituting the values for $\langle t^u \rangle$ for the Z and ZH NPs, Δ^u is equal to 2.25 k_BT. An analogous calculation can be done for the binding barriers. The average non-contact time is calculated as the mean of the time stretches in which the number of NP–HSA contacts is zero; for the Z NP $\langle t^u_Z \rangle$ = 42.9 ± 0.1 ns while for the ZH NP $\langle t^u_{ZH} \rangle$ = 51.6 ± 0.2 ns which results in a binding free energy difference Δ^b of 0.19 k_BT.

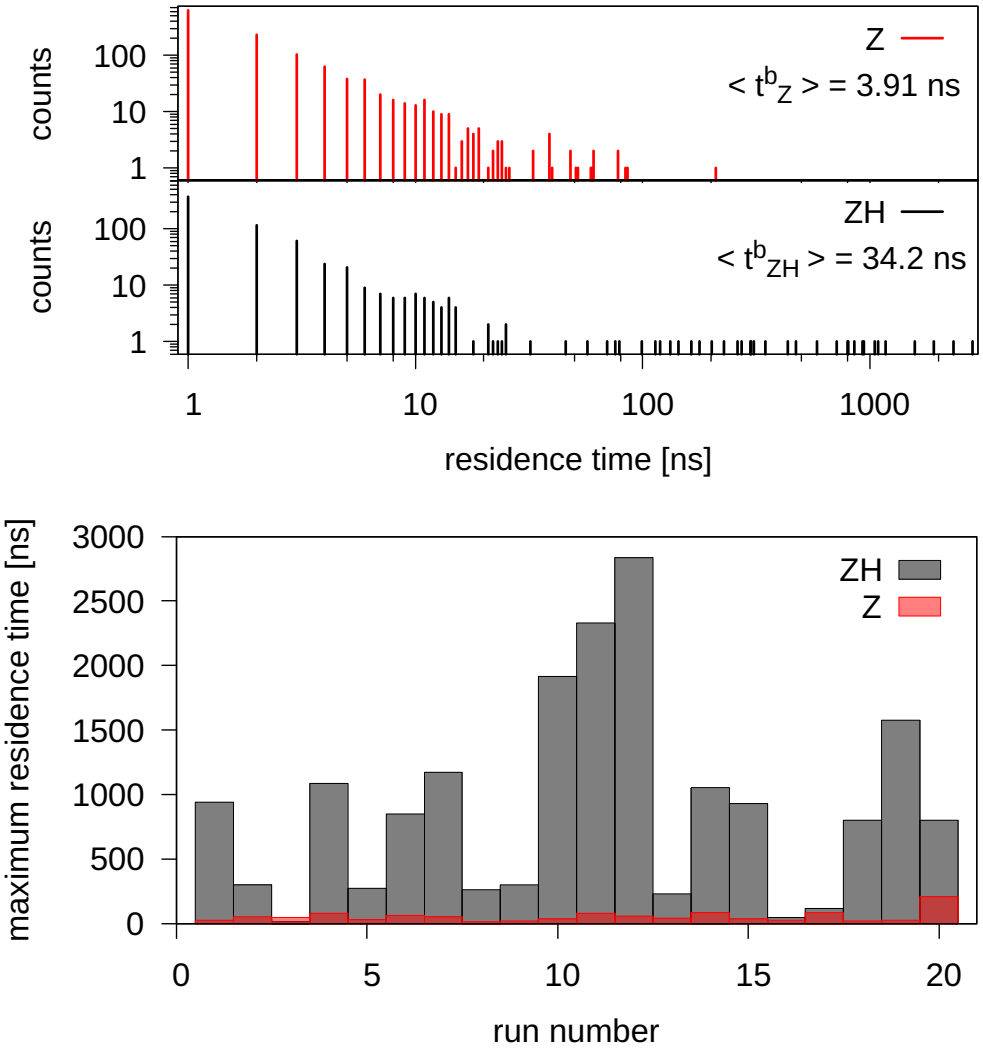

Figure 38: Top: distribution of the residence time for both the Z (red) and ZH (grey) nanoparticles. Bottom: Maximum residence time reached in each of the 20 simulations for both the Z and ZH nanoparticles.

To prove the higher efficiency of zwitterionic ligands compared to PEG in disfavouring protein adsorption, we performed simulations with a PEGylated NP and we found that the NP–protein binding is irreversible in the simulation time, as it can be seen in figure 39. The results of our simulations well match the experimental finding by Moyano *et al.* [46] suggesting that, conversely to zwitterionic NPs, a hard protein corona is formed around PEGylated NPs.

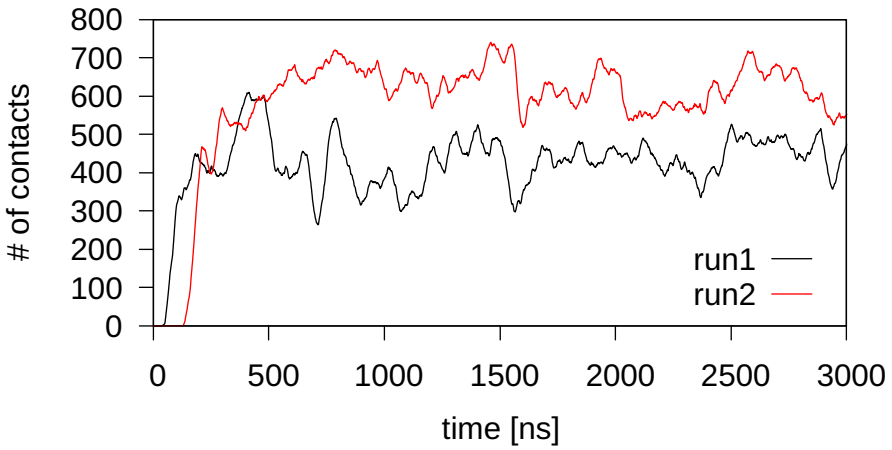

Figure 39: Number of contacts as a function of time for the two simulations performed with a PEGylated NP.

ZH ligands expose PEG to the HSA surface Since the only difference between the Z and ZH ligands resides in the two additional hydrophobic beads in the ZH terminal group, we monitored the number of contacts between different parts of two NPs and different parts of the protein. We classified protein residues based on their affinity with water: polar, charged and hydrophobic residues were selected according to figure 29. Moreover, we divided protein residues in surface and core residues independently on their character. The classification of residues was based on their solvent accessible surface area (SASA): for each residue its SASA was computed with the GROMACS tool *sasa* using a PW bead as a probe, then the maximum value of SASA was assigned to each residue according to Tien *et al.* [124]; eventually, if the ratio between the computed and maximum SASA was below a threshold of 0.1, residues were considered as core residues, otherwise as surface residues. We used only surface residues to compute the number of NP–HSA contacts for both different parts of the protein and of the NPs. Each time that either the protein or the NP were split in different groups, the number of contacts was normalised by the number of beads per group. We computed the number of contacts between the whole protein and either the Z or ZH NP and found the Z NP binds quite uniformly on the protein surface, conversely to the ZH NP which shows two preferential binding sites, as it can be seen in figure 40. These binding sites contain both hydrophobic and charged residues. Despite the different number of hydrophobic beads in the Z and ZH ligands, the number of contacts between either the Z or ZH NP and the hydrophobic surface residues of the protein is roughly the same (see panel d in figure 40).
We considered the number of contacts between different beads in the Z and ZH ligands and the whole protein; in particular, the C1 beads were distinguished in those attached to the NP surface and those belonging to the zwitterionic terminal ($C1_T$). As shown in figure 41, the percentage of PEG contacts for the ZH NP is largely different from those of the Z NP. Moreover, the more hydrophobic NP showed a smaller number of terminal hydrophobic contacts ($C1_T$) with respect to the Z NP, even if the hydrophobic content is lower for this NP.
To explain this unexpected behaviour we looked at the structural properties of the two ligand types, computing the RDF of different ligand moieties with

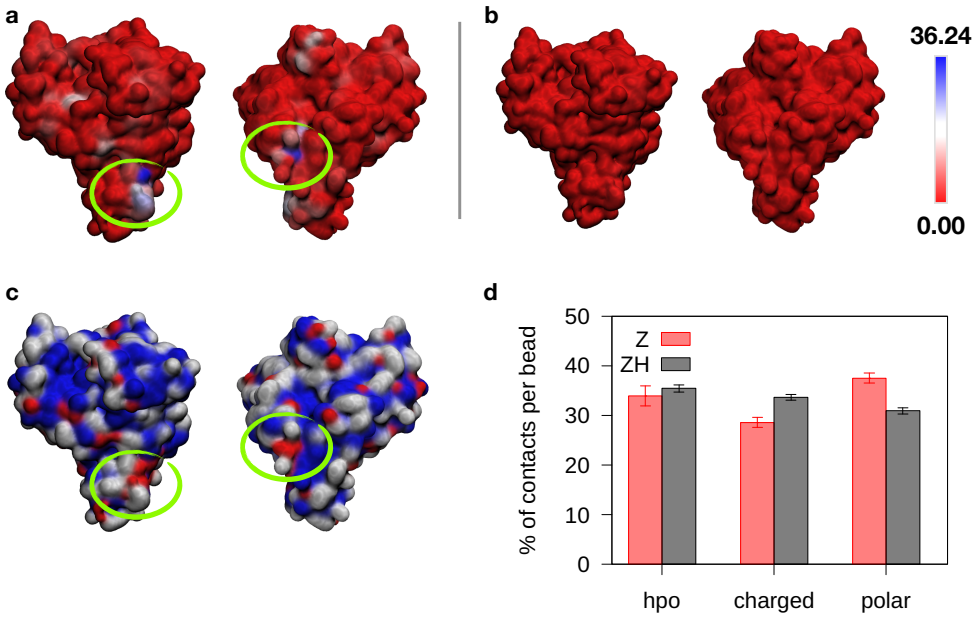

Figure 40: a and b: surface representation of the protein coloured by average number of contacts with the ZH and Z nanoparticles, respectively. The same colour scale is used for the two nanoparticles. c: surface representation of the protein coloured by residue polarity: hydrophobic residues in red, charged in white and polar in blue. d: histogram of the NP–protein contacts for different residue types.

respect to the COM of the gold core. The Z ligands extend in the water phase while the terminal groups of the ZH ligands are found closer to the NP surface suggesting a folded conformation (see figure 42). In this configuration, the more hydrophobic terminal is screened from water while the central PEG stretch is exposed to the water phase and is thus more prone to interact with the protein. Therefore, not only the chemical composition, but also ligand conformation affects the interaction between NPs and proteins.
Looking back at the small difference in the free energy barrier of binding for the Z and ZH NPs, we attempted to understand if a correlation could be found with the different ligand conformations. Indeed, the folded configuration of the ZH ligands resulted in a lower hydration of the ZH NP as it can be seen from figure 42, bottom panel. We computed the number of contacts between the Z or ZH ligands and the W particle of the PW beads, reported in table 6, in two states, the one in which the NP is in contact with the protein and that in which the NP is swimming in the water phase. The difference in the number of contacts in these two states clearly shows that the ZH NP loses the largest number of water molecules upon binding to the protein: this is coherent with the largest free energy barrier of binding observed for the ZH NP with respect to the Z NP.

Ligand conformation affects NP–protein interaction With the help of unbiased coarse-grained molecular dynamics simulations we investigated the interaction of monolayer-protected zwitterionic AuNPs with the most abundant protein in human serum, albumin (HSA). We considered two kinds of zwitterionic NPs differing in the hydrophobic content in the zwitterionic terminal group. Our simulations showed that zwitterionic NPs can reversibly bind with HSA, conversely to other ligands, such as PEG, in good agreement

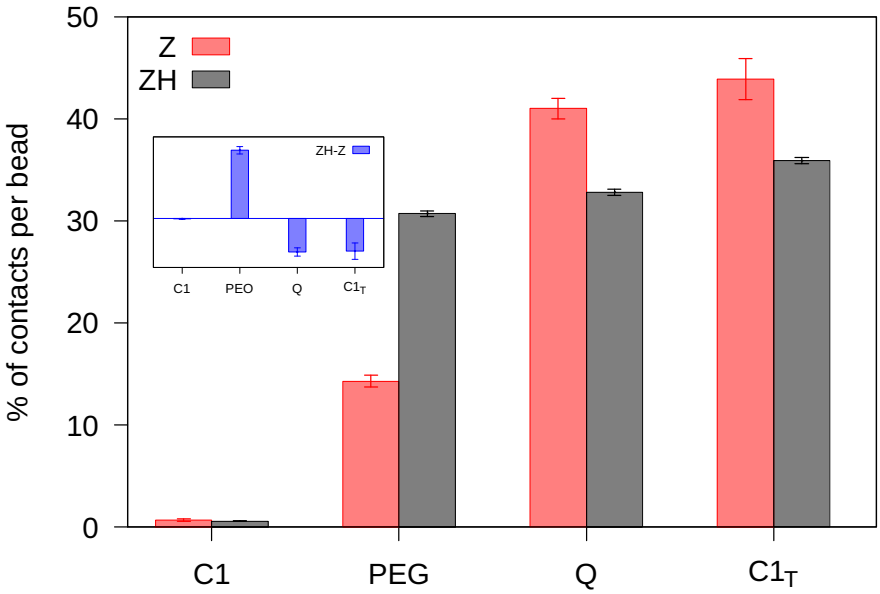

Figure 41: Histogram of the NP–protein contacts for different beads in the Z and ZH ligands. The C1 and $C1_T$ distinguish the hydrophobic beads closer to the NP core from the hydrophobic beads in the zwitterionic termini, respectively. PEG refers to the four PEO beads while Q includes both the positively and negatively charged beads in the ligand terminus. In the inset the difference (ZH-Z) between the percentage of contacts for different moieties in the ZH and Z ligands is shown.

Table 6: Number of contacts between the nanoparticle beads and the W particle of the PW beads. NC refers to the state in which the NP is not in contact with the protein, while C stands for the contact state. Zwitt indicates the zwitterionic terminal group of each of the ligands. The difference in the number of contacts between the non-contact and contact states is reported in brackets.

NP	NP–W (NC)	NP–W (C)	Zwitt–W (NC)	Zwitt–W (C)
Z	4909 $\pm$ 1	4889 $\pm$ 5 (-20)	1542 $\pm$ 1	1533 $\pm$ 2 (-9)
ZH	3950 $\pm$ 1	3821 $\pm$ 14 (-129)	1015 $\pm$ 1	985 $\pm$ 4 (-30)

with the experiments by Moyano *et al.* [46]. Our molecular-level interpretation of the experimental data suggests that the more stable binding of more hydrophobic ligands is due to their particular conformation, in which the hydrophobic moieties are folded towards the NP core and PEG moieties are exposed to water, rather than to hydrophobic interactions. Thus, the higher stability of the NP–protein complex for more hydrophobic NPs is determined by an increase in the PEG–protein contacts, which is compatible with the formation of a stable protein corona.

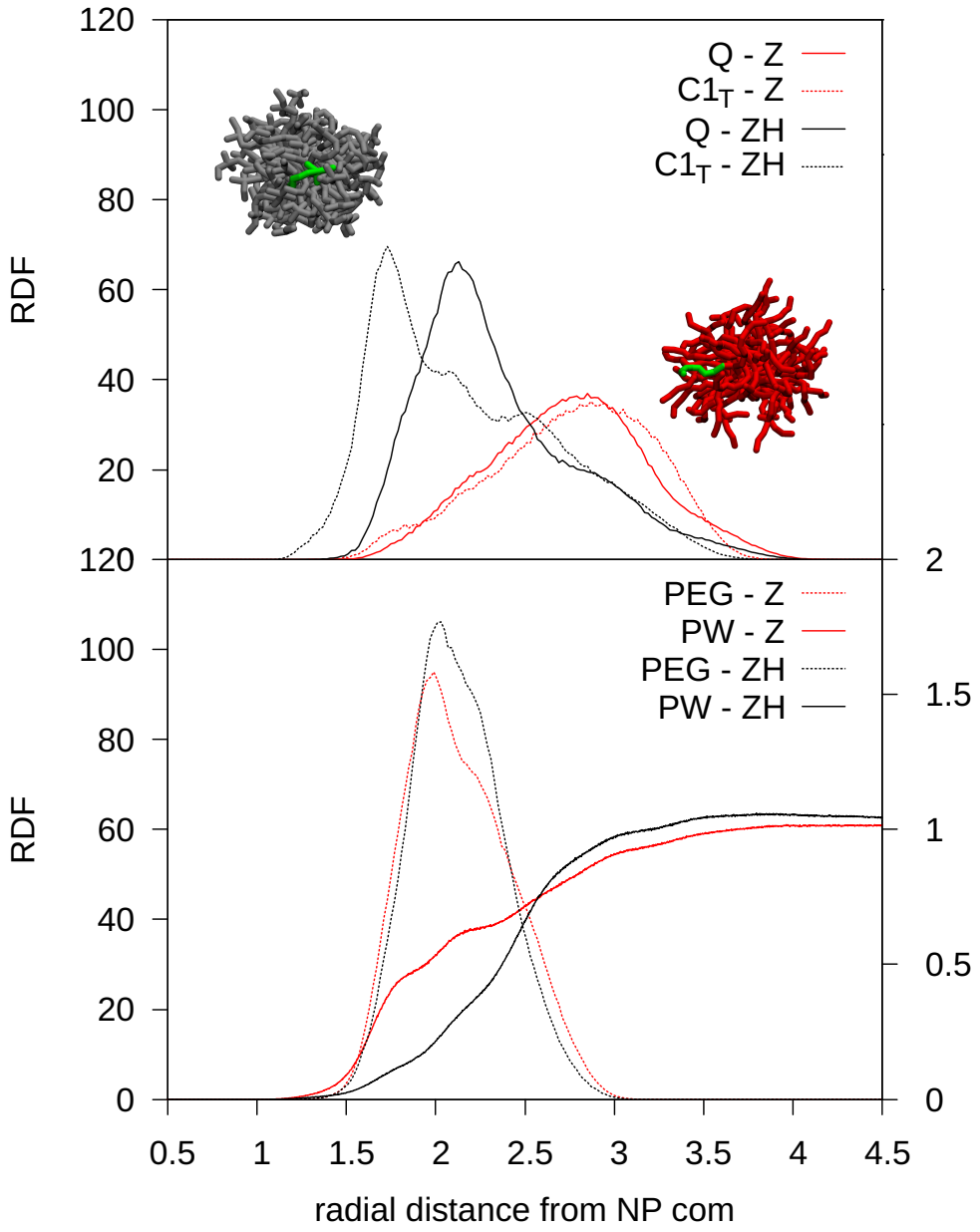

Figure 42: Top: radial distribution function for the charged (Q, solid) and hydrophobic ($C1_T$, dashed) beads in the terminal groups of both the Z (red) and ZH (grey) nanoparticles. In the insets the two nanoparticles are shown: ZH ligands in grey, Z ligands in red. Bottom: radial distribution function of the PEG moieties (dashed) and polarisable water (PW) (solid) for the Z (red) and ZH (grey) nanoparticles. For PW the y scale on the right is used.

5 GOLD NANOPARTICLES INTERACT WITH LIPID MEMBRANES WITH A THREE-STEP MECHANISM

Contents

Applications of NPs in the biomedical field require to understand and control the interactions of NPs with different biological environments. In chapter 4 we analysed the interaction of NPs with proteins, one of the major components of human plasma. In this chapter we study the interaction of NPs with cells membranes, which are the target for many applications of NPs in the biomedical field, such as controlled drug delivery, photothermal therapy and imaging. Cell membranes are the first barrier that NPs encounter when they successfully reach the target cells. To penetrate cell membranes, NPs follow different routes which depend on the nature of the NPs themselves. As for size, large NPs enter cell via endocytosis while small (< 10 nm) NPs can passively penetrate the cell membrane. Since the first mechanism is rather complex and involves many different players on different time and length scales, we focus on the second route which, as shown by some experimental data [30], [57], can be seen even in model membranes, thus removing some of the complexity of the system. We thus investigate, through molecular dynamics simulations, the interaction of functionalised NPs with model lipid membranes and show that small NPs can passively insert into the lipid membrane in a three stage process.

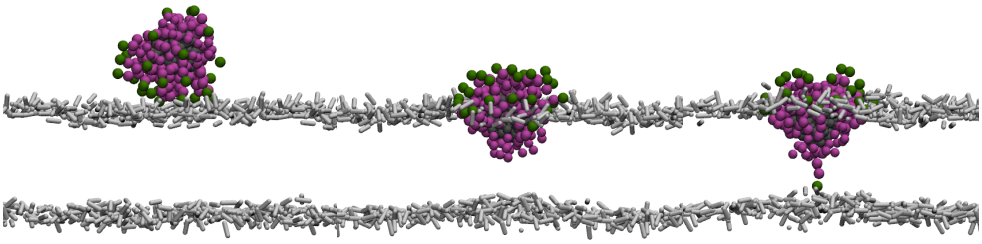

Simonelli et al. [60], Salassi et al. [125]

5.1 Natural and model cell membranes

In this section we describe the main characteristics of cell membranes and their model counterpart; a complete description of cell membranes, their properties and biological functioning can be found in the book "Life as a matter of fats" [126].

Mammalian cell membranes, also known as plasma membranes, are selective membranes which separate the interior from the exterior compartment of the cell and regulate the trafficking in and outside the cell. Cell membranes are mainly composed by a mixture of lipids and proteins. Phospholipids are the major lipid components of cell membranes; they are amphiphilic molecules made of two hydrophobic fatty acids, usually named *tails*, and a hydrophilic *head* containing a phosphate group (see figure 43). Glycolipids, lipids with a covalently bonded carbohydrate group, and sterols, among which cholesterol is the most abundant, are also present in cell membranes. The amphiphilic nature of the components of the membrane is

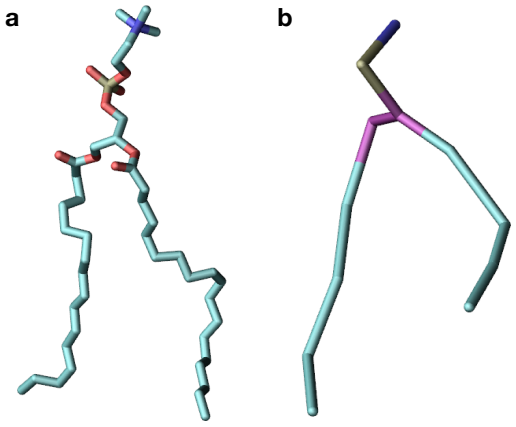

Figure 43: Schematic picture of an atomistic (a) and Martini (b) POPC lipid. Hydrophobic lipid tails are shown in cyan, phosphorus in the phosphate group in tan and nitrogen in the choline group in blue. In the Martini representation, glycerol groups are shown in magenta.

fundamental for its structure; since cells live in an aqueous environment, hydrophobic tails try to hide from the water phase for hydrophobic effect while hydrophilic heads face the aqueous phase. Lipids, then, self-assemble to form a bilayer with a hydrophobic core and two hydrophilic surfaces. A schematic picture of a cell membrane is shown in figure 44.

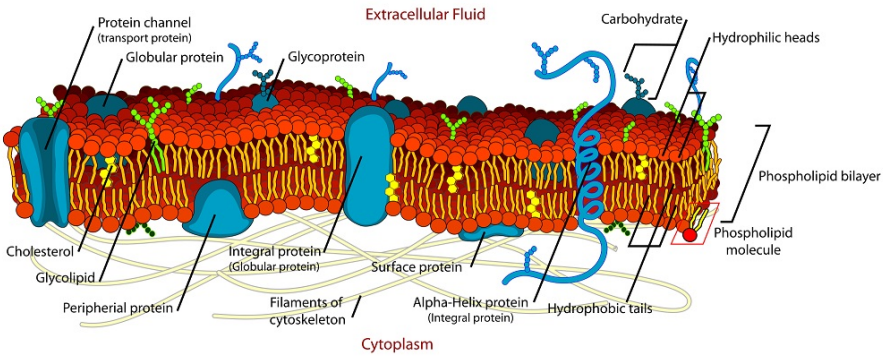

Figure 44: Schematic picture of a cell membrane. In the bilayer, mainly composed of phospholipids, different kinds of proteins are embedded. Cholesterol and carbohydrates are also present in the membrane. The cell membrane separates the exterior from the cytosolic environment. Taken from https://biologydictionary.net/cell-membrane/.

The composition of the lipid bilayer is not symmetric between the inner (facing the cytosol) and the outer (facing the extracellular fluid) leaflet: the inner leaflet is negatively charged due to the presence of phospholipids with a negatively charged head.

The fatty acids that form phospho- and glycolipids can be saturated, if no double bonds are present, or unsaturated, if one or more double bonds can be found in the lipid tails. Unsaturated fatty acids cause disorder in the packing of lipids tails thus influencing the fluidity of the membrane, which is in a fluid state at physiological temperature. From experiments of diffusion of labelled lipids [128, 127] and of vesicle disruption with detergents [129], it was shown that small-scale structures exist in the fluid cell membrane. These supramolecular entities, known as rafts, can float around in the fluid bilayer. A common feature of lipid rafts is the high content of cholesterol and sphingolipids, sphingomyelin in particular. The presence of saturated lipids, together with cholesterol, which favours lipid ordering, suggests that lipids in lipid rafts are in a liquid ordered phase. Proteins can be found in lipid rafts, too. The saturation level, together with the length of the fatty acids in the lipid tails also influences membrane thickness which is usually defined as the height of the region comprises between the lipid head groups of the opposite monolayers: membranes with the higher content in unsaturated lipids are thinner. Bilayer thickness, which is a key property for membrane functioning, is also influenced by the presence of cholesterol and by temperature, the higher the temperature, the thinner the bilayer.
Proteins are the other major component of plasma membranes. Conversely to lipids, which mainly have structural properties, proteins are responsible for membrane functions in selectively control the trafficking of molecules and in cellular recognition. Proteins contribution to the membrane mass is around 50%, the other 50% being supplied by lipids. However proteins are much larger than lipids so that a smaller number of proteins can be found in the membrane.
As it can be seen in figure 44, cell membranes are very crowded objects. Proteins on and embedded in cell membranes have different functions and can be the target of NPs, especially if they are protected by a protein corona. To study the effect of different NP properties on the biological membranes, unspecific interactions are usually preferred to limit the variability in the system. Thus, model membranes made only of lipids, and phospholipids in particular, are considered. Both lipid bilayers and lipid vesicles can be synthesised which are able to reproduce many characteristics of the natural lipid matrix of cell membranes such as softness and bending, phase transitions and domains and lipid raft formation. For these rather simple systems it is possible to measure some properties like the area per lipid, the bilayer thickness, its bending modulus, phase transition temperatures and so on. These properties can then be used as a target when computational models of lipids are developed in order to gain a molecular-level insight into the processes which involve lipid membranes.

5.2 Atomistic and coarse-grained models of lipid membranes

Given that the model membranes we consider are made only by lipids, we decided to simplify the system at most and consider just a single component bilayer. In particular we chose the POPC lipid which is the most abundant in mammalian cell membranes. POPC, whose atomistic and coarse-grained models are shown in figure 43, is composed of a hydrophilic head, containing a negatively charged phosphate and a positively charged choline group, and

of two hydrophobic tails, the unsaturated oleoyl acid and the saturated palmitoyl acid.
At atomistic level we use the corrected version [87] of the Berger lipids [86] which is based on the OPLS force field. Within this model a united atom representation is used so that CH_2 groups in the POPC tails are coarsened into a single particle. We use a lipid membrane composed of 480 POPC lipids, 240 per monolayer, or leaflet, which occupy an area of about 13x13 nm^2. The thickness of the membrane, computed as the difference between the positions of the head groups in the upper and lower leaflet of the membrane, is about 3.6 nm.
At coarse-grained level we used the Martini force field to model a POPC membrane made of 512 lipids, 256 per leaflet. The usual 4:1 mapping is used for POPC so that the phosphate and choline groups are represented by two charged beads, the glycerol termini of the fatty acids are modelled by a non-polar bead, each, and each of the two tails is made of four hydrophobic beads. The area occupied by the membrane, which is about 3.9 nm thick, is about 13x13 nm^2.

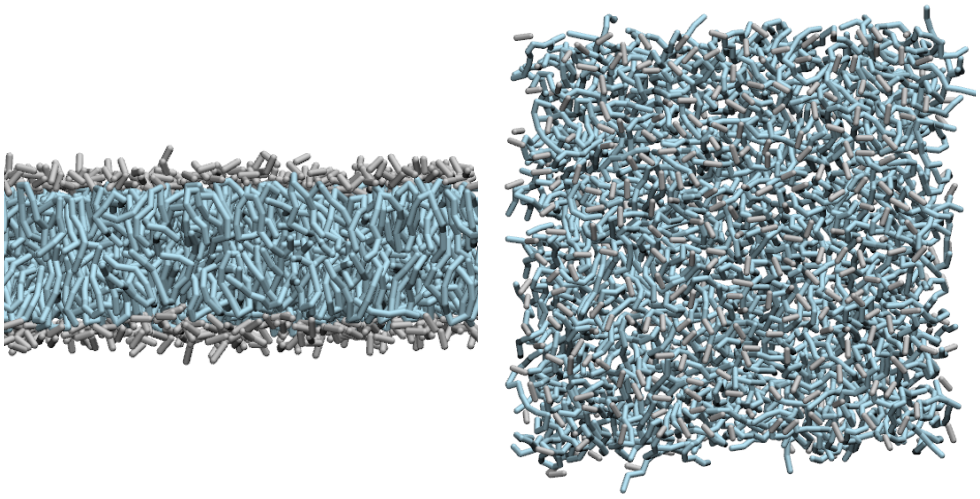

Figure 45: Left: front view of a coarse-grained POPC membrane. Right: top view of the same POPC membrane. Lipid heads are shown as light-grey sticks while lipid tails are in iceblue.

5.3 NP–membrane interaction

Cell membranes are the first barrier encountered by NPs when used in biomedical applications. Thus, the study of the interaction between NPs and model lipid membranes, which mimic the natural cell membrane, has experienced a growing interest. A key aspect of the NP-membrane interaction concerns the possibility for NPs to pass through the lipid membrane: this is particularly important for delivery applications of NPs. The penetration of NPs in lipid bilayers is still debated: recent studies by Tatur *et al.* [130] on supported lipid bilayers showed that anionic NPs could only adhere to the surface of zwitterionic lipid membranes without penetrating them. Conversely, experiments with dye-labelled NPs and multilamellar vesicles [57] showed that anionic NPs can reside in the core of the lipid membrane and even penetrate them without causing damage. These experimental observations

were supported by free energy calculation of NP insertion in the lipid membrane from the water phase. These simulations were based on implicit models of both the lipid membrane and the water phase. However, more accurate simulations, which explicitly considered both the membrane and water, could not observe spontaneous penetration of NPs in the membrane core [131, 132].
Another debated aspect of the NP-membrane interaction is related to the different pattern of ligands which can be arranged on the NP surface. For example, NPs with random, Janus [133, 134], and striped ligand arrangements can be synthesised. As shown in figure 46 Janus NPs are obtained when ligands phase separate in two distinct domains while for striped NPs the ligands arrange in alternating stripe-like domains.

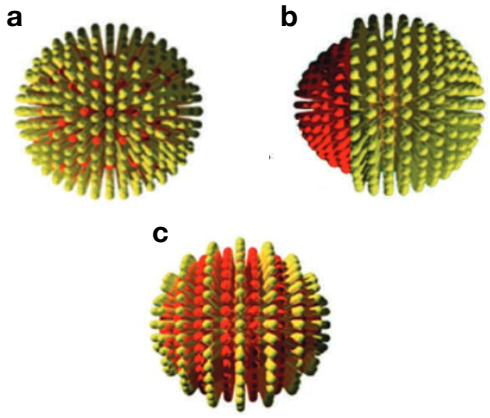

Figure 46: Schematic picture of different surface ligand arrangements. a. random, b. Janus, c. striped. Adapted from [135].

Again, the influence of the surface arrangement of ligands on NPs is still not clear. Verma *et al.* [136] showed that NPs with similar chemical composition but differing in ligand pattern were internalised into cells *via* different routes and, in particular, NPs with a striped arrangement could spontaneously penetrate the cell membrane. From thermodynamics consideration by Van Lehn *et al.* [57], however, no substantial difference in the free energy of translocation of random or striped NPs was found. Other computational studies by Gkeka *et al.* [131], who used an explicit model of water and lipid membrane to compute the free energy of transfer of NPs with different surface arrangements, demonstrated that homogeneous NPs are more easily internalised that random NPs.
We studied, at both atomistic and coarse-grained level, the interaction of a negatively charged NP, covered with a mixture of hydrophobic OT and anionic AN ligands in a 1:1 ratio (analogous to the ones synthesised by Van Lehn *et al.* [57]), with a POPC membrane. The anionic NP is functionalised with 30 OT ligands and 30 AN ligands (see section 3.2 for their atomistic and coarse-grained parameterisation), arranged in two different patterns, random and striped. The latter configuration is made up of a central hydrophobic stripe of OT ligands surrounded by two capping regions of AN ligands, as shown in figure 47.

Simulation setup To study the interaction between NPs and model lipid membranes we used unbiased coarse-grained simulations in which one anionic random 1:1 NP was inserted in a simulation box of volume 13x13x15 nm^3. The NP was placed above the membrane at a distance of about 2.5 nm (see figure 48) and the empty space in the box was filled with about 16000

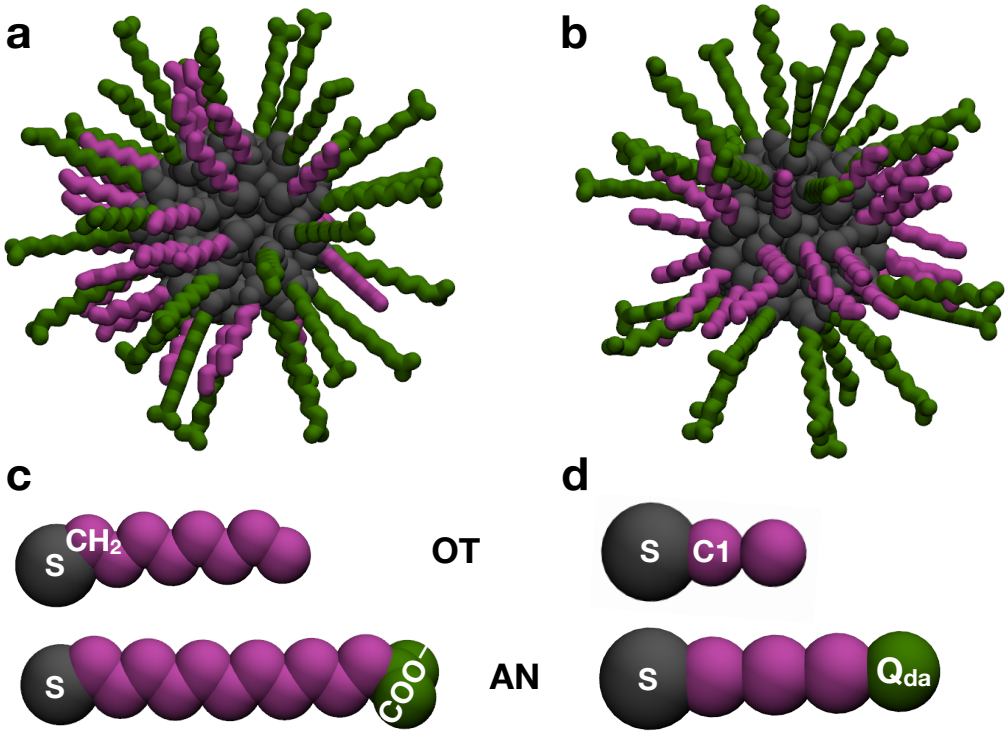

Figure 47: Atomistic representation of the random (a) and striped (b) anionic 1:1 NPs. Hydrophobic OT ligands are shown in purple while anionic ligands have the same colour (green) of their negatively charged terminal group. The core of the NP, including both gold and sulphur atoms, is in grey. Atomistic (c) and Martini (d) model of the OT and AN ligands. Sulphur atoms in grey, hydrophobic and charged moieties in purple and green, respectively.

standard Martini water beads, ions at physiological concentration (Na^+ and Cl^- at 150 mM), and 30 Na^+ counterions to neutralise the box. We performed four unbiased simulations for the random NP with length from 10 to 20 μs and five unbiased simulations for the striped NP with length 20 μs. Each production run was performed at constant temperature (T = 310 K, velocity rescale thermostat with time constant τ = 2 ps) and constant pressure (p = 1 bar, semi-isotropic Parrinello-Rahman barostat with time constant τ = 4 ps and in-plane compressibility of 4.5x10^{-5} 1/bar).
In all unbiased and metadynamics so far electrostatic interactions were cut-offed and shifted. However electrostatics plays an important role in the NP–membrane interaction. We thus compared different methods to treat electrostatics and the effect of water polarisation using atomistic metadynamics simulations as a target. The atomistic system is analogous to the Martini system: one NP and a POPC lipid membrane were inserted into a simulation box of volume 13x13x10 nm^3 which was filled with around 32000 water molecules, 30 Na^+ counterions to neutralise the box and salt at physiological 150 mM concentration. At atomistic level we performed two metadynamics runs for a total simulated time of about 1.9 μs. A Gaussian bias potential of height 1 kJ/mol and σ 0.06 nm was used. Temperature was kept constant at 310 K, using a velocity-rescale thermostat with time constant τ = 1 ps. The semi-isotropic Parrinello-Rahman barostat with time constant τ = 1 ps and compressibility 4.5x10^{-5} 1/bar was used to maintain a constant pressure

of 1 bar. At coarse-grained level we tested three models: the standard Martini (SM), the standard Martini with long range electrostatics (MPME) and the polarisable Martini with long range electrostatics (MPW). The total simulated time is 5.5, 7.3 and 31.4 μs for the SM, MPME and MPW model, respectively.

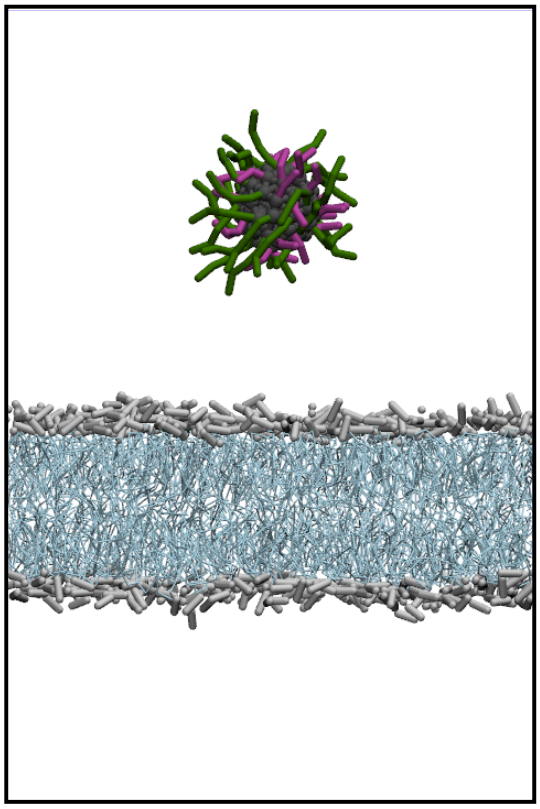

Figure 48: Starting configuration of unbiased Martini simulations. The anionic NP is put 2.5 nm above the membrane head region. The core of the NP is in grey, anionic ligands in green, hydrophobic ligands in purple. The lipid membrane in shown in stick representation, lipid heads in light-grey, lipid tails in iceblue.

The NP–membrane interaction is a three-stage process Unbiased MD simulations of both random and striped NPs showed that the NP–membrane interaction is a three-stage process (see figure 49): the NP first adsorbed at the membrane surface (stage 1), then the NP partially inserted into the bilayer core establishing a hydrophobic contact between its hydrophobic moieties and lipid tails (stage 2), eventually one or more ligands translocated the bilayer core to reach the distal leaflet of the membrane, opposite to the insertion leaflet (stage 3).
In the first stage of the interaction the NP approaches the membrane surface and adsorbs on the head region. Before moving towards the second stage, the NP spends several microseconds in the adsorbed state. The stability of this configuration depends on the configuration of the ligands on the NP: the random NP detached frequently from the membrane, while no detachment events were observed for the striped NP, as shown in figure 50.

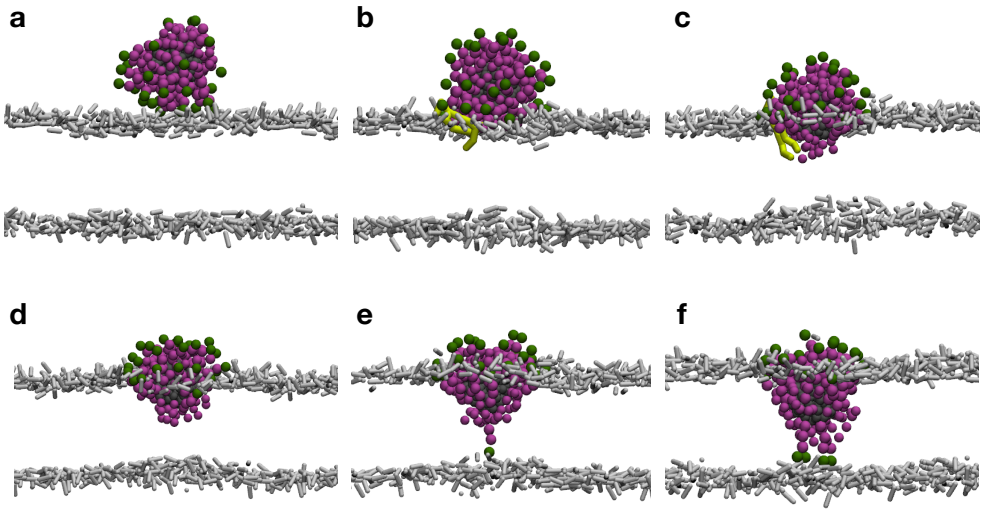

Figure 49: Sequence of the NP–membrane interaction process for the random nanoparticle. a. The nanoparticle adsorbs at the membrane surface (stage 1). b-d. One lipid (yellow) protrude towards the water phase and adheres to the hydrophobic moieties of the nanoparticle which is subsequently pulled towards the core of the membrane (stage 2). e,f. Finally, more and more ligands translocate the interior of the membrane to reach the distal leaflet (stage 3). NP core in grey, hydrophobic moieties of both anionic and hydrophobic ligands in purple, charged termini of the anionic ligands in green. Lipid heads are shown as light-grey sticks, while lipid tails, which fill the region between the head groups, are not shown for clarity. Water beads, which are not shown, feel the box around the nanoparticle and the membrane.

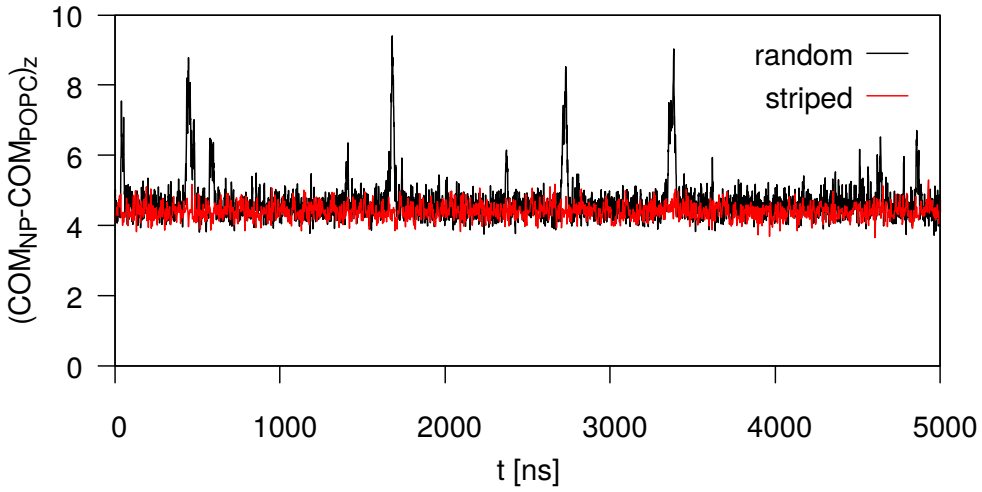

Figure 50: Distance between the centre of mass of the nanoparticle and the POPC membrane during the adsorption stage. Only 5 μs are shown for two representative simulations.

The second stage of the interaction involves the formation of a hydrophobic contact between the hydrophobic moieties of the ligands on the NP and the hydrophobic tails of the membrane. The process is initiated by the protrusion of a lipid tail in the head region (see figure 49, b). This process, which we see through unbiased simulations, is the same mechanism observed by Van Lehn *et al.* [137] for highly curved membranes. The NP is then pulled towards the centre of the bilayer and more and more hydrophobic contacts are established.

An increasing number of contacts is also created by the charged termini of the anionic ligands and the charged lipid heads, as shown in figure 51.

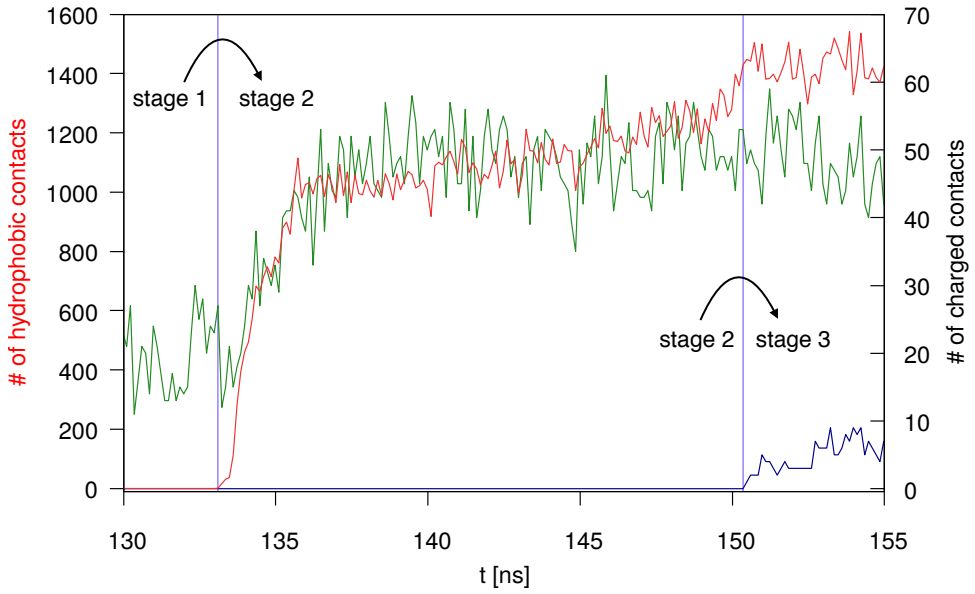

Figure 51: Number of contacts for both hydrophobic (red, left y axis) and charged (blue and green, right y axis) beads for the random nanoparticle. Charged contacts are computed between the negatively charged bead of the AN ligands and the choline bead of the lipid heads in the entrance (green) and distal (blue) leaflet. The two vertical lines represent the time at which the nanoparticle goes from stage 1 to stage 2 (left) and from stage 2 to stage 3 (right).

After the hydrophobic contact is established, one ligand (anchor) translocates the membrane interior to reach the distal leaflet of the membrane (see figure 49, e) followed by a second, a third and so on (panel f in figure 49), leading to the snorkelled configuration predicted by Van Lehn *et al.* [137] using thermodynamic models.

Ligand arrangement influences the thermodynamics of the NP–membrane interaction Before reaching stage 2, the NP spends, on average, several μs in stage 1, suggesting that a free energy barrier has to be overcome to go from stage 1 to stage 2: this free energy barrier corresponds to the protrusion of a lipid tail in the head region of the membrane and, according to our unbiased simulations, it is independent on ligand arrangement. As for the 2-3 transition a difference in the behaviour of the random and striped NPs emerged from unbiased simulations when looking at the time that elapses before the first anchor was dropped. As shown in figure 52, where the number of anchors is plotted as a function of the time since the hydrophobic contact was established, the random NP requires only a few nanoseconds to go from stage 2 to stage 3, conversely to the striped NP which resides in stage 2 for longer times (5 ns, 3.7 μs, 3.9 μs, 9.3 μs, > 10.8 μs). Different free energy barriers have thus to be overcome to make the transition from stage 2 to stage 3 for the random and striped NPs.
To be more quantitative we performed metadynamics simulations applying a bias potential to the distance between the charged bead of one AN ligand and the COM of the lipid membrane along the bilayer normal. Metadynamics simulations were run with the PLUMED plugin for GROMACS. Gaussian of

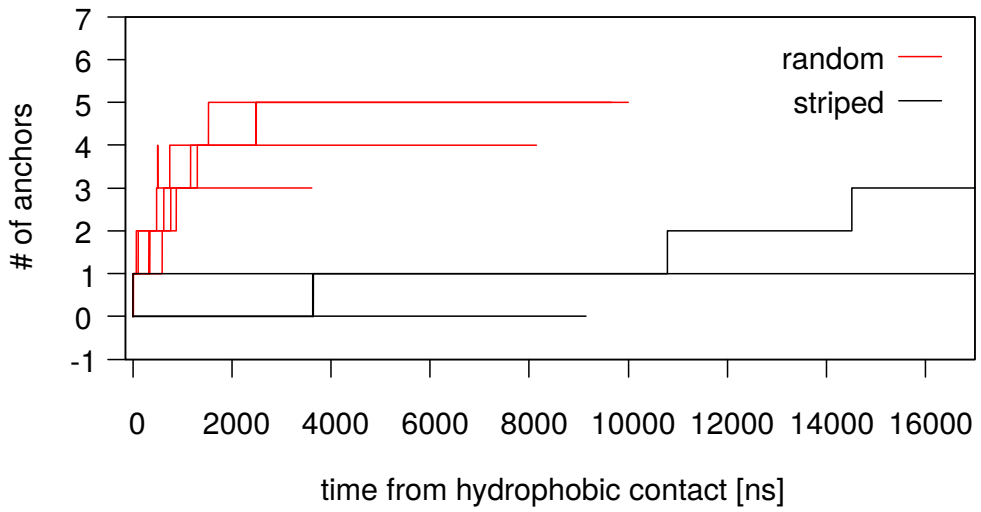

Figure 52: Number of anchors dropped by the random (red) and striped (black) nanoparticles. Different runs are shown for both nanoparticles with different lines. Time origin coincides with the establishment of the hydrophobic contact.

height and sigma 2.479 kJ/mol (about 1 k_BT) and 0.06 nm, respectively (for the meaning of these two parameters see section 2.3) were used to build the bias potential. All other parameters, temperature, pressure and so on were the same of unbiased simulations. The starting configuration of metadynamics simulations is shown in figure 53.

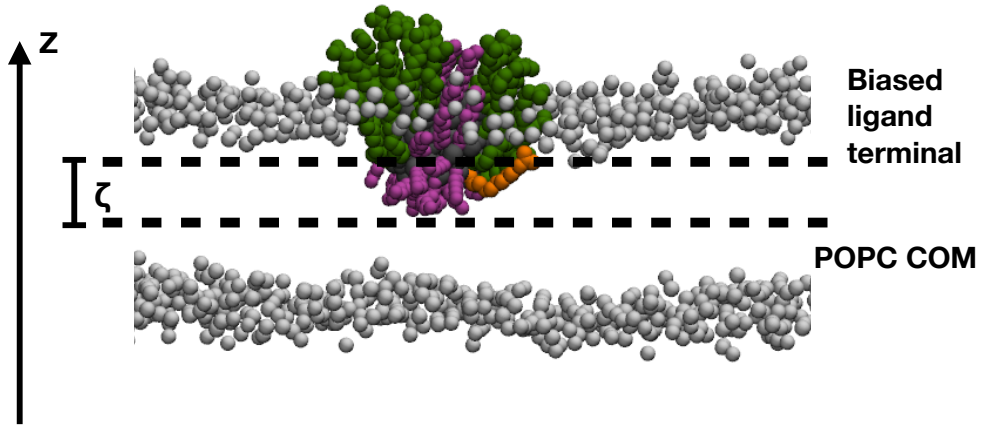

Figure 53: Initial configuration of metadynamics simulations. The reaction coordinate to which the bias potential is applied, ζ, is the distance along the z axis between the COM of the biased ligand, shown in orange, and the COM of the POPC membrane. The NP core is shown in grey, hydrophobic ligands in purple, charged ligands in green. For clarity, only the lipid heads of the POPC membrane are shown as white beads.

The resulting free energy profile for the striped NP, which is shown in figure 54, is made of two deep wells, the one on the right corresponding to the hydrophobic contact state, and the deeper on the left which corresponds to the anchored state. To complete the transition from stage 2 to stage 3, the striped NP has to overcome a free energy barrier of about 9 k_BT. The opposite transition, from stage 3 to stage 2, is hindered by a free energy

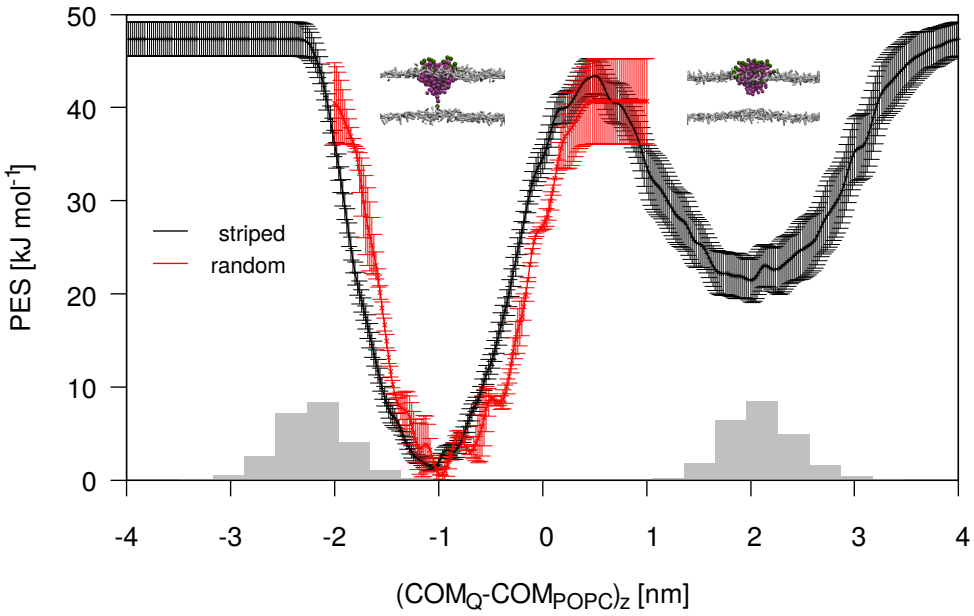

Figure 54: Free energy profile for the translocation of one charged ligand from the entrance to the distal leaflet of the lipid membrane. The distance along the bilayer normal between the COM of the charged bead of one ligand (COM_Q) and the COM of the membrane (COM_{POPC}) was used as collective variable. The black curves with its error bars refers to the striped nanoparticle, while the red curve with its error bars to the random nanoparticle. The histogram of lipid head positions is shown in grey. For the random nanoparticle only the transition from stage 3 to stage 2 could be sampled.

barrier of about 16 k_BT. Indeed, in our unbiased simulations we never observed ligand detachment events.
As for the random NP the reconstruction of the free energy profile is made difficult by the spontaneous translocation of other ligands during the sampling of the stage 2-to-stage 3 transition of the selected ligand. Thus, we could only make a qualitative analysis based on unbiased simulation which suggest a free energy barrier of translocation of a few k_BT. Sampling the transition from the anchored to the hydrophobic contact state (stage 3-to-stage 2 transition) let us estimate the dis-anchoring barrier which turned out to be similar to the one of the striped NP.

Anionic NPs can stably insert in a lipid membrane, the kinetics of the interaction being influenced by ligand arrangement From our unbiased simulations we found that partially anionic NPs can penetrate in the core of a zwitterionic POPC membrane following a three-stage process which involves first the adsorption of the NP on the membrane, followed by the establishment of a hydrophobic contact with the core of the membrane and concluded by the anchoring of more and more ligands. This last process in particular is almost irreversible as demonstrated by our metadynamics calculation from which we derived a very high dis-anchoring barrier.
We demonstrated that the ligand arrangement of mixed-composition NP influence the kinetics of the process. In particular, for random NPs only two stable states exist: the one in which the NP is adsorbed at the membrane surface and the anchored state. The striped NP, instead, goes through an additional metastable state, corresponding to the formation of a stable

hydrophobic contact between the hydrophobic moieties of the NP and the hydrophobic core of the membrane. The difference in the kinetics of the transition from one state to another for the random and patched NPs could lead to different internalisation pathways if one takes into account the more crowded membrane environment in which other molecules, such as proteins, are present.

Ligand translocation is accompanied by lipid heads and water dragging towards the centre of the membrane The results described in the previous paragraphs were obtained with the standard version of the Martini model in which electrostatics is simply cut-offed. However, for our system, a correct treatment of electrostatic interactions and water polarisation effects is crucial since one of the NP–membrane interaction steps involves the translocation of a charged bead from the polar water phase to the hydrophobic tail region of the membrane. Thus, the ability of a force field to faithfully reproduce the behaviour of charged moieties in environments with different polarity is crucial to correctly sample the translocation process. It is known that coarse-grained force fields, like the standard Martini force field, can severely underestimate the height of the free energy barrier for membrane translocation of monovalent ions [103]. Thus, we tested the reliability of the Martini force field in reproducing the process of translocation of a ligand from the water phase through the bilayer hydrophobic core.
To study the anchoring transition, we performed both unbiased and metadynamics simulations at atomistic level, which were used as a target for the comparison of three versions of the Martini force field: the standard Martini (SM) which we used so far to investigate the NP–membrane interaction, the standard Martini with long range electrostatics (MPME) and the polarisable Martini (MPW), that is the Martini version of the force field including both long range electrostatics and water polarisability (see subsection 2.4.3). We considered only the striped NP since in our unbiased simulations with the standard Martini force field it showed the highest stability of the hydrophobic contact state, which is the starting point of the transition we want to characterise.
Conversely to the SM simulations, atomistic, MPME and MPW simulations did not show any spontaneous anchoring process during the simulated time. From these simulations we computed the average distance between the COM of the NP and the COM of the POPC membrane, d_z (z being the axis perpendicular to the bilayer plane), which is reported in table 7 for the different models. All distances computed along the z axis and obtained from coarse-grained simulations are rescaled for the ratio between the thickness of the membrane in the atomistic and coarse-grained simulations. The MPW

Table 7: Average distance between the COM of the NP and the COM of the POPC membrane.

	atomistic model	SM	MPME	MPW
d_z (nm)	1.708 ± 0.008	1.463 ± 0.002	1.554 ± 0.005	1.717 ± 0.002

model shows the best agreement with atomistic simulations, while a configuration with the NP deeper inserted in the membrane is favoured by the other Martini models.

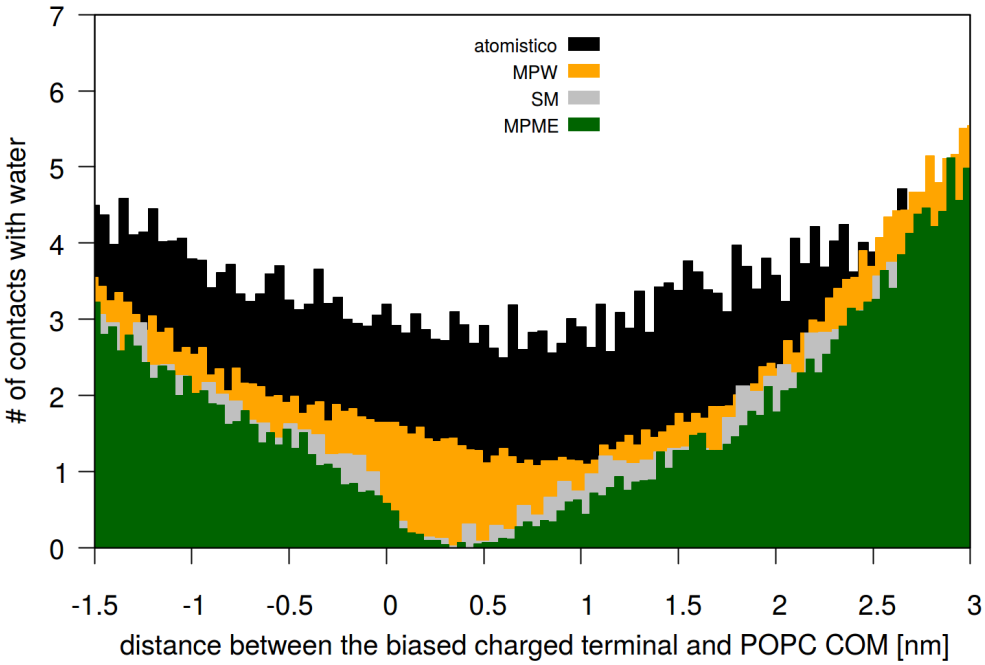

Figure 55: Number of contacts between the biased terminal group of a charged ligand and water. As for atomistic simulations the number of contacts was divided by 4 to account for the 4:1 mapping of the Martini force field.

Since no spontaneous translocation events occurred in unbiased simulations it was necessary to 'force' the transition from the hydrophobic to the anchored state using a bias potential along the reaction coordinate represented by the distance along the bilayer normal between the charged bead of one ligand and the COM of the POPC membrane (see figure 53 for the initial configuration setup). We sampled a complete transition event which involves the anchoring (forward transition) and the dis-anchoring (backward transition) of the biased ligand. From these simulations we observed that different behaviours were predicted by the four models: in the atomistic case the translocation of the ligand was accompanied by water dragging to the centre of the bilayer, as shown in figure 55, while among the coarse-grained models only the MPW could reproduce this feature, even if underestimating it. In fact, the number of contacts between water molecules and the terminal group of the biased ligand, shown in figure 55, is significantly smaller in MPW simulations while almost zero in SM and MPME simulations if the membrane core region is considered. Together with water molecules also lipid heads are dragged to the centre of the membrane in atomistic simulations. Even in this case, if one looks at the correlation between the time evolution of the collective variable and of the minimum distance of both water and choline groups from the COM of the membrane (see figure 56), only the MPW model is able to reproduce the atomistic behaviour. The dragging of water molecules and lipid heads when attempting the transition to the anchored state produces local membrane deformations, as it can be seen from figure 57.

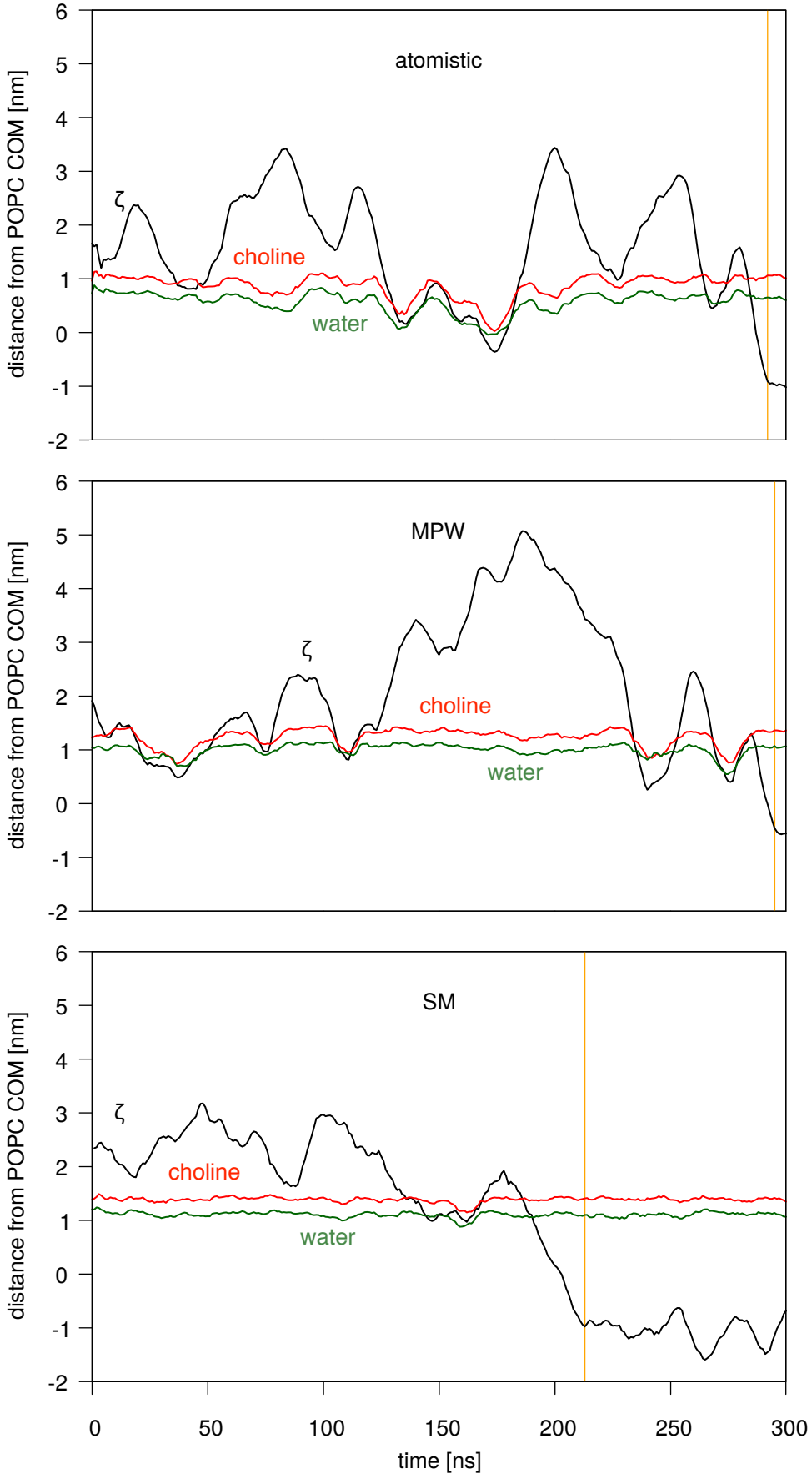

Figure 56: Time evolution of the collective variable ζ (in black) and of the minimum distance between either choline groups (in red) or water molecules (in green). The orange vertical line corresponds to the transition to the anchored state.

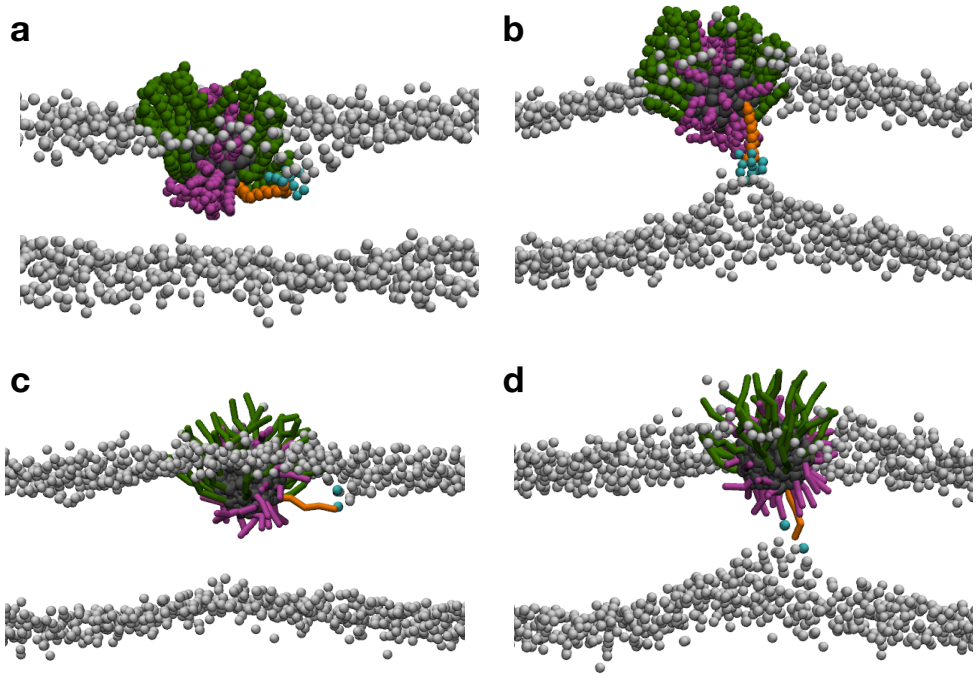

Figure 57: Dragging of lipid heads and water molecules towards the centre of the membrane for atomistic (a) and MPW model (c) simulations. When exploring the central region of the membrane the biased ligand induces large deformations of the membrane itself (b, atomistic; d, MPW model). Lipid heads in white, gold core in grey, anionic and hydrophobic ligands in green and purple, respectively. The charged biased ligand is coloured in orange, water molecules withing 0.6 nm of the charged ligand in cyan.

In one of our atomistic simulations we found that a water pore could be created to facilitate the translocation of the biased ligand from the entrance to the distal leaflet of the membrane, as shown in figure 58. Coherently with the absence of water-charged bead contacts at the membrane centre, no water pores could be formed in coarse-grained simulations with the SM and MPME models. Again, only the MPW model was able to partially reproduce atomistic results, with almost half of the forward transitions being accompanied by the translocation of one water bead together with the biased ligand.
Eventually, we computed the free energy barrier associated to the forward and backward transitions separately. We found that, at atomistic level, the forward barrier is much higher than that obtained with the SM model (see figure 59). For the forward barrier only the SM and MPW model have been compared, given the results of the forward barrier. The height of the forward and backward barriers in atomistic and coarse-grained simulations is summarised in table 8.

Table 8: Free energy barriers for the anchoring (forward) and dis-anchoring (backward) transition of a single charged ligand in atomistic and coarse-grained simulations.

	atomistic model	SM	MPME	MPW
ΔE_f (kJ/mol)	135 ± 10	26 ± 3	36 ± 5	100 ± 8
ΔE_b (kJ/mol)		38 ± 5		101 ± 7

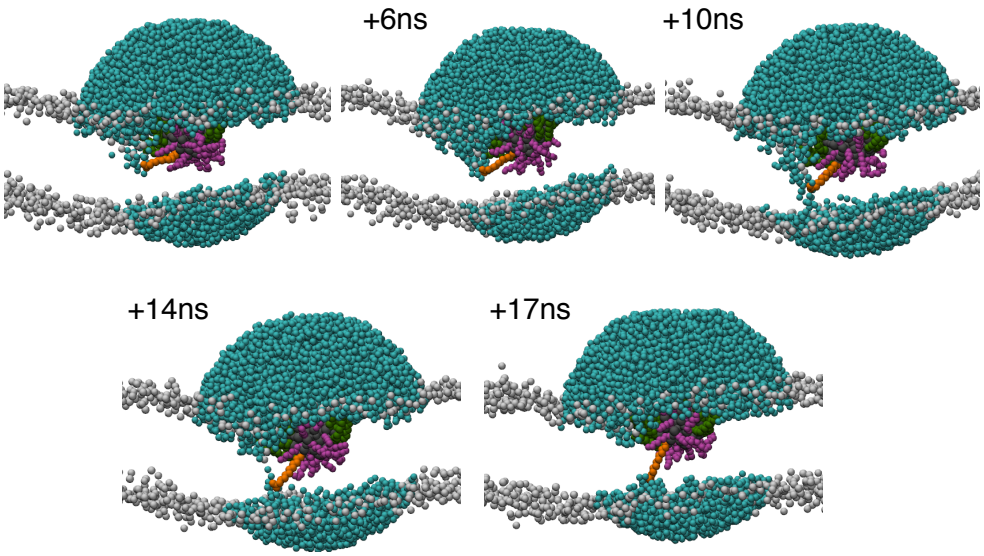

Figure 58: Sequence of ligand translocation accompanied by the formation of a water pore in one atomistic simulation. Lipid heads in white, NP core in grey, anionic ligands in green, hydrophobic ligands in purple. The biased ligand is shown in orange. Water molecules within 3.5 nm of the nanoparticle are shown in cyan.

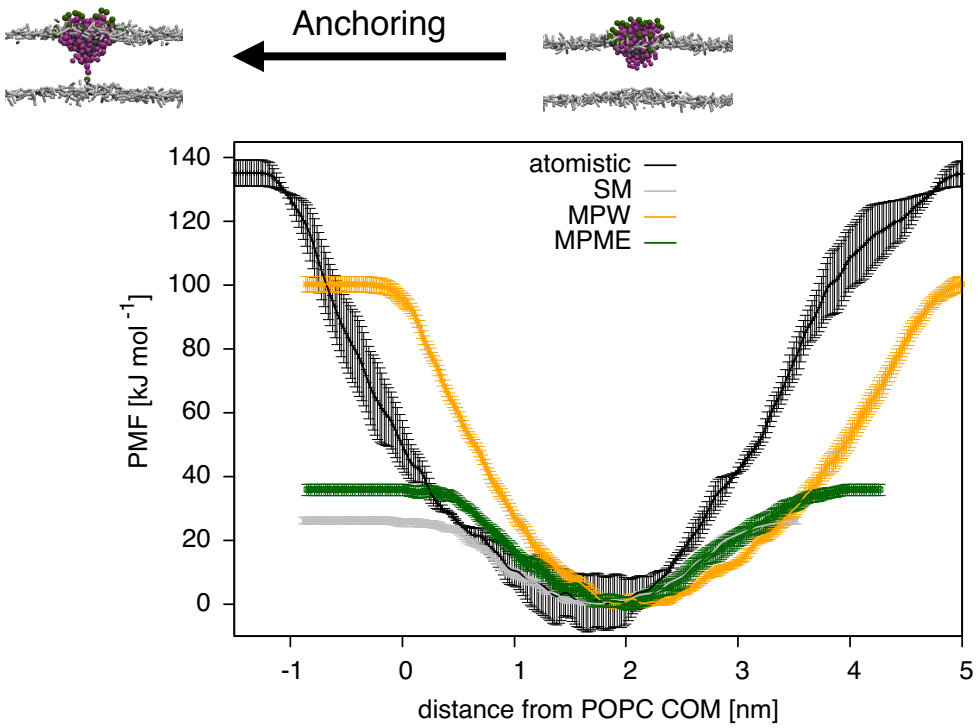

Figure 59: Potential of mean force for the forward transition (anchoring process). Error bars are standard errors and distances are rescaled to take into account the different thickness of the membrane in different models.

Long range electrostatics and water polarisability are necessary to faithfully describe the translocation of a charged ligand across a lipid membrane We compared the performances of three versions of the Martini force field, namely the standard version with both cut-offed and long range electrostatics and the polarisable version, in reproducing the processes and

free energy barriers for the translocation of a charged ligand of a monolayer-protected AuNP across the core of a neutral lipid bilayer. All three coarse-grained models are able to reproduce the key features of the hydrophobic contact configuration in which the NP stably resides in the entrance leaflet of the membrane. When looking at the anchoring process, only the polarisable version of the Martini force field is able to reproduce the mechanisms and the height of the free energy barrier associated we the process. In particular, the MPW model was able to reproduce the dragging of lipid heads and water molecules towards the centre of the membrane and the membrane deformations associated to the translocation of the charged ligand from one leaflet to the opposite of the lipid membrane, as predicted by atomistic simulations. Thus, if one is interested in preserving a good accuracy of the energetics of the process the polarisable model together with long range electrostatics should be used at the expense of a higher computational cost. However, if one is only interested in the interaction process, the standard Martini can be accurate enough and computationally more convenient.

6 ANIONIC AND CATIONIC NANOPARTICLES SHARE THE SAME INTERACTION MECHANISM WITH NEUTRAL LIPID MEMBRANES

Contents

In chapter 5 we showed that the NP characteristics can influence their interaction with model lipid membranes. In particular, we demonstrated that the ligand arrangement on the surface of gold NPs determines different kinetics of the NP-membrane interaction; this difference is sustained by free energy calculations which show how different free energy barriers for the same process are associated with different ligand arrangements.
In this chapter we deal with another aspect of surface functionalisation: the effect of NP charge on neutral lipid membranes. The role of charge in the interaction between NPs and both natural and model membranes has been investigated in many experimental systems [53, 130, 56] and with molecular dynamics simulations [138, 139]. The large variety in the systems that has been investigated makes it difficult to draw general conclusions about the effect of charge on the NP-membrane interaction. If, on the one hand, it seems clear that cationic NPs interact with negatively charged lipid membranes due to electrostatic attraction, on the other hand the behaviour of oppositely charged NPs on neutral bilayers is still unclear. While from liposome leakage assays anionic NPs seem to induce the largest damage to neutral lipid membranes [56] compared to cationic NPs, neutron reflectometry experiments show that anionic NPs could only adhere on the surface of a neutral lipid membrane [130] while cationic NPs could penetrate the bilayer. No disruptive effects were registered for anionic NPs interacting with neutral multilamellar liposomes [57].
We study the interaction of both anionic and cationic AuNPs with neutral POPC membranes through fluorescence leakage assays and molecular dynamics simulations. From our experiments we find that there is no difference in the interaction of anionic and cationic NPs with zwitterionic POPC vesicles. We sustain these results with biased molecular dynamics simulations which show that the free energy barrier to translocate one charged ligand, either positively or negatively charged, through the hydrophobic core of a POPC membrane is the same for anionic and cationic NPs.

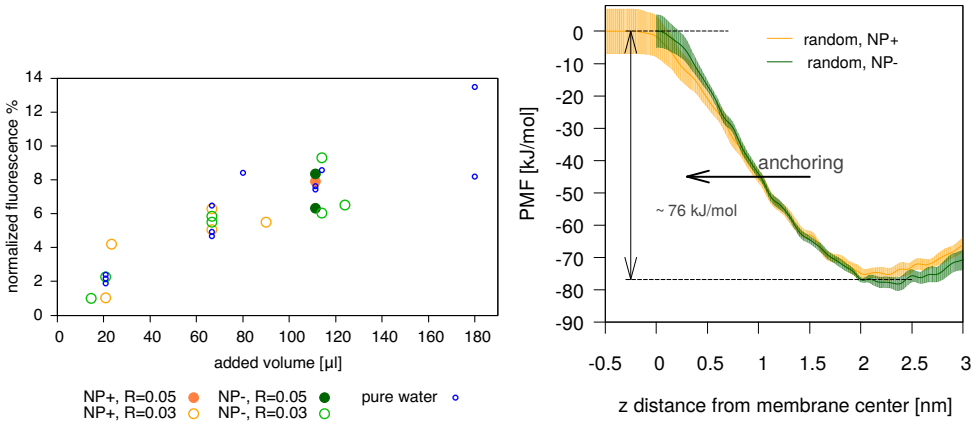

6.1 Liposomes as a model for cells

To study at a very fundamental level the interaction between NPs and cell membranes, simplified model systems should be considered. As seen in chapter 5 cell membranes are very crowded objects which can be modelled as a lipid matrix in which proteins are embedded. Since we are interested in studying the fundamental aspects of the NP-membrane interaction, we consider an even simpler model of membrane made only of lipids, and in particular POPC. In chapter 5 we described molecular dynamics simulations in which planar lipid membranes were used as a model for cell membranes. The main reason to chose planar bilayers resides in the higher computational cost associated to the simulation of lipid vesicles, if one is interested in reproducing cell shape.
From the experimental point of view one of the possible ways to probe the interaction between objects like NPs and lipid membranes is to use leakage assays from lipid vesicles, or liposomes. These structures have a spherical shape which self-assemble for hydrophobic effect when lipid films are dissolved in water. The lipid membrane thus separates the internal from the external aqueous environments (see figure 60).

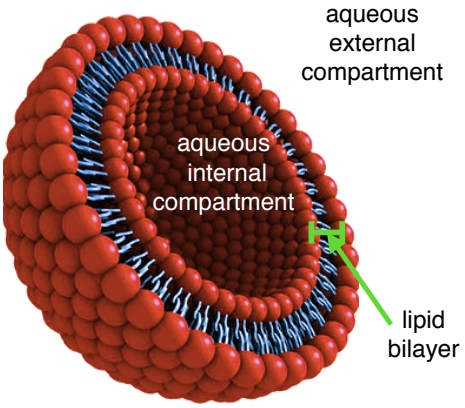

Figure 60: Schematic picture of a liposome made of amphiphilic lipids. The lipid bilayer divides the interior from the exterior aqueous environment.

Since the bilayer core is apolar, charged or polar compounds cannot penetrate from the exterior to the interior of the vesicle and *viceversa*. Thus, the only way to let molecules or larger objects pass through the lipid membrane is to locally and temporary perturb the membrane itself; this is the basic principle of leakage assays: molecules to which the lipid membrane of

liposomes is impermeable are usually loaded in the interior of the liposome and their leakage upon interaction with the objects to be studied is monitored. Exploiting their characteristic compartmentalisation, liposomes can be used not only as model systems for cell but also they can be employed in biomedicine as drug delivery systems.
Different methods can be used to prepare lipid vesicles, depending on the size and lipid components of liposomes, the molecules to be encapsulated and the dispersion medium.
Liposomes can be synthesised with diameter in the range 20 nm to 1 μm; if concentric membranes can be found inside the outer structure, liposomes are said to be multilamellar. In this case it is preferable to have membrane composed by a mixture of charged and neutral lipids so that electrostatic repulsion can stabilise multilamellar vesicles.

6.2 Experimental system

In this section we describe the methods that have been employed to prepare both liposomes and NPs. Only the preparation of liposomes is object of this thesis while NP preparation and characterisation were carried out by Ester Canepa at the premises of the Chemistry Department of the University of Genoa. Here we report only the key steps of NP synthesis and their key properties.

Synthesis and characterisation of gold nanoparticles Anionic and cationic NPs were prepared using the one-phase synthesis procedure [136]: with this method a solution of gold chloride ($HAuCl_4$) hydrophobic (OT) and either cationic (N,N,N-trymethylammonium bromide, TMA) or anionic (mercaptoundecanoic sulfonate, MUS) ligands is prepared and subsequently the reducing agent ($NaBH_4$) is added dropwise. The advantage of this technique is the good control on the ratio between different ligands: the ligand shell composition typically matches the stoichiometric ratio of ligands used in the syntheis. NP with a 1:1 mixture of hydrophobic and either anionic (NP-) or cationic (NP+) ligands and diameters smaller than 10 nm were synthesised (see figure 61 for a FESEM image of the NPs).

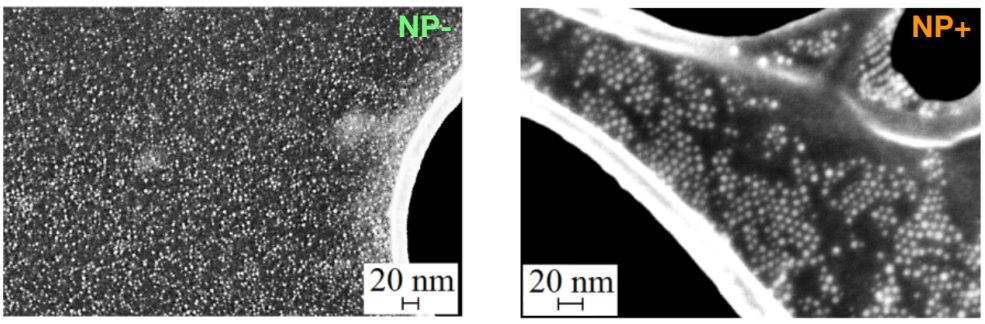

Figure 61: FESEM images of the anionic (left) and cationic (right) nanoparticles.

Synthesis and characterisation of POPC liposomes To perform leakage experiments we employed POPC liposomes loaded with the fluorescent dye calcein: this molecule, whose structure is shown in figure 62 together with its excitation and emission spectrum, is excited at a wavelength

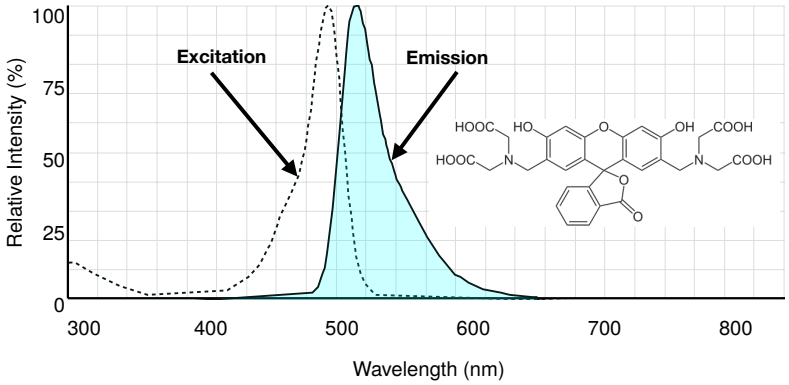

Figure 62: Excitation (dashed) and emission (solid) spectra of calcein. The excitation wavelength is 495 nm while the emission peak occurs at 515 nm. The chemical structure of calcein is shown in the inset.

of 495 nm and emits at a wavelength of 515 nm. At physiological pH 7.4 it bears 4 negative charges located at the carboxyl groups. To perform fluorescence measurements calcein should be encapsulated in liposomes at a concentration above its self-quenching concentration: inside liposomes calcein does not emit fluorescence but, when calcein molecules are diluted due to leakage effects to the outer medium, fluorescence is recovered and leakage can be detected. The self-quenching of calcein occurs at a concentration of 70 mM.
Lyophilised POPC was dissolved in chloroform and subsequently gently dried under nitrogen to generate a homogeneous lipid film which was then put under vacuum for 24 hours in order to remove residual solvent. Liposomes were obtained hydrating the lipid film at a lipid concentration 1 mg/ml with a solution of either 175 or 80 mM calcein, 2 mM histine, 2mM TES. The pH of the solution was adjusted to 7.4. The liposomal dispersion was sonicated for 15 minutes at 25 ℃ under nitrogen with a probe-type sonicator. To remove large lipid aggregates and titanium impurities from the probe the solution was centrifuged for 10 minutes and the sonicated vesicles employed in the experiments were collected from the supernatant. The outer solution of calcein was removed from the sample using the minicolumn centrifugation technique [140]. Filtration columns (1x10 cm) were filled with Sephadex G-50 swollen in 2 mM histidine, 2 mM TES, 100 mM NaCl and 1 mM EDTA at pH 7.4. Columns were centrifuged for 1 minute to remove excess buffer, then aliquotes of 100 μl were added to each column and centrifuged to filter the non-encapsulated material. The concentration of liposomes after filtration was determined by ^{1}H-NMR measurements following Hein *et al.* [141].
Liposomes were characterised using dynamic light scattering and ζ-potential measurements in the same buffer used for leakage experiments: the vesicles had a diameter of 23 $\pm$ 2 nm and ζ-potential of -5.5 $\pm$ 0.4 mV. The standard errors are derived from the Student's T-distribution at 95% confidence level interval.

6.3 Computational methods

In this section we describe the coarse-grained systems and simulation parameters that we use to support the experimental findings.

Simulations without calcein To test the effect of charge on the NP-membrane interaction we considered an anionic and a cationic NP with a 1:1 random arrangement of charged and hydrophobic ligands. The parameterisation of the ligands has been illustrated in section 3.2. We used unbiased MD simulations to probe the interaction mechanism of interaction for the cationic and anionic NPs. We considered the same setup built for the anionic NP illustrated in section 5.3: one NP, either cationic or anionic was put in a simulation box of volume 13x13x18 nm^3 in contact with the surface of a POPC bilayer and hydrated with about 18000 standard Martini water beads, salt at physiological concentration (NaCl 150 mM) and 30 counterions to neutralise the system.
Metadynamics simulations were performed to sample the free energy barrier associated to the translocation of a charged ligand through the membrane core (2-3 transition in the interaction mechanism described in section 5.3). Following the same setup of section 5.3 either the cationic or the anionic NPs in the hydrophobic contact configuration were hydrated with around 14000 polarisable water beads, salt at physiological concentration and 30 counterions to neutralise the simulation box. We chose the distance between one charged terminal bead and the COM of the membrane as collective variable. A Gaussian bias potential of σ 0.06 nm and height 2.479 kJ/mol was applied along the reaction coordinate.

Simulations with calcein To be consistent with the experimental setup we compartmentalised the simulation box to reproduce the internal volume of the liposomes. We developed a coarse-grained Martini model of the calcein dye. Its parameterisation is described in [142] and its structure is shown in figure 63.

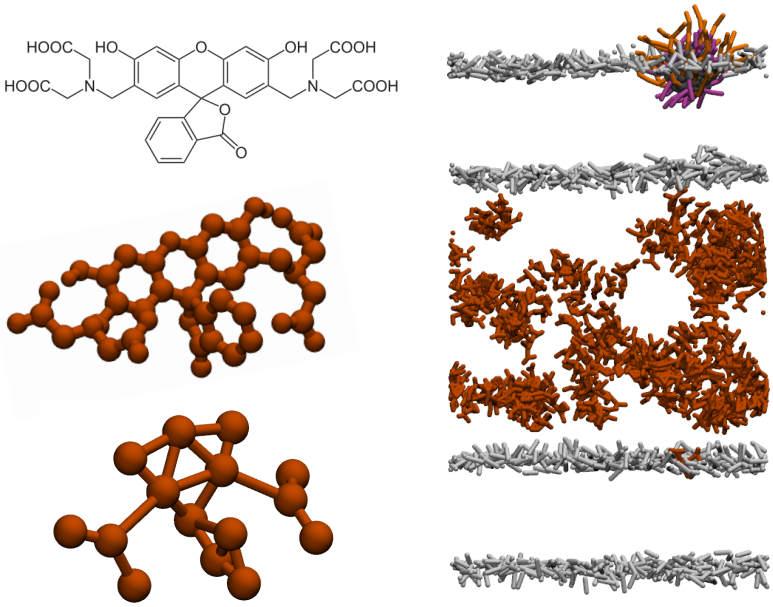

Figure 63: Left: atomistic (top) and Martini coarse-grained (bottom) model of calcein. Right: setup of metadynamics simulation performed with the compartmentalised system. The nanoparticle core is shown in grey, cationic ligands in orange, hydrophobic ligands in purple, lipid heads in white and calcein molecules in red. Water and lipid tails are not shown for clarity.

The simulation box, shown in figure 63, is divided into two regions by two identical POPC membranes: the region between the bilayers is filled with calcein at 175 mM, around 14000 polarisable water beads, salt at physiological concentration and 768 Na^+ ions to neutralise the four negative charges per calcein molecule; the outer region is filled with around 14000 polarisable water beads, salt at physiological concentration and 30 counterions to neutralise the box.
All simulations, both biased and unbiased, were performed at constant temperature (T = 310 k, velocity rescale thermostat with time constant τ = 2 ps) and constant pressure (p = 1 bar, semi-isotropic Parrinello-Rahman barostat with time constant τ = 12 ps and in-plane compressibility of $3x10^{-4}$ 1/bar). In unbiased simulations electrostatics was simply cut-offed and shifted while in metadynamics simulations with polarisable water the long range contribution of electrostatics was included with the PME method.

6.4 Experimental results

We performed leakage experiments from liposomes interacting either with anionic or cationic NPs. Measurements were performed at 25 ℃ at a lipid concentration of 0.035 mM inserted in a solution volume of 1.6 ml containing also 100 mM NaCl, 2 mM histidine, 2 mM TES and 0.1 mM EDTA at pH 7.4. The sample was excited at 490 nm and fluorescence emission was measured at 520 nm under continuous magnetic stirring. We observed a small increase in the fluorescence curve which reached a plateau in 30 minutes. This effect was reproducible and present only under stirring. We thus attribute this initial leakage to the interaction between the liposomes and the Teflon magnet, which was removed from the sample when no stirring was applied. The interaction experiments were then initiated only after the plateau was reached. Before being inserted in the liposome solutions, NPs were filtered using a 20 nm pore size filter in order to remove large particle aggregates, if present. The concentration of NPs after filtration was determined with UV/VIS absorption measurements. Either cationic or anionic NPs were added to the liposome solution in a NP/lipid weight ratio of 0.03. Calcein fluorescence was monitored as a function of time and normalised to its maximum obtained from liposome rupture which was achieved adding 0.5% (w/v) sodium cholate to the sample at the end of the experiment. A schematic picture of the experimental procedure is shown in figure 64.

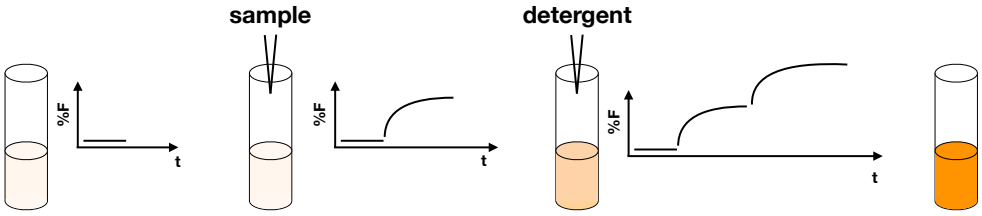

Figure 64: A schematic picture of a typical leakage experiment is shown. First, the solution of liposomes loaded with the fluorescent dye is prepared and the initial fluorescence is measured. Then the sample is added to the liposome solution and fluorescence is recorded again. Finally, a detergent is put in the sample and the fluorescence due to liposomes rupture is measured.

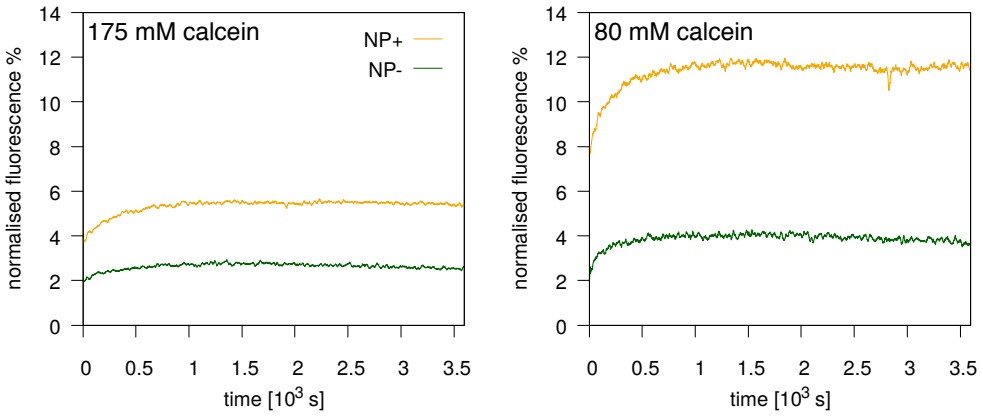

Figure 65: Fluorescence change in time upon interaction of either anionic (green) or cationic (orange) nanoparticles with the liposome solution. Two calcein concentrations, namely 175 (left) and 80 (right) mM, were tested.

The normalised fluorescence is computed as $(F - F_0)/(F_{max} - F_0)\%$. The results of two measurements at different calcein concentration are shown in figure 65.
We performed a set of experiments for each NP and compared the results with the ones obtained from analogous experiments in which only pure water was added to the liposome solution. Different volumes of water, among which those corresponding to the ones used for anionic and cationic NPs, were tested. The results of the experiments, mostly performed by Ester Canepa and Annalisa Relini, are summarised in figure 66.

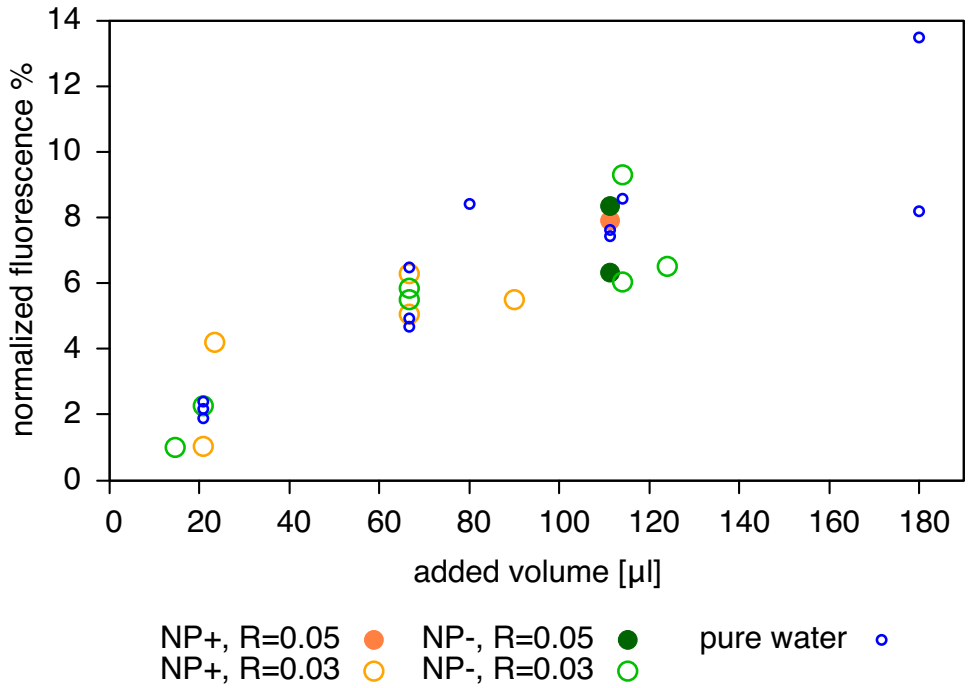

Figure 66: Fluorescence value at plateau as a function of the added volume of either nanoparticle solution or pure water. Orange points refer to measurements with cationic nanoparticles at a NP/lipid weight ratio, R, of 0.05 (filled) or R = 0.03 (empty). Green points represent measurements with anionic nanoparticles at R = 0.05 (filled) or R = 0.03 (empty). Blue points represent the measurements in which only water was added to the liposomes.

As it can be seen from the point distribution in figure 66, the equilibrium fluorescence leakage seems to be independent of the sign of the charge of the NPs and even independent on their presence. In fact, the points corresponding to the addition of NPs and those corresponding to pure water follow the same trend which seems to be dependent only on the volume of sample added to the liposome solution.

6.5 Simulation results

To sustain the experimental findings shown in the previous section, we performed biased MD simulations to compare the energetics of the interaction process between the anionic and cationic NPs with a zwitterionic POPC membrane.
As shown in section 5.3 the anchoring step is sensitive to different ligand arrangements and involve significant membrane deformations. We thus consider the same process to test if a difference in the behaviour of the cationic and anionic NP could be found. We performed metadynamics simulations in which one charged ligand was biased to accelerate the transition from the hydrophobic to the anchored state of the NP-membrane interaction (see chapter 5 for further details). We considered two different setups to mimic different concentrations of calcein: one in which calcein is absent which mimics the low concentration experiments, and one in which the calcein is present at 175 mM concentration in a compartment delimited by two lipid membranes (see figure 63).
At a visual inspection of biased MD simulations we observed that both anionic and cationic NPs induced large membrane deformations, as shown in figure 67, and in almost all simulations both NPs transferred at least one water bead during the biased ligand translocation.
More quantitatively, we computed the free energy barrier associated to the translocation process across the membrane core both in presence and absence of calcein. As shown in figure 68 no difference could be observed in the free energy barrier of translocation of a cationic and anionic ligand: for the negatively charged ligand a barrier of 76 ± 6 kJ/mol was measured while for the cationic NP the free energy barrier was 77 ± 5 kJ/mol in absence of calcein. The right panel of figure 68 shows that calcein has some effect on the free energy barrier of translocation but this effect is the same for both NPs. Both free energy barriers in fact were enlarged by about 10 kJ/mol. The effect of calcein is coherent with the difference that we observed in the equilibrium fluorescence for different calcein concentrations.

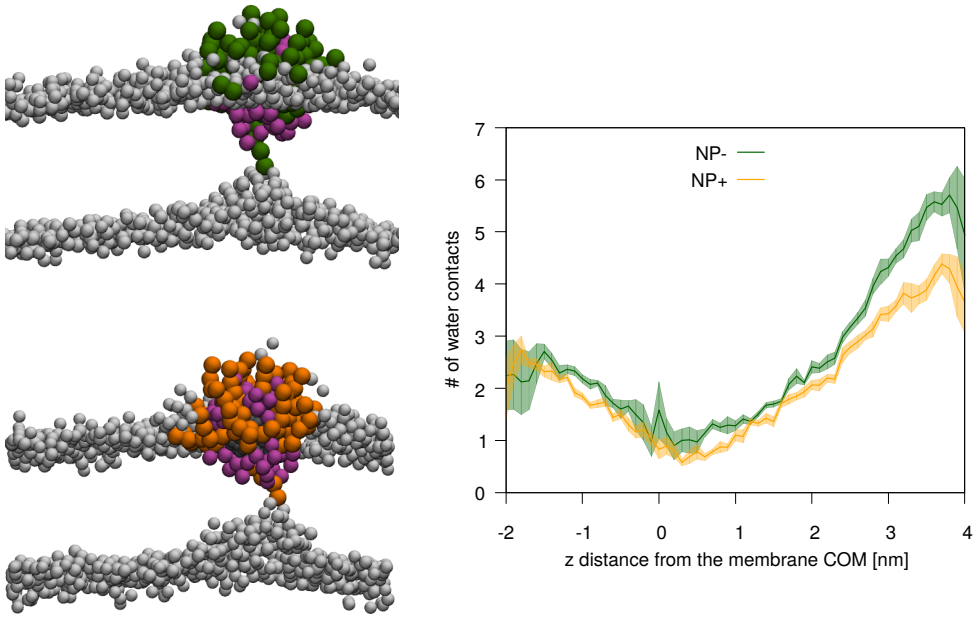

Figure 67: Left: deformation of the lipid membrane during the anchoring process for the anionic (top) and cationic (bottom) nanoparticle. Right: number of contacts between the terminal bead of the biased ligand and water beads for the anionic (green) and cationic (orange) nanoparticles. Nanoparticle core in black, anionic ligands in green, cationic ligands in orange, hydrophobic ligands in purple. Lipid heads are shown in white while lipid tails and water are not shown for clarity.

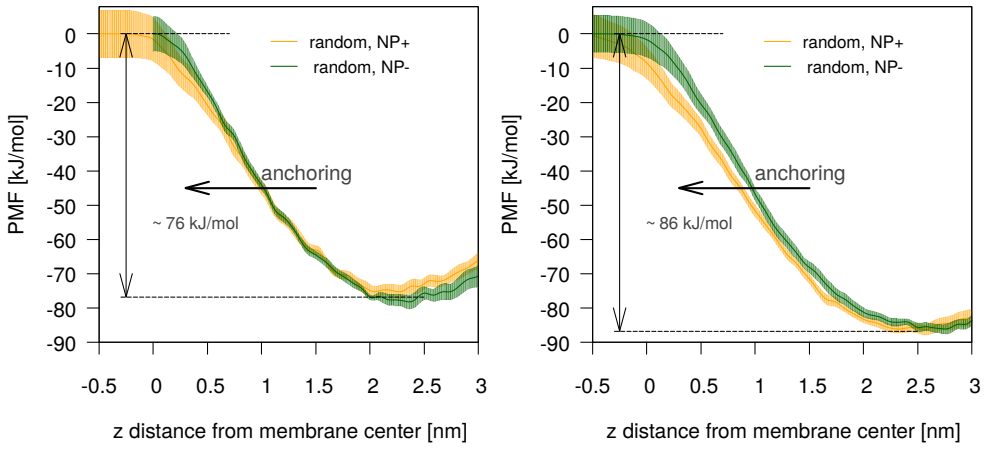

Figure 68: Free energy barrier for the translocation of one charged ligand through the lipid membrane core in absence (left) and presence (right) of calcein.

Charge does not influence the interaction of NPs with neutral lipid membranes We performed leakage experiments of the calcein fluorescent dye from zwitterionic POPC liposomes to study the influence of the charge of monolayer-protected gold NPs on their interaction with neutral zwitterionic lipid membranes. Our experiments show that charge does not lead to different behaviours in the interaction of NPs with liposomes. Moreover, from experiments in which only pure water was added to the liposome solution, we could see that the effect of NPs, independently on their charge, is negligible with respect to volume effects. We sustain these experimental evidence by means of molecular dynamics simulations. We show that the free energy

barrier associated to the translocation of one charged ligand across the hydrophobic core of the membrane is the same for both anionic and cationic NPs. We also observe that both NPs produce the same membrane deformations during the transitions which is almost always accompanied by water transport across the bilayer.

CONCLUSIONS

In thesis we investigated the behaviour of monolayer-protected gold nanoparticles with biomedical applications. In particular we studied, using both molecular dynamics simulations and experiments, the interaction of functionalised gold nanoparticles with proteins and model lipid membranes. These biological components are relevant for *in vivo* applications of nanoparticles. As shown in chapter 1 nanoparticles injected in the body have to circulate in the blood stream, a very crowded environment in which different biological compounds can be found, before being delivered to cells. Among the large variety of biomolecules dispersed in blood there are proteins: their importance is related to the possibility for proteins to form stable complexes with nanoparticles. If, on the one hand this complexation can make nanoparticles less toxic to the body, on the other hand their functionality may be altered and their circulation time in blood can be reduced.
Cells are the target of many biomedical applications as well as organelles inside cells. The first barrier that nanoparticles encounter when interacting with cells is the cell membrane: the high complexity of this biological system makes it non-trivial to study the interaction with nanoparticles. Thus, model membranes are considered, as illustrated in chapter 5.
In chapter 4 we studied the interaction of zwitterionic nanoparticles with albumin, the most abundant protein in human serum plasma, using molecular dynamics simulations. Among the possible molecules which can be used to functionalise gold nanoparticles we selected zwitterionic ligands since they proved to be efficient in reducing the adsorption of proteins. We chose two ligands differing only in the hydrophobic content of their zwitterionic terminal group. We demonstrated that the interplay of chemical and conformational properties of the ligands which functionalise the nanoparticles determines different interaction strength between albumin and zwitterionic nanoparticles. In particular, we showed that the higher hydrophobic content in the terminal group of the ligands determines the folding of the ligands themselves increasing the stability of the nanoparticle-protein complex. Ligands with lower hydrophobicity, instead did not fold and their interaction with albumin was weaker.

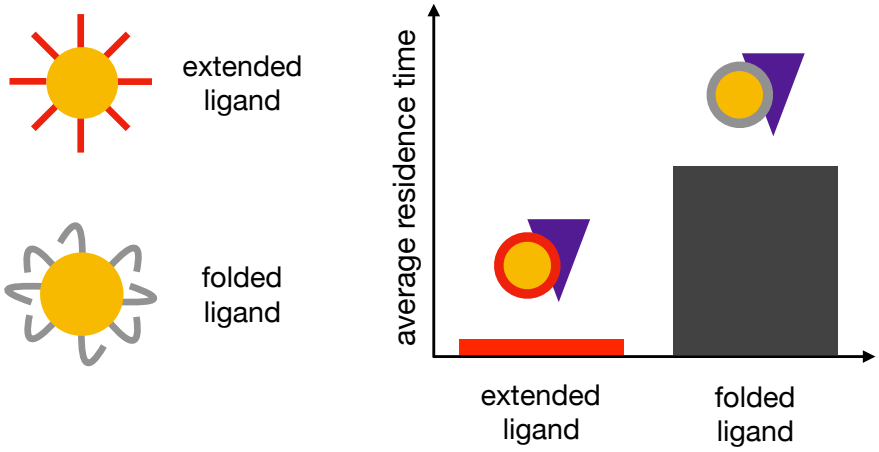

In chapter 5 we studied the interaction of functionalised gold nanoparticles with mono-component model lipid membranes. We used molecular dynamics simulations to elucidate the mechanism of interaction at a molecular level. We found that the interaction between a charged nanoparticle, functionalised with a mixture of charged and hydrophobic ligands, and a neutral lipid membrane develops in three stages: at first the nanoparticle approaches the lipid membrane surface and adsorbs on it; then the nanoparticle inserts into the membrane core and finally some of the charged ligands translocate across the membrane core. We investigated the effect of different patterns of ligands on the nanoparticle surface on the interaction with a lipid membrane. We found that the ligand pattern does not influence the mechanism of interaction but only its kinetics: patterned nanoparticles showed a lower kinetics with respect to nanoparticles with random ligand arrangement.

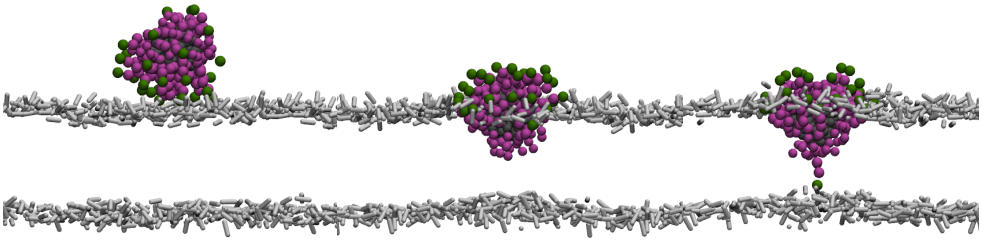

Finally, in chapter 6 we studied at both experimental and computational level the effect of the sign of the charge on the interaction between nanoparticles and neutral lipid membranes. We performed leakage experiments of a fluorescent dye encapsulated in neutral liposomes upon the interaction with a solution of particles of either positive or negative charge. We found that the sign of the charge does not influence the interaction of nanoparticles with the neutral membrane of liposomes, and that nanoparticles are not highly disruptive to the lipid membrane. We sustained this finding with molecular dynamics simulations which showed that functionalised nanoparticles, differing only in the charge of the ligands, share the same mechanism of interaction with and cause similar perturbation to a neutral lipid membrane.

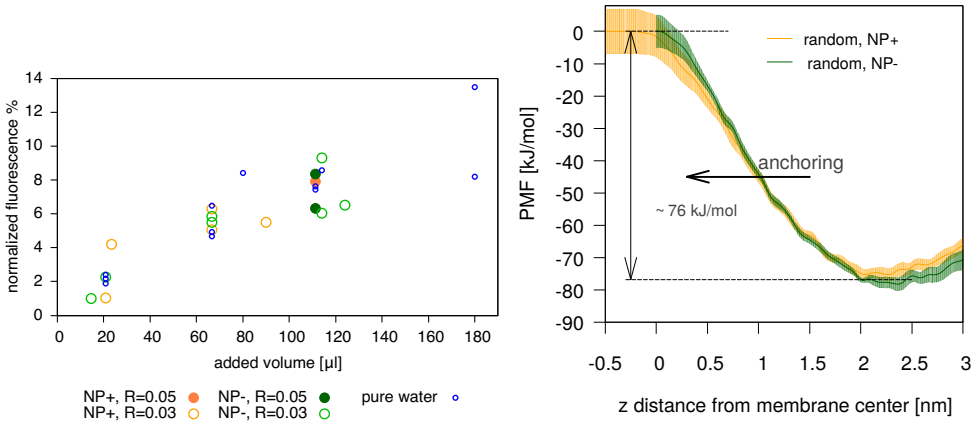

REFERENCES

[1] Xiaohua Huang et al. “Cancer Cell Imaging and Photothermal Therapy in the Near-Infrared Region by Using Gold Nanorods”. In: *Journal of the American Chemical Society* 128.6 (2006), pp. 2115–2120.

[2] Nathaniel L. Rosi and Chad A. Mirkin. “Nanostructures in Biodiagnostics”. In: *Chemical Reviews* 105.4 (2005), pp. 1547–1562.

[3] Ivan H. El-Sayed, Xiaohua Huang, and Mostafa A.El-Sayed. “Selective laser photo-thermal therapy of epithelial carcinoma using anti-EGFR antibody conjugated gold nanoparticles”. In: *Cancer Letters* 239.1 (2006), pp. 129–135.

[4] Karrina McNamara and Syed A. M. Tofail. “Nanoparticles in biomedical applications”. In: *Advances in Physics: X* 2.1 (2016), pp. 54–88.

[5] Jingyi Chen et al. “Gold Nanocages as Photothermal Transducers for Cancer Treatment”. In: *Small* 6.7 (2010), pp. 811–817.

[6] Lucia Babes et al. “Synthesis of Iron Oxide Nanoparticles Used as MRI Contrast Agents: A Parametric Study”. In: *Journal of Colloid and Interface Science* 212.2 (1999), pp. 474–482.

[7] A. Jordan et al. “Inductive heating of ferrimagnetic particles and magnetic fluids: Physical evaluation of their potential for hyperthermia”. In: *International Journal of Hyperthermia* 25.7 (2009), pp. 499–511.

[8] Q. A. Pankhurst et al. “Applications of magnetic nanoparticles in biomedicine”. In: 36.13 (2003), pp. 167–181.

[9] Ajay Kumar Gupta and Mona Gupta. “Synthesis and surface engineering of iron oxide nanoparticles for biomedical applications”. In: *Biomaterials* 26.18 (2005), pp. 3995–4021.

[10] Koichiro Hayashi et al. “Superparamagnetic Nanoparticle Clusters for Cancer Theranostics Combining Magnetic Resonance Imaging and Hyperthermia Treatment”. In: *Theranostics* 3.6 (2013), pp. 366–376.

[11] Ameer Azam et al. “Antimicrobial activity of metal oxide nanoparticles against Gram-positive and Gram-negative bacteria: a comparative study”. In: *International Journal of Nanomedicine* (2012), p. 6003.

[12] Tianyi Wang et al. “Potential application of functional porous TiO2 nanoparticles in light-controlled drug release and targeted drug delivery”. In: *Acta Biomaterialia* 13 (2015), pp. 354–363.

[13] Hong Yang et al. “One-pot synthesis of amphiphilic superparamagnetic FePt nanoparticles and magnetic resonance imaging in vitro”. In: *Journal of Magnetism and Magnetic Materials* 322.8 (2010), pp. 973–977.

[14] Hong Yang et al. “Monodisperse water-soluble Fe–Ni nanoparticles for magnetic resonance imaging”. In: *Journal of Alloys and Compounds* 509.4 (2011), pp. 1217–1221.

[15] Won Seok Seo et al. “FeCo/graphitic-shell nanocrystals as advanced magnetic-resonance-imaging and near-infrared agents”. In: *Nature Materials* 5.12 (2006), pp. 971–976.

[16] Mary J Cloninger. “Biological applications of dendrimers”. In: *Current Opinion in Chemical Biology* 6.6 (2002), pp. 742–748.

[17] Cameron C Lee et al. “Designing dendrimers for biological applications”. In: *Nature Biotechnology* 23.12 (2005), pp. 1517–1526.

[18] Vladimir Rozhkov, David Wilson, and Sergei Vinogradov. “Phosphorescent Pd Porphyrin-Dendrimers: Tuning Core Accessibility by Varying the Hydrophobicity of the Dendritic Matrix”. In: *Macromolecules* 35.6 (2002), pp. 1991–1993.

[19] Nguyen T.K. Thanh and Luke A.W. Green. “Functionalisation of nanoparticles for biomedical applications”. In: *Nano Today* 5.3 (2010), pp. 213–230.

[20] David F. Williams. “There is no such thing as a biocompatible material”. In: *Biomaterials* 35.38 (2014), pp. 10009–10014.

[21] S. Moein Moghimi, A. Christy Hunter, and J. Clifford Murray. “Long-circulating and target-specific nanoparticles: Theory to practice”. In: *Pharmacological Reviews* 53.2 (2001), pp. 283–318.

[22] Ameya R. Kirtane. “Strategies to improve plasma circulation of nanoparticles”. In: *Nirma University Journal of pharmaceutical sciences* 1.1 (2014), pp. 1–18.

[23] Mark J. Ernsting et al. “Factors controlling the pharmacokinetics, biodistribution and intratumoral penetration of nanoparticles”. In: *Journal of Controlled Release* 172.3 (2013), pp. 782–794.

[24] Saba Naqvi et al. “Concentration-dependent toxicity of iron oxide nanoparticles mediated by increased oxidative stress”. In: *International Journal of Nanomedicine* (2010), p. 983.

[25] Dhermendra K Tiwari, Takashi Jin, and J. Behari. “Dose-dependent in-vivo toxicity assessment of silver nanoparticle in Wistar rats”. In: *Toxicology Mechanisms and Methods* 21.1 (2010), pp. 13–24.

[26] Stefan Wilhelm et al. “Analysis of nanoparticle delivery to tumours”. In: *Nature Reviews Materials* 1.5 (2016).

[27] Xi He et al. “pH-sensitive drug-delivery systems for tumor targeting”. In: *Therapeutic Delivery* 4.12 (2013), pp. 1499–1510.

[28] Guanren Zhao et al. “Smart pH-sensitive nanoassemblies with cleavable PEGylation for tumor targeted drug delivery”. In: *Scientific Reports* 7.1 (2017).

[29] Barbara De Berardis et al. “Exposure to ZnO nanoparticles induces oxidative stress and cytotoxicity in human colon carcinoma cells”. In: *Toxicology and Applied Pharmacology* 246.3 (2010), pp. 116–127.

[30] Pascale R. Leroueil et al. “Wide Varieties of Cationic Nanoparticles Induce Defects in Supported Lipid Bilayers”. In: *Nano Letters* 8.2 (2008), pp. 420–424.

[31] Gevdeep Bhabra et al. “Nanoparticles can cause DNA damage across a cellular barrier”. In: *Nature Nanotechnology* 4.12 (2009), pp. 876–883.

[32] Haji Bahadar et al. “Toxicity of nanoparticles and an overview of current experimental models”. In: *Iranian Biomedical Journal* 20.1 (2016), pp. 1–11.

[33] Pablo del Pino et al. “Protein corona formation around nanoparticles – from the past to the future”. In: *Mater. Horiz.* 1.3 (2014), pp. 301–313.

[34] Iseult Lynch et al. “The nanoparticle-protein complex as a biological entity: a complex fluids and surface science challenge for the 21st century”. In: *Advances in Colloid and Interface Science* 134-135 (2007), pp. 167–174.

[35] L. Vroman. “Effect of Adsorbed Proteins on the Wettability of Hydrophilic and Hydrophobic Solids”. In: *Nature* 196.4853 (1962), pp. 476–477.

[36] Van Hong Nguyen and Beom-Jin Lee. “Protein corona: a new approach for nanomedicine design”. In: *International Journal of Nanomedicine* Volume 12 (2017), pp. 3137–3151.

[37] Morteza Mahmoudi, Mohammad A. Shokrgozar, and Shahed Behzadi. “Slight temperature changes affect protein affinity and cellular uptake/toxicity of nanoparticles”. In: *Nanoscale* 5.8 (2013), p. 3240.

[38] Morteza Mahmoudi et al. “Protein-Nanoparticle Interactions: Opportunities and Challenges”. In: *Chemical Reviews* 111.9 (2011), pp. 5610–5637.

[39] Claudia Corbo et al. “The impact of nanoparticle protein corona on cytotoxicity, immunotoxicity and target drug delivery”. In: *Nanomedicine* 11.1 (2016), pp. 81–100.

[40] Jung Soo Suk et al. “PEGylation as a strategy for improving nanoparticle-based drug and gene delivery”. In: *Advanced Drug Delivery Reviews* 99 (2016), pp. 28–51.

[41] R Gref et al. “‘Stealth’ corona-core nanoparticles surface modified by polyethylene glycol (PEG): influences of the corona (PEG chain length and surface density) and of the core composition on phagocytic uptake and plasma protein adsorption”. In: *Colloids and Surfaces B: Biointerfaces* 18.3-4 (2000), pp. 301–313.

[42] Takuro Niidome et al. “PEG-modified gold nanorods with a stealth character for in vivo applications”. In: *Journal of Controlled Release* 114.3 (2006), pp. 343–347.

[43] Jillian L. Perry et al. “PEGylated PRINT Nanoparticles: The Impact of PEG Density on Protein Binding, Macrophage Association, Biodistribution, and Pharmacokinetics”. In: *Nano Letters* 12.10 (2012), pp. 5304–5310.

[44] Shenfu Chen et al. “Surface hydration: Principles and applications toward low-fouling/nonfouling biomaterials”. In: *Polymer* 51.23 (2010), pp. 5283–5293.

[45] Hiromi Kitano et al. “Structure of Water Incorporated in Sulfobetaine Polymer Films as Studied by ATR-FTIR”. In: *Macromolecular Bioscience* 5.4 (2005), pp. 314–321.

[46] Daniel F. Moyano et al. “Fabrication of Corona-Free Nanoparticles with Tunable Hydrophobicity”. In: *ACS Nano* 8.7 (2014), pp. 6748–6755.

[47] S. E. A. Gratton et al. “The effect of particle design on cellular internalization pathways”. In: *Proceedings of the National Academy of Sciences* 105.33 (2008), pp. 11613–11618.

[48] Charlotte M. Beddoes, C. Patrick Case, and Wuge H. Briscoe. “Understanding nanoparticle cellular entry: A physicochemical perspective”. In: *Advances in Colloid and Interface Science* 218 (2015), pp. 48–68.

[49] Hong-ming Ding and Yu-qiang Ma. “Theoretical and Computational Investigations of Nanoparticle-Biomembrane Interactions in Cellular Delivery”. In: *Small* 11.9-10 (2014), pp. 1055–1071.

[50] B. Devika Chithrani, Arezou A. Ghazani, and Warren C. W. Chan. “Determining the Size and Shape Dependence of Gold Nanoparticle Uptake into Mammalian Cells”. In: *Nano Letters* 6.4 (2006), pp. 662–668.

[51] Hideya Nakamura and Satoru Watano. “Direct Permeation of Nanoparticles across Cell Membrane: A Review”. In: *KONA Powder and Particle Journal* 35.0 (2018), pp. 49–65.

[52] Julia Dausend et al. “Uptake Mechanism of Oppositely Charged Fluorescent Nanoparticles in HeLa Cells”. In: *Macromolecular Bioscience* 8.12 (2008), pp. 1135–1143.

[53] Oshrat Harush-Frenkel et al. “Targeting of nanoparticles to the clathrin-mediated endocytic pathway”. In: *Biochemical and Biophysical Research Communications* 353.1 (2007), pp. 26–32.

[54] Viktoriya Sokolova et al. “Mechanism of the uptake of cationic and anionic calcium phosphate nanoparticles by cells”. In: *Acta Biomaterialia* 9.7 (2013), pp. 7527–7535.

[55] Ying Jiang et al. “The Interplay of Size and Surface Functionality on the Cellular Uptake of Sub-10 nm Gold Nanoparticles”. In: *ACS Nano* 9.10 (2015), pp. 9986–9993.

[56] Catherine M. Goodman et al. “Toxicity of Gold Nanoparticles Functionalized with Cationic and Anionic Side Chains”. In: *Bioconjugate Chemistry* 15.4 (2004), pp. 897–900.

[57] Reid C. Van Lehn et al. “Effect of Particle Diameter and Surface Composition on the Spontaneous Fusion of Monolayer-Protected Gold Nanoparticles with Lipid Bilayers”. In: *Nano Letters* 13.9 (2013), pp. 4060–4067.

[58] Anuj Tiwari et al. “Passive membrane penetration by ZnO nanoparticles is driven by the interplay of electrostatic and phase boundary conditions”. In: *Nanoscale* 10.7 (2018), pp. 3369–3384.

[59] Alessandra Luchini et al. “Neutron Reflectometry reveals the interaction between functionalized SPIONs and the surface of lipid bilayers”. In: *Colloids and Surfaces B: Biointerfaces* 151 (2017), pp. 76–87.

[60] Federica Simonelli et al. “Monolayer-Protected Anionic Au Nanoparticles Walk into Lipid Membranes Step by Step”. In: *The Journal of Physical Chemistry Letters* 6.16 (2015), pp. 3175–3179.

[61] Reid C. Van Lehn and Alfredo Alexander-Katz. “Pathway for insertion of amphiphilic nanoparticles into defect-free lipid bilayers from atomistic molecular dynamics simulations”. In: *Soft Matter* 11.16 (2015), pp. 3165–3175.

[62] Dmitry Bedrov et al. “Passive Transport of C60Fullerenes through a Lipid Membrane: A Molecular Dynamics Simulation Study”. In: *The Journal of Physical Chemistry B* 112.7 (2008), pp. 2078–2084.

[63] Jirasak Wong-Ekkabut et al. “Computer simulation study of fullerene translocation through lipid membranes”. In: *Nature Nanotechnology* 3.6 (2008), pp. 363–368.

[64] Erik C. Dreaden et al. “The golden age: gold nanoparticles for biomedicine”. In: *Chem. Soc. Rev.* 41.7 (2012), pp. 2740–2779.

[65] Lev Dykman and Nikolai Khlebtsov. “Gold nanoparticles in biomedical applications: recent advances and perspectives”. In: *Chem. Soc. Rev.* 41.6 (2012), pp. 2256–2282.

[66] P Ghosh et al. “Gold nanoparticles in delivery applications”. In: *Advanced Drug Delivery Reviews* 60.11 (2008), pp. 1307–1315.

[67] Oren M. Becker et al. *Computational Biochemistry and Biophysics*. CRC Press, 2001.

[68] M. P. Allen and D. J. Tildesley. *Computer Simulation of Liquids (Oxford Science Publications)*. Clarendon Press, 1989.

[69] Daan Frenkel and Berend Smit. *Understanding Molecular Simulation: From Algorithms to Applications (Computational Science Series, Vol 1)*. Academic Press, 2001.

[70] Loup Verlet. “Computer "Experiments" on Classical Fluids. I. Thermodynamical Properties of Lennard-Jones Molecules”. In: *Physical Review* 159.1 (1967), pp. 98–103.

[71] R.W. Hockney. “Potential calculations and some applications.” In: *Methods Comput. Phys.* 9 (1970), pp. 135–211.

[72] William C. Swope et al. “A computer simulation method for the calculation of equilibrium constants for the formation of physical clusters of molecules: Application to small water clusters”. In: *The Journal of Chemical Physics* 76.1 (1982), pp. 637–649.

[73] Giovanni Bussi, Davide Donadio, and Michele Parrinello. “Canonical sampling through velocity rescaling”. In: *The Journal of Chemical Physics* 126.1 (2007), p. 014101.

[74] H. J. C. Berendsen et al. “Molecular dynamics with coupling to an external bath”. In: *The Journal of Chemical Physics* 81.8 (1984), pp. 3684–3690.

[75] M. Parrinello and A. Rahman. “Polymorphic transitions in single crystals: A new molecular dynamics method”. In: *Journal of Applied Physics* 52.12 (1981), pp. 7182–7190.

[76] A. Laio and M. Parrinello. “Escaping free-energy minima”. In: *Proceedings of the National Academy of Sciences* 99.20 (2002), pp. 12562–12566.

[77] Abby L. Parrill and Kenny B. Lipkowitz, eds. *Reviews in Computational Chemistry Volume 28*. John Wiley & Sons, Inc, 2015.

[78] Alessandro Laio and Francesco L Gervasio. “Metadynamics: a method to simulate rare events and reconstruct the free energy in biophysics, chemistry and material science”. In: *Reports on Progress in Physics* 71.12 (2008), p. 126601.

[79] Tom Darden, Darrin York, and Lee Pedersen. “Particle mesh Ewald: An N·log(N) method for Ewald sums in large systems”. In: *The Journal of Chemical Physics* 98.12 (1993), pp. 10089–10092.

[80] Ulrich Essmann et al. “A smooth particle mesh Ewald method”. In: *The Journal of Chemical Physics* 103.19 (1995), pp. 8577–8593.

[81] P. P. Ewald. “Die Berechnung optischer und elektrostatischer Gitterpotentiale”. In: *Annalen der Physik* 369.3 (1921), pp. 253–287.

[82] Haibo Yu and Wilfred F. van Gunsteren. “Accounting for polarization in molecular simulation”. In: *Computer Physics Communications* 172.2 (2005), pp. 69–85.

[83] Kresten Lindorff-Larsen et al. “Improved side-chain torsion potentials for the Amber ff99SB protein force field”. In: *Proteins: Structure, Function, and Bioinformatics* (2010), pp. 1950–1958.

[84] William L. Jorgensen, Jeffry D. Madura, and Carol J. Swenson. “Optimized intermolecular potential functions for liquid hydrocarbons”. In: *Journal of the American Chemical Society* 106.22 (1984), pp. 6638–6646.

[85] William L. Jorgensen and Julian Tirado-Rives. “The OPLS [optimized potentials for liquid simulations] potential functions for proteins, energy minimizations for crystals of cyclic peptides and crambin”. In: *Journal of the American Chemical Society* 110.6 (1988), pp. 1657–1666.

[86] O. Berger, O. Edholm, and F. Jähnig. “Molecular dynamics simulations of a fluid bilayer of dipalmitoylphosphatidylcholine at full hydration, constant pressure, and constant temperature”. In: *Biophysical Journal* 72.5 (1997), pp. 2002–2013.

[87] D Peter Tieleman et al. “Membrane protein simulations with a united-atom lipid and all-atom protein model: lipid–protein interactions, side chain transfer free energies and model proteins”. In: *Journal of Physics: Condensed Matter* 18.28 (2006), S1221–S1234.

[88] H. J. C. Berendsen et al. “Interaction Models for Water in Relation to Protein Hydration”. In: *The Jerusalem Symposia on Quantum Chemistry and Biochemistry*. Springer Netherlands, 1981, pp. 331–342.

[89] H. J. C. Berendsen, J. R. Grigera, and T. P. Straatsma. “The missing term in effective pair potentials”. In: *The Journal of Physical Chemistry* 91.24 (1987), pp. 6269–6271.

[90] William L. Jorgensen et al. “Comparison of simple potential functions for simulating liquid water”. In: *The Journal of Chemical Physics* 79.2 (1983), pp. 926–935.

[91] William L. Jorgensen and Jeffry D. Madura. “Temperature and size dependence for Monte Carlo simulations of TIP4P water”. In: *Molecular Physics* 56.6 (1985), pp. 1381–1392.

[92] Siewert J. Marrink et al. “The MARTINI Force Field: Coarse Grained Model for Biomolecular Simulations”. In: *The Journal of Physical Chemistry B* 111.27 (2007), pp. 7812–7824.

[93] Djurre H. de Jong et al. “Improved Parameters for the Martini Coarse-Grained Protein Force Field”. In: *Journal of Chemical Theory and Computation* 9.1 (2012), pp. 687–697.

[94] Luca Monticelli et al. “The MARTINI Coarse-Grained Force Field: Extension to Proteins”. In: *Journal of Chemical Theory and Computation* 4.5 (2008), pp. 819–834.

[95] Xavier Periole et al. “Combining an Elastic Network With a Coarse-Grained Molecular Force Field: Structure, Dynamics, and Intermolecular Recognition”. In: *Journal of Chemical Theory and Computation* 5.9 (2009), pp. 2531–2543.

[96] Cesar A. López, Alex H. de Vries, and Siewert J. Marrink. “Computational microscopy of cyclodextrin mediated cholesterol extraction from lipid model membranes”. In: *Scientific Reports* 3.1 (2013).

[97] Hwankyu Lee and Ronald G. Larson. “Coarse-Grained Molecular Dynamics Studies of the Concentration and Size Dependence of Fifth- and Seventh-Generation PAMAM Dendrimers on Pore Formation in DMPC Bilayer”. In: *The Journal of Physical Chemistry B* 112.26 (2008), pp. 7778–7784.

[98] Emanuele Panizon et al. “MARTINI Coarse-Grained Models of Polyethylene and Polypropylene”. In: *The Journal of Physical Chemistry B* 119.25 (2015), pp. 8209–8216.

[99] Giulia Rossi et al. “Coarse-graining polymers with the MARTINI force-field: polystyrene as a benchmark case”. In: *Soft Matter* 7.2 (2011), pp. 698–708.

[100] Jaakko J. Uusitalo et al. “Martini Coarse-Grained Force Field: Extension to DNA”. In: *Journal of Chemical Theory and Computation* 11.8 (2015), pp. 3932–3945.

[101] Jaakko J. Uusitalo et al. “Martini Coarse-Grained Force Field: Extension to RNA”. In: *Biophysical Journal* 113.2 (2017), pp. 246–256.

[102] Siewert J. Marrink and D. Peter Tieleman. “Perspective on the Martini model”. In: *Chemical Society Reviews* 42.16 (2013), p. 6801.

[103] Semen O. Yesylevskyy et al. “Polarizable Water Model for the Coarse-Grained MARTINI Force Field”. In: *PLoS Computational Biology* 6.6 (2010). Ed. by Michael Levitt, e1000810.

[104] Julian Michalowsky et al. “A refined polarizable water model for the coarse-grained MARTINI force field with long-range electrostatic interactions”. In: *The Journal of Chemical Physics* 146.5 (2017), p. 054501.

[105] H BEKKER et al. “GROMACS - A PARALLEL COMPUTER FOR MOLECULAR-DYNAMICS SIMULATIONS”. In: *PHYSICS COMPUTING ’92*. Ed. by RA DeGroot and J Nadrchal. World Scientific Publishing, 1993, pp. 252–256.

[106] Gareth A. Tribello et al. “PLUMED 2: New feathers for an old bird”. In: *Computer Physics Communications* 185.2 (2014), pp. 604–613.

[107] Hannu Häkkinen. “The gold–sulfur interface at the nanoscale”. In: *Nature Chemistry* 4.6 (2012), pp. 443–455.

[108] Mathias Brust et al. “Synthesis of thiol-derivatised gold nanoparticles in a two-phase Liquid–Liquid system”. In: *J. Chem. Soc., Chem. Commun.* 0.7 (1994), pp. 801–802.

[109] Olga Lopez-Acevedo et al. “Structure and Bonding in the Ubiquitous Icosahedral Metallic Gold Cluster Au144(SR)60”. In: *The Journal of Physical Chemistry C* 113.13 (2009), pp. 5035–5038.

[110] Murray S. Daw and M. I. Baskes. “Semiempirical, Quantum Mechanical Calculation of Hydrogen Embrittlement in Metals”. In: *Physical Review Letters* 50.17 (1983), pp. 1285–1288.

[111] A. P. Sutton and J. Chen. “Long-range Finnis–Sinclair potentials”. In: *Philosophical Magazine Letters* 61.3 (1990), pp. 139–146.

[112] Raju P. Gupta. “Lattice relaxation at a metal surface”. In: *Physical Review B* 23.12 (1981), pp. 6265–6270.

[113] Fabrizio Cleri and Vittorio Rosato. “Tight-binding potentials for transition metals and alloys”. In: *Physical Review B* 48.1 (1993), pp. 22–33.

[114] Joseph Hautman and Michael L. Klein. “Simulation of a monolayer of alkyl thiol chains”. In: *The Journal of Chemical Physics* 91.8 (1989), pp. 4994–5001.

[115] Scott J. Weiner et al. “A new force field for molecular mechanical simulation of nucleic acids and proteins”. In: *Journal of the American Chemical Society* 106.3 (1984), pp. 765–784.

[116] Hendrik Heinz et al. “Accurate Simulation of Surfaces and Interfaces of Face-Centered Cubic Metals Using 12-6 and 9-6 Lennard-Jones Potentials”. In: *The Journal of Physical Chemistry C* 112.44 (2008), pp. 17281–17290.

[117] Elena Heikkilä et al. “Atomistic Simulations of Functional Au144(SR)60 Gold Nanoparticles in Aqueous Environment”. In: *The Journal of Physical Chemistry C* 116.17 (2012), pp. 9805–9815.

[118] Hwankyu Lee and Richard W. Pastor. “Coarse-Grained Model for PEGylated Lipids: Effect of PEGylation on the Size and Shape of Self-Assembled Structures”. In: *The Journal of Physical Chemistry B* 115.24 (2011), pp. 7830–7837.

[119] G. Rossi et al. “A Coarse-Grained MARTINI Model of Polyethylene Glycol and of Polyoxyethylene Alkyl Ether Surfactants”. In: *The Journal of Physical Chemistry B* 116.49 (2012), pp. 14353–14362.

[120] Monica Bulacu et al. “Improved Angle Potentials for Coarse-Grained Molecular Dynamics Simulations”. In: *Journal of Chemical Theory and Computation* 9.8 (2013), pp. 3282–3292.

[121] Ahmadreza F. Ghobadi et al. “Dispersing Zwitterions into Comb Polymers for Nonviral Transfection: Experiments and Molecular Simulation”. In: *Biomacromolecules* 17.2 (2016), pp. 546–557.

[122] J. M. Berg, J. L. Tymoczko, and L. Stryer. *Biochemistry*. New York, N.Y : W.H. Freeman and Company., 2012.

[123] Fabian Grunewald et al. “Transferable MARTINI Model of Poly(ethylene Oxide)”. In: *The Journal of Physical Chemistry B* 122.29 (2018), pp. 7436–7449.

[124] Matthew Z. Tien et al. “Maximum Allowed Solvent Accessibilites of Residues in Proteins”. In: *PLoS ONE* 8.11 (2013). Ed. by Alexey Porollo, e80635.

[125] Sebastian Salassi et al. “Au Nanoparticles in Lipid Bilayers: A Comparison between Atomistic and Coarse-Grained Models”. In: *The Journal of Physical Chemistry C* 121.20 (2017), pp. 10927–10935.

[126] Ole G. Mouritsen. *Life - As a Matter of Fat: The Emerging Science of Lipidomics (The Frontiers Collection)*. Springer, 2006.

[127] Christian Dietrich et al. “Relationship of Lipid Rafts to Transient Confinement Zones Detected by Single Particle Tracking”. In: *Biophysical Journal* 82.1 (2002), pp. 274–284.

[128] Michael J. Saxton and Ken Jacobson. “SINGLE-PARTICLE TRACKING:Applications to Membrane Dynamics”. In: *Annual Review of Biophysics and Biomolecular Structure* 26.1 (June 1997), pp. 373–399.

[129] S. Schuck et al. “Resistance of cell membranes to different detergents”. In: *Proceedings of the National Academy of Sciences* 100.10 (2003), pp. 5795–5800.

[130] Sabina Tatur et al. “Effect of Functionalized Gold Nanoparticles on Floating Lipid Bilayers”. In: *Langmuir* 29.22 (2013), pp. 6606–6614.

[131] Paraskevi Gkeka et al. “Membrane Partitioning of Anionic, Ligand-Coated Nanoparticles Is Accompanied by Ligand Snorkeling, Local Disordering, and Cholesterol Depletion”. In: *PLoS Computational Biology* 10.12 (2014). Ed. by Helmut Grubmüller, e1003917.

[132] Elena Heikkilä et al. “Atomistic simulations of anionic Au144(SR)60 nanoparticles interacting with asymmetric model lipid membranes”. In: *Biochimica et Biophysica Acta (BBA) - Biomembranes* 1838.11 (2014), pp. 2852–2860.

[133] Rachelle M. Choueiri et al. “Surface patterning of nanoparticles with polymer patches”. In: *Nature* 538.7623 (2016), pp. 79–83.

[134] Ana M. Percebom et al. “Janus gold nanoparticles obtained via spontaneous binary polymer shell segregation”. In: *Chemical Communications* 52.23 (2016), pp. 4278–4281.

[135] Xiang Liu et al. “Determination of monolayer-protected gold nanoparticle ligand–shell morphology using NMR”. In: *Nature Communications* 3.1 (2012).

[136] Ayush Verma et al. “Surface-structure-regulated cell-membrane penetration by monolayer-protected nanoparticles”. In: *Nature Materials* 7.7 (2008), pp. 588–595.

[137] Reid C. Van Lehn et al. “Lipid tail protrusions mediate the insertion of nanoparticles into model cell membranes”. In: *Nature Communications* 5.1 (2014).

[138] Rakesh Gupta and Beena Rai. “Effect of Size and Surface Charge of Gold Nanoparticles on their Skin Permeability: A Molecular Dynamics Study”. In: *Scientific Reports* 7.1 (2017).

[139] Shikha Nangia and Radhakrishna Sureshkumar. “Effects of Nanoparticle Charge and Shape Anisotropy on Translocation through Cell Membranes”. In: *Langmuir* 28.51 (2012), pp. 17666–17671.

[140] A. Relini et al. “Effect of physical constraints on the mechanisms of membrane fusion: bolaform lipid vesicles as model systems”. In: *Biophysical Journal* 71.4 (1996), pp. 1789–1795.

[141] Robert Hein, Can B. Uzundal, and Andreas Hennig. “Simple and rapid quantification of phospholipids for supramolecular membrane transport assays”. In: *Organic & Biomolecular Chemistry* 14.7 (2016), pp. 2182–2185.

[142] S Salassi et al. “A Martini coarse-grained model of the calcein fluorescent dye”. In: *Journal of Physics D: Applied Physics* 51.38 (2018), p. 384002.

[143] Abolfazl Akbarzadeh et al. “Liposome: classification, preparation, and applications”. In: *Nanoscale Research Letters* 8.1 (2013), p. 102.

[144] A.D. Bangham, J. De Gier, and G.D. Greville. “Osmotic properties and water permeability of phospholipid liquid crystals”. In: *Chemistry and Physics of Lipids* 1.3 (1967), pp. 225–246.

[145] Eudald Casals et al. “Time Evolution of the Nanoparticle Protein Corona”. In: *ACS Nano* 4.7 (2010), pp. 3623–3632.

[146] J S. Dua, A.C. Rana, and A.K. Bhandari. “Liposome: Methods of preparation and applications”. In: 3 (2012), pp. 14–20.

[147] Michael J. Hostetler et al. “Monolayers in Three Dimensions: Synthesis and Electrochemistry of -Functionalized Alkanethiolate-Stabilized Gold Cluster Compounds”. In: *Journal of the American Chemical Society* 118.17 (1996), pp. 4212–4213.

[148] Michael J. Hostetler, Allen C. Templeton, and Royce W. Murray. “Dynamics of Place-Exchange Reactions on Monolayer-Protected Gold Cluster Molecules”. In: *Langmuir* 15.11 (1999), pp. 3782–3789.

[149] Alicia M. Jackson, Jacob W. Myerson, and Francesco Stellacci. “Spontaneous assembly of subnanometre-ordered domains in the ligand shell of monolayer-protected nanoparticles”. In: *Nature Materials* 3.5 (2004), pp. 330–336.

[150] Prashant K. Jain et al. “Review of Some Interesting Surface Plasmon Resonance-enhanced Properties of Noble Metal Nanoparticles and Their Applications to Biosystems”. In: *Plasmonics* 2.3 (2007), pp. 107–118.

[151] A. Laouini et al. “Preparation, Characterization and Applications of Liposomes: State of the Art”. In: *Journal of Colloid Science and Biotechnology* 1.2 (2012), pp. 147–168.

[152] M.J Morilla et al. “Development and in vitro characterisation of a benznidazole liposomal formulation”. In: *International Journal of Pharmaceutics* 249.1-2 (2002), pp. 89–99.

[153] M. Reza Mozafari. “Liposomes: an overview of manufacturing techniques.” In: *Cellular and molecular biology letters* 10.4 (2005), pp. 711–719.

[154] James R Nicol, Dorian Dixon, and Jonathan A Coulter. “Gold nanoparticle surface functionalization: a necessary requirement in the development of novel nanotherapeutics”. In: *Nanomedicine* 10.8 (2015), pp. 1315–1326.

[155] Mohamed Abd-Elmoneim Raslan and. “Effect of Some Formulation Variables on the Entrapment Efficiency and in Vitro Release of Ketoprofen from Ketoprofen Niosomes”. In: *Journal of Life Medicine* 01.02 (2013), pp. 15–22.

[156] Stefania Sabella et al. “A general mechanism for intracellular toxicity of metal-containing nanoparticles”. In: *Nanoscale* 6.12 (2014), p. 7052.

[157] Qing Shao et al. “Difference in Hydration between Carboxybetaine and Sulfobetaine”. In: *The Journal of Physical Chemistry B* 114.49 (2010), pp. 16625–16631.

[158] Janos Szebeni et al. “Oxidation and denaturation of hemoglobin encapsulated in liposomes”. In: *Biochimica et Biophysica Acta (BBA) - General Subjects* 798.1 (1984), pp. 60–67.

[159] Angeles Villanueva et al. “The influence of surface functionalization on the enhanced internalization of magnetic nanoparticles in cancer cells”. In: *Nanotechnology* 20.11 (2009), p. 115103.

[160] Xiaohu Xia and Younan Xia. “Gold nanocages as multifunctional materials for nanomedicine”. In: *Frontiers of Physics* 9.3 (2013), pp. 378–384.